THESIS

SUSTAINABLE RECYCLING OF METAL MACHINING SWARF VIA SPARK PLASMA SINTERING

Submitted by

Alexandra E. Sutherland

School of Advanced Materials Discovery

In partial fulfillment of the requirements

For the Degree of Master of Science

Colorado State University

Fort Collins, Colorado

Fall 2021

Master's Committee:

Advisor: Kaka Ma

Justin Sambur
Steve Simske

ABSTRACT

SUSTAINABLE RECYCLING OF METAL MACHINING SWARF VIA SPARK PLASMA SINTERING

In general, extracting virgin metals from natural resources exerts a significant environmental and economic impact on our earth and society. Production of virgin stainless steels and titanium (Ti) alloys have particularly caused concerns because of the high demands of these two classes of metals across many industries, with low fractions of scraps (less than one-third for steels and one-fourth for Ti alloys) that are currently recirculated back into supply. In addition, the conventional recycling methods for metals require multiple steps and significant energy consumption. With the overarching goal of reducing energy consumption and streamlining recycling practices, the present research investigated the effectiveness of direct reuse of stainless steel swarf and Ti-6Al-4V alloy swarf as feedstock for spark plasma sintering (SPS) to make solid bulk samples. The parts made from machining swarf were characterized to tackle material challenges associated with the metal swarf such as irregular shapes and a higher amount of oxygen content. The hypothesis was that while solid bulk parts made from metal swarf would contain undesired pores that degrade mechanical performance, some mechanical properties (e.g., hardness) can be comparable or even outperform the industrial standard counterparts made from virgin materials, because of cold working and grain refinement that occurred to the swarf during machining and the capability of SPS to retain ultrafine microstructures.

304L stainless steel and Ti-6Al-4V (Ti64) alloy swarf were collected directly from machining processes, cleaned, and then consolidated to bulk samples by SPS with or without addition of gas atomized powder. Nanoindentation and Vickers indentation were utilized to evaluate the hardness at two length scales. Ball milling was performed on Ti64 to assess the energy consumption required to effectively convert swarf to varied morphologies. In addition, to provide insight into

the macroscale mechanical behavior of the materials made by SPS of recycled swarf, finite element modeling (FEM) was used to predict tensile stress-strain curves and the corresponding stress distributions in the samples.

The key findings from my research proved that reuse of austenitic stainless steel chips and Ti64 alloy swarf as feedstock for SPS is an effective and energy efficient approach to recycle metal scraps, compared to the production and use of virgin gas atomized powders, or conventional metal recycling routes. The mechanical performance of the samples made from metal swarf outperformed the relevant industrial standard materials in terms of hardness while the ductility remains a concern due to the presence of pores. Therefore, future work is proposed to continue to address the challenges associated with mechanical performance, including but not limited to, tuning the SPS processing parameters, quantifying an appropriate amount of addition of powder as a sintering aid, and refining the morphology of the swarf by ball milling. It is critical for the health of our planet to always consider the tradeoff between energy consumption and materials performance.

ACKNOWLEDGEMENTS

I would first like to acknowledge Colorado State University for providing the start-up funding for my advisor's lab, which financially support my research. I would also like to acknowledge the NSF-CBET grant #1605392, which ended on June 30, 2020, for supporting part of the materials, supplies, and facility user fees at the beginning of my research. I would also like to thank my advisor, Dr. Kaka Ma, for always being there when I asked for help, patiently working with me, and helping formulate a research plan specific to my motivations.

I am also very thankful for the other members of my committee, Dr. Justin Sambur and Dr. Steve Simske, and the energy put forth to review my work. Dr. Justin Sambur also showed me another part of the research community during my first year rotations, and I am very appreciative of that.

The Colorado State University Analytical Research Core staff and their constant willingness to help with sample analysis and preparation played a crucial role to the success of my work. The remote analysis done with the assistance of Rebecca Miller and Steven Marquez during the pandemic was invaluable.

I would also like to thank Vincent Metals for providing the materials required for this work. Without them, none of this would have been possible.

I am incredibly grateful for the other students and professors at The Factory, Dr. Chris Weinberger, Alexander Preston, and Liam Fisher. The guidance and knowledge gained from lectures and individual conversations were irreplaceable.

Lastly, I would like to thank my parents, brother, friends and especially Corey for their unfaltering support and encouragement throughout this process. Without them, I would not have succeeded.

DEDICATION

To my parents, brother, Corey, Harley, friends and family.

TABLE OF CONTENTS

LIST OF TABLES

LIST OF FIGURES

Chapter 1

Literature Review and Goals of My Research

1.1 Introduction

Structural metals have been integral parts of our society for centuries, with steel gaining importance in the 1200s B.C. [1] and the first steel-framed building being constructed in 1885. In 1940, the Kroll process to extract and refine titanium was patented [2]. Titanium has entered many industries as an alternative to steels due to its high strength to weight ratio and corrosion resistance since then. However, its production requires several resource-intensive steps, leading to high costs and substantially negative environmental impacts. Current recycling methods of both steel and titanium alloys also require a high amount of energy and virgin material. This chapter provides literature review on the current recycling methods for metal scraps and recent efforts to improve the recycling efficiency. Based on the findings from the literature review, the motivation and objectives of my research are outlined at the end of this chapter, with an overall long term goal of developing a more sustainable strategy for recycling metal swarf.

1.1.1 Current Recycling Methods

There are three varieties of scrap metals: home, prompt industrial, and post-consumer. Home scrap is generated within the steel-making plant and no additional processing is required to recycle it prior to melting [3]. Fortunately, technological advances have significantly reduced the amount of home scrap produced [4]. Prompt industrial scrap is usually new, clean material that is a byproduct of manufacturing operations such as machining or defective parts. Post-consumer, or obsolete, scrap is sourced from a myriad of places including discarded vehicles, appliances, bridges or railroad cars [3, 4]. Each type of scrap is subjected to many different conditions during its life cycle, adding to the challenge of using a singular recycling method for them all.

The basic steps of metal recycling involve collection, separation and melting. The separation step can be extensive and involve both physical and chemical processes. Examples include eddy current separation, sweat furnace, magnetic separation or incineration [4]. After sorting and initial processing of the scrap is complete, it is melted with virgin material in an electric arc furnace. It then can be cast as slab or billets which are then machined to custom parts, or atomized to powder to be used in powder metallurgy applications such as additive manufacturing. Recycling offers both economic and environmental incentives. Rao reported that the cost of producing metals from scrap was nearly half that of producing virgin metals from ore [4]. Energy credits are issued from governments and general cost cuts are associated with reducing steps in the primary production process like extraction, making recycling of metals economically favorable for companies. One environmental incentive for metal recycling is the reduction of toxic gases that are released into the atmosphere, namely sulfur dioxide and dioxin. These gases are byproducts resulting from the decomposition of organic matter during the smelting process [4], which are harmful to both the environment and humans. Another importance of recycling is the reduction of the carbon footprint that results from producing new raw materials, i.e., extraction and production of materials from their raw resources. The majority of the world's energy production comes from fossil fuel-based sources that have high associated carbon emissions, so reducing the energy consumption is always equivalent to a reduction in the carbon footprint.

Johnson et al. analyzed the energy and material consumption for three scenarios: (1) current steel production, (2) 100% recycling of steel and (3) 100% virgin steel. They found that by increasing the amount of scrap that was mixed into an electric arc furnace with virgin material by just 25%, the total primary energy of the steel would decrease by 12% [5]. They anticipated that with the high demand of steel and the long lifetime of steel products, the amount of scrap currently in circulation would not meet the demand for global production [5]. However, as economic models become more circular to account for long-term environmental sustainability, the recycling rates and scrap collection will inevitably increase in the near future. The EPA estimated that each ton of recycled steel saves 642 kWh of energy [6]. Paraskevas et al. observed the energy consumption

needed to recycle aluminum using the current method of melting and casting scrap. They found that there is a significant material loss of 16-25% during the melting step due to oxidation, and that the overall quality also degraded due to loss of purity [7]. While the study was specific to aluminum, it demonstrates just one of the problems concerning current metal recycling practices.

Titanium (Ti) is a valuable metal commonly used in modern structural applications such as the aerospace industry. Due to its high strength to weight ratio, electrical and thermal conductivity, and high melting point, it outperforms several other metals like steels and aluminum alloys. Virgin titanium is typically produced through the Kroll process, in which titanium tetrachloride ($TiCl_4$) is reduced by liquid magnesium at a temperature of 800-850°C to provide Ti that is in a porous sponge form. Subsequently, the Ti sponge needs to be purified by leaching or vacuum distillation, crushed, and pressed before being melted to form ingot. It is often necessary to remelt the ingot to remove inclusions and/or to improve uniformity. These multiple steps represent the high energy consumption, adding to the cost of Ti, which is approximately six times more expensive than stainless steels. In addition, the use of Ti alloy ingots currently has a low material efficiency. For example, 90-120 tons of titanium alloy ingot is used for a single Boeing 787 aircraft, but approximately 85% (100 tons) of this becomes scrap during the machining process. Only roughly 12 tons actually goes to the aircraft [8].

Of the 100 tons of scrap generated from the aircraft, only 22% of it is circulated back into supply [9]. Currently, the Ti scrap is collected and cleaned to remove tool fragments, oil and impurities. It is then remelted with virgin material. With increasing cycles of use, the amount of impurities such as oxygen and iron will increase. The iron concentration can be mitigated during recycling by proper scrap separation prior to melting, but the oxygen levels will inevitably rise due to the dissolution of the surface oxide layer during melting. Because of this, pure scrap cannot be expected to be of the same quality grade if it is directly reused. To maintain a high purity and quality, scrap is remelted with virgin titanium sponge in order to dilute the oxygen concentration [8]. This imposes the problem of titanium's life cycle following a cascading model and not a cyclical model since subsequent life cycles result in continuous quality downgrades.

The high oxidation rates and purity restrictions make it a challenge to recycle Ti and its alloys. Titanium's high affinity to oxygen helps to hinder rust much more effectively than stainless steels due to the formation of a surface oxide layer, but the higher-purity grades of titanium require very low levels of oxygen - <0.2 wt-% for pure (grade 2) titanium and 0.25 wt-% for Ti6Al4V alloy (grade 5) [9] within the bulk. Ti64 will be used to denote Ti6Al4V alloy hereafter. Table 1.1 summarizes the specific energy consumption and carbon dioxide emissions associated with the primary production and recycling for 304L stainless steel, grade 2 Ti and grade 5 Ti, as well as the recycling fraction in current supply [9]. Apparently, both the energy consumption and carbon emissions associated with producing and recycling Ti are nearly ten times greater than that of a commonly used stainless steel (304L). It is also worth noting that although the amounts of recycled material in current supply are comparable, there is still substantially less titanium being recycled compared to stainless steel. Much of this stems from the difficulty in direct recycling of titanium, particularly the higher purity grades.

Table 1.1

Primary Production	**304L**	**Grade 2 Ti**	**Grade 5 Ti**
Energy (kWh/kg)	18.6	163.0	190.7
CO_2 (kg/kg)	4.4	33.3	40.3
Recycling	**304L**	**Grade 2 Ti**	**Grade 5 Ti**
Energy (kWh/kg)	4.2	21.5	24.2
CO_2 (kg/kg)	1.2	6.1	6.8
Fraction in current supply (%)	32.4	23.0	22.0

1.2 New Recycling Methods

The current recycling processes are effective and already incorporated into our infrastructure, but there is plenty of room for improvement if we are to transition to a more sustainable and circular economic model. To achieve greener material engineering, the energy, chemical and water consumption must be minimized during the recycling process while maximizing material quality and output. Due to the high price and demand for titanium, research is being conducted on a variety of recycling methods, the most common of which involves high energy ball milling. One of the benefits of ball milling is the ability to manipulate mechanical properties by grain refinement. As described in the next section, material strength tends to increase with decreased grain size. Since ball milling can refine grains down to the nanometer scale, it introduces the ability to strengthen the materials without altering chemical compositions.

1.2.1 Ball Milling

Mechanical milling utilizes plastic deformation to break down particles and reduce grain size (Figure 1.1). During ball milling, the impact of milling media on particles in the form of compressive and shear stresses introduces dislocations into the lattice. As milling continues, the dislocation density increases, thereby increasing the average atomic-level strain. Eventually, the dislocations pile up and form sub grains separated by low-angle grain boundaries that lower the total internal strain [10]. With continued milling, grain rotation transforms the low angle grain boundaries to high angle boundaries through several pile-up and annihilation events, ultimately leading to grain refinement. Nanocrystalline materials display increased hardness and strength according to the Hall-Petch relation given by Equation (1.1)

$$\sigma_y = \sigma_0 + k_y d^{-1/2} \tag{1.1}$$

where σ_y is the yield strength, σ_0 is the materials starting stress required for dislocation movement, k_y is the materials strengthening coefficient and d is the average grain diameter [11]. Because of the high number of grain boundaries present in nanocrystalline materials, diffusion rates also

tend to increase resulting in a decrease in sintering times [10]. The repeated plastic deformation straining a crystal lattice can also lead to the diffusionless martensitic phase transformation. For example, the FCC lattice in austenitic stainless steel can become strained and transform to a body-centered tetragonal (BCT) lattice (a martensitic phase) under constant plastic deformation. Martensitic stainless steels are typically much harder and stronger, but they lack the ductility and formability of an austenitic (FCC) steel.

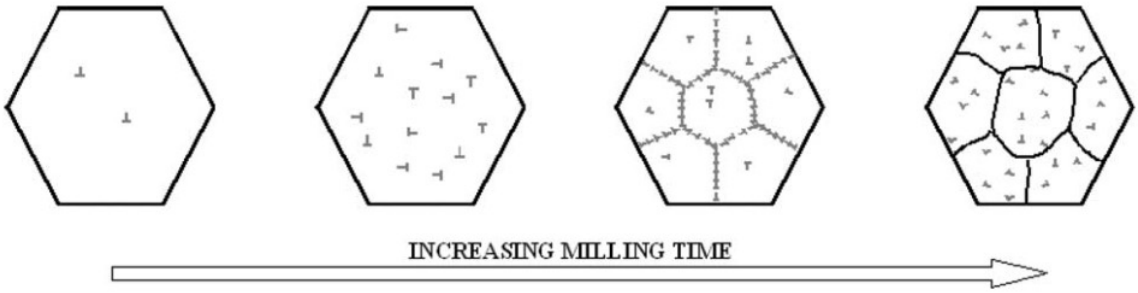

Figure 1.1: Schematic representation of grain refinement during ball milling [12].

Several research groups have investigated ball milling of stainless steel or Ti machining scrap as a recycling method. For example, de Sales Pereira Mendonça et al. ball milled 3 wt-% vanadium carbide with duplex stainless steel (UNS S31803) machining chips for 50 hours in argon, followed by a 30-minute residual stress relief treatment at 1050°C. The powder that resulted from the milling was then compressed and sintered at 1200°C for one hour. They found that the addition of the vanadium carbide significantly helped with particle size reduction. However, it led to a higher porosity in the sintered sample which lowered the micro-hardness [13]. Martensitic formation occurred due to the ball milling and was present after sintering to a bulk sample. The group's studies lacked discussion on the effect of ball milling on the microstructure of the sintered samples and it is unclear whether the hardness increased due to grain refinement or the addition of the carbides. Enayati et al. also ball milled stainless steel machining chips that were 2-4 mm long for 25, 50 and 100 hours. A martensitic phase transformation was also reported after 25 hours of milling, but the relative amount of martensite did not increase as milling time increased [14].

The grains were on the nanometer-scale after ball milling, resulting in an increased hardness of the milled powder. However, the powder was then annealed which resulted in grain growth and reduction in the amount of martensite, therefore decreasing the hardness [14].

Shial et al. ball milled commercially pure grade 2 titanium chips that had been cut into 8-10 mm long and 1 mm wide pieces. They were wet milled in toluene for a total of 2.5 hours using stainless steel media. The resultant powder was then mixed with a 4 μm graphite powder in varying ratios that acted as a lubricant to help prevent cold welding and oxidation of the titanium particles, and was ball milled for another 12 hours. Grain refinement of the powder particles occurred but trace amounts of iron contamination from the milling media were present after 2.5 hours of milling [15]. It was also concluded that a complete conversion from chips to powder would be very difficult to obtain. However, over 95% of the chips had been converted to powder demonstrating the capability of ball milling for particle size reduction [15]. Both Enayati et al. and Shial et al. were successful in showing that ball milling is an effective method for the conversion of scraps to powders, but neither group consolidated their powders to bulk materials to evaluate the quality and properties of the parts made from the recycled metal chips.

In addition, several studies explored ball milling of commercial gas or water atomized powders in order to change the morphology, microstructure, or composition to create a specific composite or alloy. For example, Corrochano et al. ball milled gas atomized Al 6061 powder with $MoSi_2$ powder for 1-2 hours with the intention of making a composite. They found that the decreased powder particle size from ball milling allowed for better packing, and that strain hardening occurred to the powder during ball milling [16]. The ball milled powder was hot extruded to form bulk samples, which exhibited improvement in the mechanical properties due to the homogeneous distribution of the $MoSi_2$ reinforcement particles throughout the matrix [16]. In 2017, Kulecki and Lichanska ball milled four different alloy compositions of Fe-Cr-Mo-Mn-(Cu) steel powders for either 0.5, 1 or 2 hours. The milled powders were then pressed into dogbone structures and furnace sintered at 1250°C for 1 hour. They also observed that the improvement in packing efficiency was directly proportional to the ball milling time due to the reduction in powder particle size as the milling time

increased [17]. It was also found that having more total alloy additions enhanced the hardenability and that the ball milling significantly improved the plastic properties of the sintered sample [17]. In 2020, Long et al. ball milled gas atomized Ti64 with a particle size less than 70 μm for 10 hours in argon. XRD results showed that there was clearly grain refinement and lattice distortion after ball milling. The milled powder was spark plasma sintered with a pressure of either 100 or 300 MPa (31 or 94 kN, respectively) to temperatures between 550-700°C with a heating rate of 100°C/min. After sintering, the hexagonal close packed (HCP) α-phase transformed to a duplex HCP α + body centered cubic (BCC) β phase with a much more homogeneous microstructure [18]. No local recrystallization or grain growth occurred below 650°C, but there was a lower density of intragranular dislocations at both 650°C and 700°C, and the grain boundaries became more straight and polygonal, indicating recovery and recrystallization [18]. Sun et al. proposed a method to transform Ti64 scrap into usable feedstock powder for additive manufacturing. The starting material for their method was hydrogenated Ti64 powder that had been produced from Ti64 scrap, hydrogenated and ball milled. They then ball milled this powder in an unspecified solvent mixed with a thermoplastic binder and obtained a particle size less than 10 μm. After milling, the particles were spray dried with argon to obtain spherical particles. A debinding process was used to remove the thermoplastic binder and the powder was then sintered at 1200°C for 4 hours in argon, followed by de-oxygenation at 750°C for 12 hours before being leached with diluted hydrochloric acid and finally air dried. The particles had less than 5 vol-% porosity, very low oxygen levels and high sphericity, making for a very usable powder for additive manufacturing [19]. However, the process itself is relatively complex and involves numerous steps and chemical additions, making it overall just as costly and unsustainable as the current recycling methods for Ti used in industry.

1.2.2 Sintering

Sintering is divided into either liquid state or solid state categories depending on which phases are present during the process. Belt furnace sintering and hot isostatic pressing (HIP) are examples of liquid state and solid phase methods, respectively, and are widely used in industry. Solid state

sintering usually happens around 2/3 of the melting temperature of a material [20] and occurs in three stages: (1) initial stage, (2) intermediate stage and (3) final stage. These stages are illustrated in Figure 1.2. Prior to the initial stage, particles are considered loose. Particles are cold packed using a uniaxial press to maximize the surface contact between particles. During the initial sintering stage, the contacts between particles, known as necks, are first being formed. The intermediate stage involves growth of the necks, but the pores are still continuous [21] until the final stage is reached, where the pores become discrete and are eventually closed [21]. Several variables can affect the sinterability and microstructure of a material including powder shape, morphology, material composition, temperature, pressure, time, heating rate and cooling rate [22].

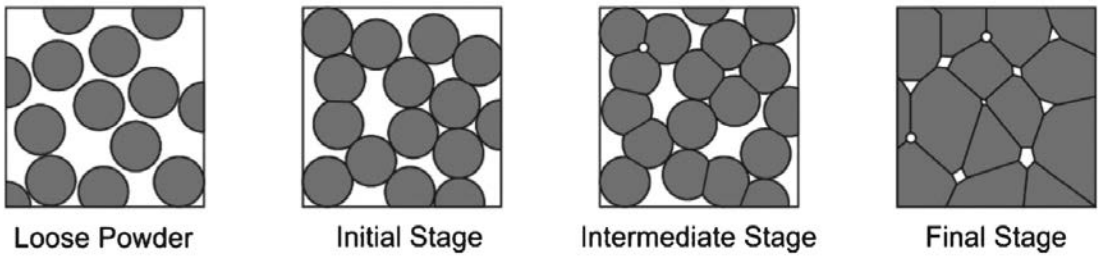

Figure 1.2: The stages of sintering, starting with loose powder prior to the initial stage and finishing with the closure of pores formed by necks [23].

Without any driving forces, sintering would not occur. Particle surfaces have an associated free surface energy, γ_s, which is the amount of energy required to create a new unit of surface area [20]. In order to minimize the total energy of the system, diffusion of atoms will occur when possible, leading to the formation of necks between particles. The temperature and pressure applied during sintering facilitates this mass transport. In liquid state sintering, the atomic mobility is high and particles have a relatively high energy. In solid state sintering of crystalline materials, however, the formation of necks also leads to the formation of a solid-solid interface that has an associated free energy, γ_{ss}. Therefore, there is an energetic tradeoff between the reduction of particle surface area and the increase of interface area. The ratio between these energies is dependent on the angle created between two particles, φ_e, which is also referred to as the dihedral angle, as given

in Equation (1.2) [20]. Locally, the driving force is dictated by the curvature of surfaces where mass diffusion occurs from regions of sharp curvature to those of low curvature [24], [20]. In the initial sintering stage, the radius of necks are acute and typically less than 0.2 times the particle radius [21].

$$\frac{\gamma_{ss}}{\gamma_s} = 2cos(\frac{\phi_e}{2}) \tag{1.2}$$

In the final stages of sintering, γ_s is much smaller but γ_{ss} is much larger than previous stages. According to Equation (1.3), as the volume, *V*, and densification of particles changes, the pressure (and therefore energy) required to continue changing the volume also changes

$$\Delta P = \gamma \frac{dA}{dV} \tag{1.3}$$

where *A* is the particle surface area. Assuming spherical particles, the required pressure will decrease as the particle radius increases [20]. Therefore, as the necks grow in size, the energy required to continue growing them decreases. The vapor pressure, *p*, and solubility (related to a difference in chemical potentials, $\Delta\mu$) also have a large effect on this process as given by Equation (1.4) [20] where *R* is the gas constant, *T* is temperature, and *p* and p_0 are vapor pressures associated with curved and flat surfaces, respectively. Therefore, the chemical potential gradient that acts as a driving force for mass diffusion will decrease as the particle surface becomes less curved. This also determines that smaller particles with a higher curvature will have a higher driving force than larger particles.

$$\Delta\mu = RTln(\frac{p}{p_0}) \tag{1.4}$$

Spark plasma sintering (SPS), also known as field assisted sintering technology (FAST), is a solid-state sintering method that leverages the Joule heating effect to sinter fully dense materials in a matter of minutes. The general setup of SPS is illustrated in Figure 1.3 [25] and consists of an electrically conductive unit comprised of electrodes, graphite spacers, punches and a die containing

the sample, all within a vacuum chamber. Graphite is commonly used for the tooling due to its easy machinability, high compressive strength, and high thermal and electrical conductivity. A uniaxial pressure is applied from the top which aids in the sintering process as described above. A current is passed through the conductive tooling and the electrical resistance generates heat via the Joule heating effect, where the power of heat produced is proportional to the material's resistance and the square of the current passing through the material. Even if the material being sintered is conductive, most of the heat transfer comes from the graphite tooling due to the limited surface contact between particles within the green body. High heating rates of 100°C/min up to 1000°C/min can be achieved with SPS [26], making it much faster to achieve fully dense parts and with a power consumption three to five times lower than traditional methods such as pressureless furnace sintering, hot pressing and hot isostatic pressing [27].

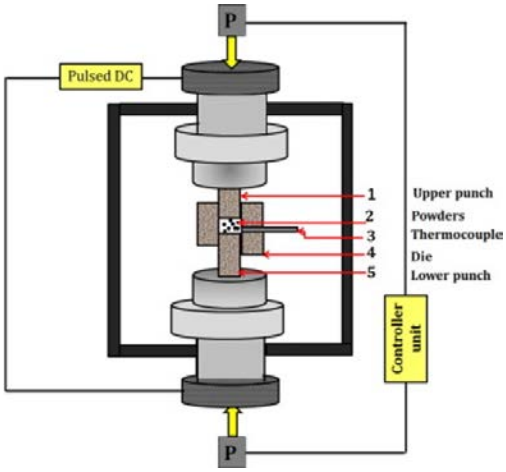

Figure 1.3: Diagram of SPS setup [25]

Another attractive benefit of SPS is the restricted grain growth that occurs during sintering due to the short sintering time and relatively lower temperature required compared to other sintering methods. This can be advantageous in the case of nanocrystalline materials and for the manipulation of mechanical properties. In general, the driving forces for grain growth are the same as sintering - curvature and interfacial energy - but the interface considered in the case of grain growth is the grain boundary, γ_{GB}, [20]. The stability of a grain is dictated by its curvature (as previously

discussed) and the amount of other grains surrounding it. In order to reach an equilibrium, the angle created by adjoining grains must be so that curvature is minimized. For example, one grain surrounded by six other grains can form 120° angles at each triple point. Once another grain is added or subtracted, a geometric distortion is forced and a concave interface is formed on the central grain, creating a driving force for the grain boundary to move [20]. Mathematically, this can be written with Equation (1.5) [20]

$$\frac{dr}{dt} = k\frac{D_{GB}}{RT}\frac{2\gamma_{GB}}{r_0}\frac{V_M}{w} \tag{1.5}$$

where D_{GB} is the grain boundary diffusivity, k is a constant, w is the boundary thickness and r_0 is the initial grain radius. The concept of grain stability can be related to pore stability during sintering. In the final stages of sintering when pores become discrete and not continuous, they do so on grain boundaries. Depending on the angle formed between the pore and the surrounding grains, a pore will either grow or shrink. However, there is also an associated interfacial energy with pores due to the solid-vapor interface which acts as a driving force to close the pores. The diffusion mechanism is of high importance during sintering and when considering neck growth. If neck growth happens primarily by surface diffusion where atoms are migrating from the particle surface to the neck, the neck will only elongate and the distance between two particles will not decrease. If neck growth occurs by bulk or grain boundary diffusion, the neck will increase in thickness and ultimately lead to a higher densification [28]. The shrinkage, ΔL, is given mathematically by Equation (1.6), where D_l is the lattice diffusion constant, V is the particle volume, and a is the particle radius [20].

$$\frac{\Delta L}{L} = \sqrt{\frac{D_l \gamma_s V t}{RT a^3}} \tag{1.6}$$

Research on directly recycling scrap materials is gaining increasing attention in the scientific community. Depending on the material, this can present several challenges such as morphology, composition and microstructure - most of which are altered during prior life cycles. In 2016, Lui

et al. studied the effect of chip conditions on the solid-state recycling of Ti64 machine chips using equal channel angular pressing (ECAP) [29]. Five different chips were used where the lengths varied from 0.1 to 3 cm, thicknesses from 50-500 μm and widths from 0.1 to 1 cm. They found that all the samples achieved full density after ECAP and annealing (at 1050°C for 0.5 hour in order to homogenize the β-phase) and that the compositions after consolidation were similar between samples - i.e. no increase in oxygen content. The prior chip boundaries were still visible between samples but bonding was successfully achieved. They also report that the microstructure reflected the dimensions of the starting chips, where smaller grains resulted from smaller chips, and that the chip boundary spacing was dependent on the starting chip thickness. The recycled chips had a higher hardness due to the high dislocation density and ultrafine grains, as well as dispersed oxides that had been broken up from prior chip boundaries [29]. Luo et al. also successfully used ECAP as a solid-state recycling method of commercially pure (CP) grade 2 titanium scrap [30]. They observed that the grain refinement that occurred during ECAP strengthened the material, but the grain growth that began to occur with further processing and at temperatures above 590°C ultimately reduced the strength of their consolidated material [30]. Paraskevas et al. used a 50/50 mixture of thin, flat aluminum 6061 machine chips and gas atomized powder. The mixture was cold pressed and SPS'ed up to 490°C at 100°C/min using a uniaxial pressure of 200 MPa. Good bonding between the chips and powder was obtained and the sample was nearly fully dense, containing only one small region with pores. The hardness was slightly higher than commercial aluminum 6061 but only by a marginal amount. The group believed that the powder aided in bonding the chips together and excluding residual porosity, as well as obtaining more homogeneous mechanical properties throughout the sample [27].

Weston and Jackson sintered thin, rectangular grade 5 Ti64 chips approximately 5 mm long using field-assisted sintering technique (FAST) [31]. The samples were sintered at either 950°C or 1200°C with a hold time of 0, 5 or 30 minutes at the peak temperature. They found that the 950-0 (temp-dwell time) sample had a 97.7% relative density and by increasing the hold time to 5 minutes at the same temperature, the density increased by 1.4%. Increasing the temperature

to 1200°C resulted in a negligible density increase compared to the 950°C samples, but allowed for increased homogenization of the β-phase as it was past the 990°C β-transus temperature [31]. Dwell times longer than 5 minutes did not increase the density any more than 0.2%. The observed pores were triangular in shape and believed to be a result of the serrations in the machining chips. It was also reported that at higher temperatures and with a longer hold time, it was no longer possible to perceive that the material was derived from a swarf feedstock. This study demonstrated that using swarf directly as the feedstock for sintering is a potential recycling method. However, the composition and any increase in oxygen levels were not reported, which are critical for the quality of the resulting materials. Kuçera et al. created chips by filing Al-Fe17 ingot to a size of 1.25-20.88 μm (most between 2-8 μm) and ball milled the filings at a 30:1 BPR for 8 hours in argon [32]. 10 g of the chips were then placed in a 20 mm diameter graphite die and pre-compacted with 360 MPa, then loaded with 3 kN in an SPS which was then heated at 100°C/min to 500°C and held for 10 minutes at a 48 MPa (15 kN) followed by spontaneous cooling in the chamber. They showed that the chips that had been ball milled, pre-compacted and then sintered had a lower porosity than the sample that had not been pre-compacted. In addition, the samples that were ball milled were twice as strong as those that were not milled at all. This indicates that the grain refinement that occurred during ball milling was successfully retained during SPS. However, a secondary phase ($Al_{13}Fe_4$) precipitated during sintering which facilitated in a decreased ductility [32].

In the case of sintering swarf, the morphology of the swarf, which is typically non-spherical with large, low-curvature surfaces, plays an important role in the densification behavior. When the swarf particles are packed together, they will naturally orient uniformly so that the largest face is perpendicular to the uniaxial applied pressure in an effort to reduce the force per unit area. The majority of the contact area will therefore be along the lengths of chips. The dihedral angle between these surfaces is relatively low, leading to a higher ratio of interfacial energy to surface energy given in Equation (1.2). Despite the low dihedral angle, it is anticipated that the interfacial energy from the contacting area between neighbor chips is the primary driving force for diffusion. In the case of thick chips, the two ends of the chips have a lower surface area than the long, flat

surface, but a higher curvature. Therefore, the curvature is the primary driving force for pore closure.

One issue that may occur during sintering is local overheating at chip boundaries. Most of the heat transfer during SPS comes from the graphite tooling, but there is still a small amount of current passing through conductive samples in later sintering stages and the contact area between particles can effect local temperature gradients. Microstructural evidence of melting and high temperature gradients were found at interparticle junctions of spark plasma sintered titanium alloys [33, 34]. It was also predicted that larger particles in the centimeter size range would have much higher local overheating compared to smaller particles on the micron scale [34]. If this were to occur, liquid state sintering may be achieved, consuming more energy than necessary and affecting the final microstructure. However, a model to accurately predict the amount of overheating has not yet been developed.

1.3 Motivation and Aims

1.3.1 Materials of Interest

Extracting virgin metals from natural resources generally exerts a significant environmental and economic impact on our earth and society. Production of virgin stainless steels and titanium (Ti) alloys have particularly caused concerns because of the high demands of these two classes of metals across many industries. Currently, less than one-third of steel scrap and less than one-fourth of titanium scrap are recirculated back into supply [9]. In addition, the traditional recycling methods require multiple steps and significant energy consumption, especially for Ti and its alloys.

304L is a low-carbon austenitic, i.e. face centered cubic (FCC) crystal structure, stainless steel that has a combination of desirable properties such as machinability, high strength and ductility, and high corrosion resistance. Strain-induced martensite is a unique feature of austenitic stainless steels and occurs as a result of plastic deformation or rapid cooling. The martensitic phase transformation significantly affects the strength and ductility, and the microstructure resembles twin or lath structures.

Titanium is a valuable material due to its high strength to weight ratio, but requires the extensive Kroll's process to extract it. There are two allotropic forms of titanium: the HCP α-phase is the equilibrium phase at temperatures below 882°C (for pure Ti), and the BCC β-phase is the equilibrium phase for high temperatures (882°C < T < 1668°C). The α-phase can be stabilized by alloying with elements such as oxygen, nitrogen and carbon, which also act to strengthen by solid-solution strengthening and invoking better creep resistance than the β alloys [35]. However, many of these stabilizing elements are considered problematic for industry applications since they are easily picked up by titanium, and diminish the toughness [2]. β alloying elements include chromium, molybdenum and niobium. These act to reduce the β-transus temperature (882°C for pure Ti, 990°C for Ti64 [31]) and also tend to decrease the strength while increasing the formability [35] due to the higher number of slip systems in the BCC structure compared to HCP. The Ti64 alloy selected in my research is an α-β Ti alloy that is applied in a wide range of applications, including the aerospace industry and biomechanical applications, where low weight and excellent corrosion resistance are crucial.

As discussed in Section 1.2, Ti64 chips have been studied as a feedstock for SPS in the literature. However, the critical concern on the pickup of impurities such as oxygen, has not been fully understood. The quality of the parts made from Ti64 swarf without ball milling were not investigated in previous studies. Therefore, 304L stainless steel and Ti64 were selected as the two primary materials of interest in my research.

1.3.2 Specific Aims

The overarching goal of the present research is to reduce energy consumption and streamline recycling practices for commonly used metals, taking into account the tradeoff between materials performance and environmental impact. Despite the progress that has been reported in literature, previous studies were limited to recycling chips via ball milling to convert them to powders without evaluating the properties and integrity of bulk solid materials made from the ball milled powders. In addition, very few efforts were put into the environmental impact assessment of the recycling

methods. Particularly, it remained unclear how effective it could be to directly reuse metal swarf as feedstock for sintering to make bulk materials for practical applications. How would the irregular shape and variance in size of metal swarf affect the densification behavior compared to the spherical gas atomized powder that is expensive and energy-intensive to produce? A novel recycling method can be developed for commonly used metals by combining ball milling and SPS. Because of the capability of SPS to restrict grain growth, the ball milling of chips followed by SPS can allow sustainable recycling of metals while maintaining or improving mechanical properties. Spark plasma sintering a mixture of virgin powder with scrap chips of the same material has also not been explored by many groups, particularly with 304L stainless steel or titanium alloys. Another key component that has not been addressed by previous research is the environmental impacts of recycling, specifically the energy consumption. It is important to analyze and compare new methods to current industry methods to select more sustainable recycling approaches.

To address the aforementioned questions and to fill the gap in current knowledge on recycling of metal swarf via SPS, the present research had the following specific aims: (1) to assess the effectivity of using swarf directly as the feedstock for SPS by evaluating and comparing the quality of the sintered bulk parts to industrial standard materials or counterpart samples made from virgin materials or powders, and (2) to assess the associated energy consumption of the proposed new recycling approach in comparison to conventional recycling routes and/or the production of parts using virgin gas atomized powder. The present work explored three recycling methods: (1) spark plasma sintering of swarf, (2) spark plasma sintering of a mixture of swarf and gas atomized powder to use the powder as a sintering aid, and (3) ball milling of swarf to evaluate the minimal processing parameters required to achieve various morphologies. The first two methods are performed to distinguish from the prior studies where chips are completely converted to powder. For methods (1) and (2), ball milling was performed for a very limited time length (15 minutes) in order to detangle some long and curly chips. In other words, the feedstock of the SPS is still in the form of chips rather than powder.

Chapter 2

Approach: Experimental Procedure and Characterization Methods

This chapter is to describe the experimental procedures and characterization methods used in both direct recycling of chips and formation of powder from chips. The experimental process is outlined in Figure 2.1. Limited ball milling was performed on the titanium chips prior to SPS. Bulk samples made from recycled scraps via SPS were characterized for phase constitution, morphology, microstructure and hardness. The 304L samples consist of (1) a 50/50 blend of nibbled 304L chips and gas atomized 304L powder (SS-50) and (2) 100% nibbled 304L chips (SS-100). The Ti64 samples consist of 100% Ti64 chips that had been minimally ball milled before SPS under varying conditions. Ti64 chips were also ball milled with toluene and varying amounts of stearic acid in an attempt to form a powder suitable for additive manufacturing. Samples from ball milling were collected every 10 hours to analyze the evolution of phase constitution, particle size distribution and particle morphology as a function of ball milling time length.

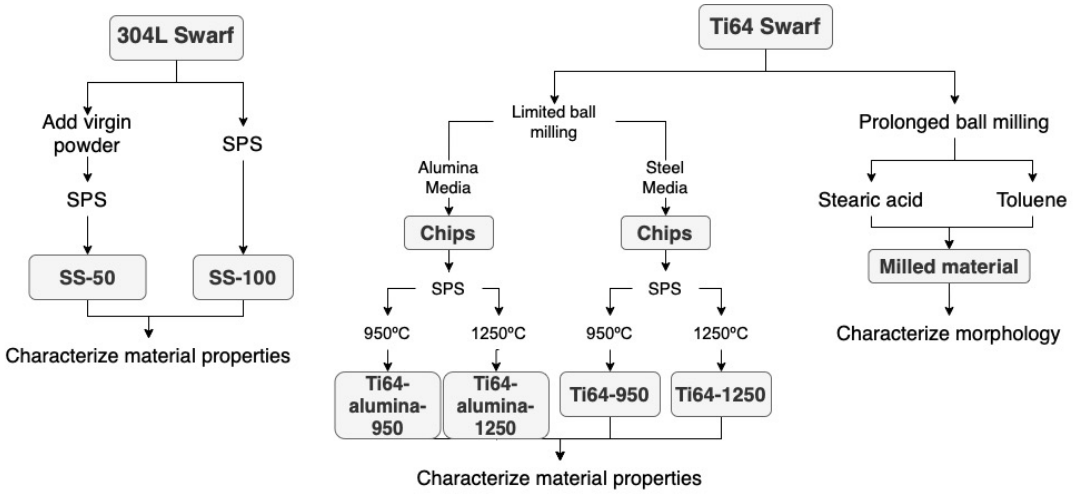

Figure 2.1: Flowchart outlining experimental processes.

2.1 Materials Selection

The two materials studied in this work are 304L stainless steel and Ti-6Al-4V (Ti64). The use of the 304L serves the purpose of acting as a starting point in the development of a new and more sustainable recycling method for titanium alloys. The stainless steel chips were received by AK steel (West Chester Township, Butler County, Ohio, OH). They were previously machined from a larger piece of virgin feedstock material (nibbled) and are considered coarse in size. Optical and SEM images are shown in Figure 2.2. The composition of the 304L chips is given in Table 2.1 [36].

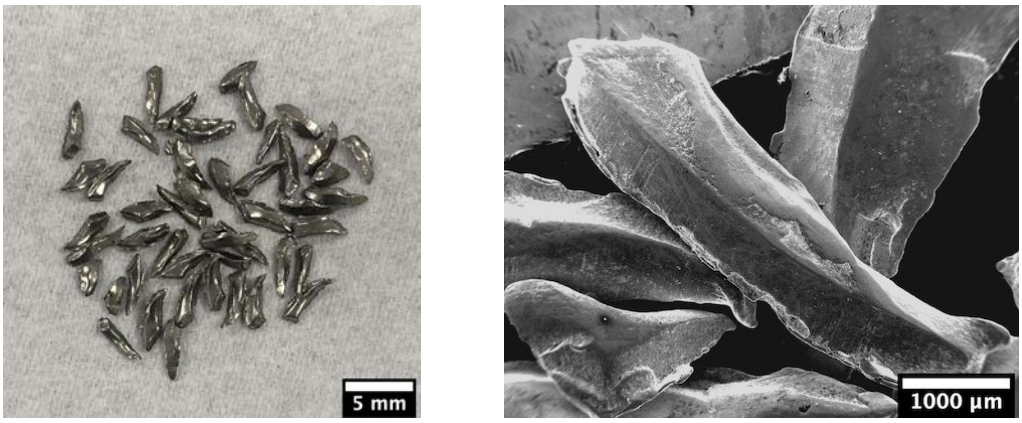

(a) **(b)**

Figure 2.2: (a) Optical and (b) SEM images of the AR 304L chips.

Table 2.1: Nominal composition of 304L chips, as received [36].

Elements	**Fe**	**Cr**	**Ni**	**C**	**Mn**	**Cu**	**Si**	**Mo**	**V**
wt.%	Balance	18.18	8.09	0.0253	1.30	0.57	0.41	0.26	0.064
Elements	**W**	**N**	**P**	**Nb**	**Al**	**B**	**S**	**Ti**	**Ca**
wt.%	0.059	0.038	0.027	0.013	<0.003	0.0026	0.0021	0.002	<0.0005

Ti64 machining chips were provided by Vincent Metals (Portland, OR), made from fine machining of medical-grade devices such as titanium implants. The chips are significantly finer in size, with more severe serrations than the 304L chips and a curled structure, as shown in Figure 2.3.

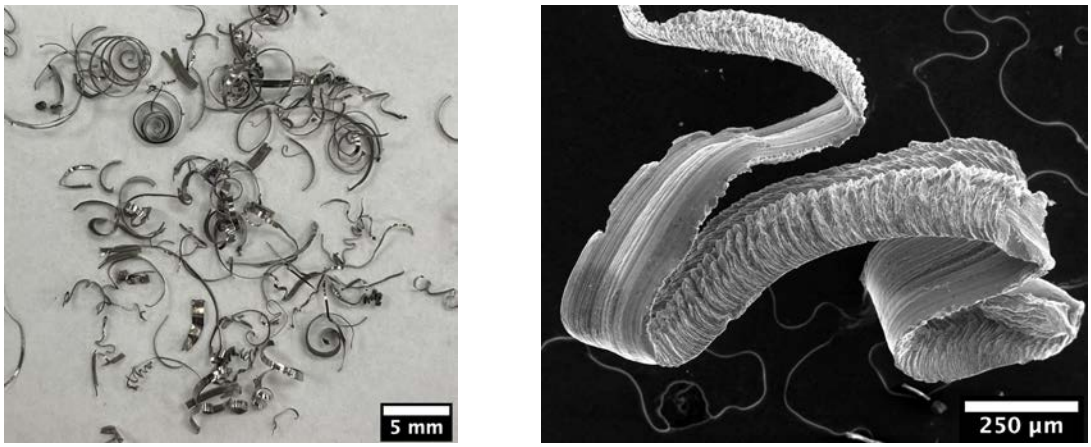

(a) **(b)**

Figure 2.3: (a) Optical and (b) SEM images of AR Ti64 chips.

The Ti64 chips were collected directly from machinery. Once received, they were cleaned thoroughly by ultrasonicating in acetone for 30 minutes. Every five minutes, the chips were stirred to separate any large clumps that had formed and to ensure all chips were thoroughly cleaned. 15 minutes into the cleaning process, the acetone was changed out. This helped in a rough estimate of any remaining machine oil left on the chips, as the first beaker of acetone was typically a yellow-brown color but the final beaker remained clear in color throughout the final 15 minutes of sonicating. The chemical composition of industry standard annealed Ti64 is given in Table 2.2.

Table 2.2: Nominal composition of Ti64 [9].

Elements	**Ti**	**Al**	**V**	**O**	**C**	**N**	**H**	**Fe**	**Other**
wt.%	Balance	5.5 - 6.75	3.5 - 4.5	<0.2	<0.1	<0.05	<0.0125	<0.4	0.4

Figure 2.4 shows SEM images of the Ti64 chips prior to any processing. The chips depicted were mounted in a resin epoxy, polished to 0.05 µm and etched using Kroll's reagent to reveal the microstructure. The AR chips exhibited elongated, lamellar grains, which is the typical microstructure of Ti64. Figure 2.4a shows the chips mounted in the epoxy and captures the variance in chip sizes and morphologies. There is a large variance in the width of the chips, between 7.96-390.14 µm, with the majority of them being between 42.36-67.23 µm. The average chip width was measured to be 54.55 µm. The average grain width was measured to be 2.96 µm, with widths ranging from 0.623-10.86 µm. Individual colonies were not distinguishable within the chips. Distortion of the chips was observed due to the machining process used to create the chips, as shown in Figure 2.4b, where the directions of the grains rotate as the chip curves.

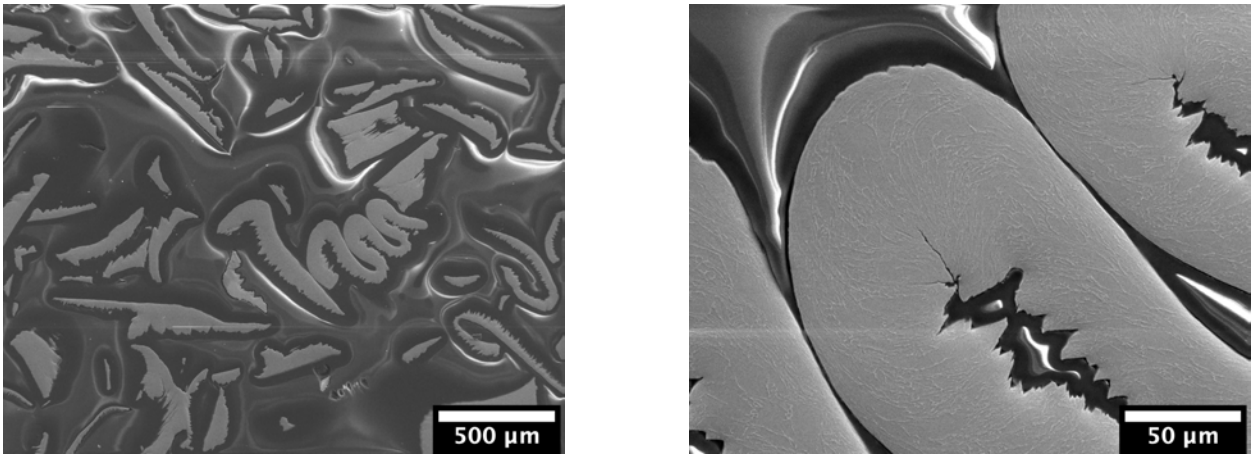

(a) **(b)**

Figure 2.4: SEM images of the etched AR Ti64 chips. Microstructure is distinguishable in (b).

2.2 Materials Consolidation

Many methods exist for the consolidation of metal scrap and powders including, but not limited to, casting, forging and sintering. Each method results in different defects such as pores, cracks and dislocations, that effect the mechanical properties [37]. These methods also vary in cost effectiveness and the flexibility in creating complex shapes. Casting of metals is one of the most

conventional and relatively simple methods. Melted metal is poured into a prepared mold. After cooling and solidifying, fine machining is performed to obtain the final part. Because of its simplicity and ability to create complex shapes, casting is considered a highly cost-effective method [37]. However, the subsequent subtractive machining processes lead to high material waste. In addition, the microstructures throughout a cast part are typically inconsistent, with grains varying from columnar to equiaxed [37]. Forging of metals is performed by pressing or hammering to shape a metal. One of the main disadvantages is that complex parts are difficult to obtain. However, because of the plastic deformation that occurs on the material, the parts are usually much stronger than cast parts [37]. SPS heats materials more directly and quickly than other methods, such as casting, so it consumes energy more efficiently. The assistance of the applied pressure also decreases the required sintering temperature, further reducing its energy consumption. When used in conjunction with work-hardened feedstock material, SPS can be of great benefit in maintaining desired material properties as discussed in Chapter 1.

In the present study, 304L and Ti64 chips were packed into a graphite tooling set for SPS after preparation. Graphite spacers were used to protect the punches from the uneven and sharp chips. A layer of graphite foil lined the die and was placed in between the spacers and sample material to protect the tooling. All samples were uniaxially pressed from both the top and bottom to 1 ton and held for 5 minutes on each side. The samples produced with titanium chips were compressed with every 3 g addition of chips due to their spring-like structure that inhibited even packing by cold pressing.

The SPS of samples was performed using a Dr. Sinter model SPS-3.20MKIV. For all samples, applied force and heating rate were held at 5 kN and 100°C/min, respectively, with a 1 minute hold at 100°C to allow any residual water to evaporate and a 5 minute hold at the peak temperature. Voltage, current, specimen displacement, displacement rate, temperature, uniaxial force and environmental pressure were recorded continuously during sintering. After the sintering was completed, pressure was immediately released and samples were cooled in the chamber.

For 304L, a peak temperature of 1100°C was used to provide the best tradeoff between material properties and energy consumption, based on prior studies [38, 39]. For Ti64, peak temperatures of 950°C and 1250°C were used. Some studies reported that 950°C was the temperature required to achieve fully dense samples without passing the β-transus temperature [31, 40, 41]. Although it was expected that sintering the chips at higher temperatures (e.g., 1250°C) would inevitably consume more energy, a higher sintering temperature may be necessary to achieve a densification comparable to powders due to the lower surface area to volume ratio and irregular morphologies of the chips. In addition, Weston and Jackson found that samples sintered near this temperature had a more homogeneous microstructure, resulting in more uniform macroscopic mechanical properties [31].

After samples were sintered, a coarse 60 grit sandpaper was used to remove the surface layers containing graphite or titanium foil that penetrated the sample. Samples were then cut into four equal-sized pieces and each piece polished down to 0.05 μm using a diamond suspension. Powder X-ray diffraction (XRD), scanning electron microscopy (SEM), electron dispersive X-ray spectroscopy (EDS), nanoindentation and Vickers indentation methods were then employed for analysis.

2.3 Powder Formation Methods

Near-net shape (NNS) manufacturing methods such as additive manufacturing commonly require the use of powders as feedstock materials. Critical characteristics of the powders include flowability, composition - particularly oxygen content, particle size and particle size distribution [42]. When producing powders, the primary factors that affect flowability are the particle size and shape. In general, flowability decreases with decreased particle size because the increased surface area resulting from smaller particles increases the inter-particle friction. Gas atomization (GA) and plasma atomization (PA) are methods that produce the majority of titanium powders used in industry [42]. GA and PA particle sizes are typically in the 10-300 μm particle size range [42].

The processes of GA and PA are similar, with the main steps of the process being melting, atomization and solidification. Melting can be done with several methods including plasma arc melting, induction drip melting or vacuum induction melting. The liquid metal is then broken into droplets which solidify during their flight into a cooling chamber. GA uses a constant stream of inert gas to break up the liquid whereas PA uses plasma torches. The primary difference is that in PA, melting and atomization occur simultaneously, reducing the amount of solid materials the liquid metal comes in contact with and thus also reducing contamination [42]. Because of this, the yield for fine powders is higher with PA than GA - Ti64 powder produced with PA has a 40% higher yield than with produced with GA [42].

The constant stream of gas and high energy required for melting are two major factors of atomization that increase its environmental footprint. Currently, gas atomization of steel requires 1.94 kWh/kg [43] and that of Ti64 requires 1.95-8.81 kWh/kg [44]. To improve powder production through a sustainability perspective, this study will use ball milling as a potential alternative and more sustainable method for Ti64 powder production.

2.4 Ball Milling Methods

There are many varieties of ball milling but the premise for each is the same: some amount of feedstock material is fed into a chamber along with balls so that there is a fixed weight ratio of material to balls - also known as the ball to powder ratio (BPR). The contents of the chamber are spun around, either by the chamber spinning itself or by an arm located inside the chamber, and the repeated collisions of the balls with the feedstock material cause the particles to break down. This results in a reduction of particle size and can alter the particle shape, grain sizes and occasionally composition of the feedstock material.

Attrition mills have a rod situated inside the chamber that rotates to induce the collisions [45]. They can be easily adapted to have a constant flow of liquid nitrogen in contact with the feedstock or within a cooling jacket around the chamber. However, the collision force varies from the edges to the center of the mill resulting in a lower yield of usable powder [36] and it has the lowest overall

energy transfer per collision [45]. A roller mill utilizes gravity to induce the collisions by spinning a cylindrical container around a horizontal axis [45]. However, smaller, laboratory-scale mills do not provide enough force of impact to reduce particle sizes [36]. Vibratory mills can be either 1D or 3D and will shake along one or three directions [45]. They are very effective in reducing particle size, but larger quantities of feedstock make it more difficult to use [36]. Planetary ball mills consist of multiple jars rotating on a common axis while simultaneously rotating on their own respective axis, similar to how planets orbit the sun [36]. The impact force in laboratory-scaled planetary ball mills is higher than each of the previously mentioned mill types [45], a higher volume can be used than vibratory mills, and a more consistent particle breakdown is offered compared to attrition mills [36]. The main drawback of planetary ball mills is the temperature regulation. Because the temperature increases with increased milling due to friction, they are often operated on an on/off duty cycle. The heat buildup can lead to cold welding, agglomeration, and a decreased yield of powder [36]. Due to these reasons and feasibility for scaling up to the industry scale, planetary ball mills were used for this study

2.4.1 Ball Milling Environment

Ball milling can be performed in a variety of gases or liquids depending on the desired product. Titanium is well known for readily reacting with other elements such as oxygen, nitrogen, hydrogen and carbon, especially at elevated temperatures. Because of this, an inert environment is required. Air, water, argon, ethanol or liquid nitrogen (LN_2) are common ball milling environments [36]. Due to their ability to help maintain lower temperatures within the milling environment, LN_2, water and ethanol are often used to prevent cold welding of particles. Due to its cryogenic temperatures, LN_2 is also used to suppress the annihilation of dislocations within particles so that the overall dislocation density increases with increased milling, making for a stronger material [36]. Some materials will form metal nitrides when in contact with the LN2 which helps stabilize the ultrafine grain structure by pinning grain boundaries. This also aids in strengthening the material [2].

Process control agents (PCAs) can also be used to prevent cold welding of particles. The primary drawback to PCAs is that they introduce a source of contamination. Hydrogen is one of the largest contaminants of PCAs but can be removed by introducing a simple degassing step to the production procedure [36]. Stearic acid is a PCA commonly used with ball milling. Instead of helping maintain a lower temperature, it acts as a surfactant by coating particles, ultimately decreasing the cold welding. Only very small quantities of stearic acid are required to observe a large decrease in cold welding. Toluene is another common PCA used when wet milling that also prevents oxygen pickup. Because it is in a liquid state, heat buildup is much more gradual than with dry milling [46]. Because the intent of this study is to minimize chemical waste and maximize efficiency, the Ti64 chips were first ball milled in an argon environment to reduce oxygen pickup with the addition of stearic acid to prevent cold welding. Various amounts of stearic acid were tested to find the minimum quantity necessary for effective particle reduction. Chips were also ball milled in toluene to compare to those milled in stearic acid. To minimize the heat buildup within the jars, a 5 minute on and 5 minute off duty cycle was used for all ball milling as chosen by Fullenwider et al [36]. It was observed that cold welding significantly decreased using these time intervals compared to longer "on" times.

2.4.2 Ball Milling Parameters

A number of variables can be adjusted in a planetary ball mill to increase the milling efficiency. One of two primary influences of the energy transfer rate is the main plate rotation speed, which determines the frequency of ball-feedstock collisions. The second primary influence is the BPR, which determines how much energy is transferred during each collision [10]. In general, an increased BPR will result in less time required for milling. However, this also requires less feedstock material be used so there is a tradeoff between the time required to mill and amount of material produced. The amount that the jars are filled also affects the milling efficiency with a similar tradeoff as the BPR - filling the jars too little will result in a longer time required to ball

mill a given amount of material, but filling the jars too much will inhibit the movement of media. Thus, it is recommended that 50% of the jar volume be filled [10].

The planetary ball milling of Ti64 chips was performed in a PQ-N04 Across International (Livingston, NJ) planetary ball mill using hardened 100 mL (52 mm inner diameter) stainless steel jars. 6 mm diameter stainless steel balls were used at a 10:1 BPR. Approximately 50% of each jars volume was filled. The speed was set at 500 RPM and a 5 minute on/5 minute off approach was used to prevent the buildup of heat within the jars. In the investigation of ball milling Ti64 for powder production, the milling time, amount of PCA and type of PCA were varied to analyze how these conditions affect powder morphology evolution.

2.5 Sample Characterization

Ball milled powders were characterized by SEM, XRD and EDS. Spark plasma sintered samples were characterized by Archimedes density, XRD, SEM, EDS, Vickers indentation, and nanoindentation. These methods provide the measurements of particle size, grain and colony sizes, phase constitution, particle morphology, general chemical composition, and micro-scale mechanical hardness.

2.5.1 Phase Constitution

Sample phases were analyzed with XRD and SEM. XRD uses X-rays to determine atomic and molecular structure information about a crystalline material. A variety of data can be obtained from an experiment such as preferred crystal orientation planes, phases, average grain size, strain and crystal structure [47]. Material phases are based not only on chemical makeup, but also on atomic arrangement [48] making XRD an excellent technique for phase determination. Because of the short wavelength of X-rays, a resolution in the range of 0.1-10 Å can be achieved. Since the average spacing between atoms in a crystal lattice is on the order of a single angstrom, this makes X-rays especially useful for obtaining atomic-level data [49]. During an XRD experiment, X-rays that are generated with a cathode tube and copper system are directed at a sample. As the X-ray

detector rotates around the sample at specified angles of 2ϑ, the intensities of the X-rays that are reflected off the sample are recorded. At specific angles of rotation, Bragg's Law (Equation(2.1)) is satisfied and constructive interference of reflected X-rays occurs, increasing the intensity detected. All the X-rays that are detected are converted to a count rate, which appear as peaks. Each phase of each crystalline material has its own signature peak pattern that essentially consists of relative intensities and spacings between lattice planes [50]. These peak patterns are stored in databases where they can later be referenced.

$$2dsin\theta = n\lambda \tag{2.1}$$

Scanning electron microscopy (SEM) is an imaging technique that uses a high-energy electron beam to generate high-resolution topographical images of conductive samples. Due to the extreme detail that can be obtained from SEM, it is one of the most widely used analytical tools in industry [47]. An electron beam is generated and focused, then is rastored over a sample surface. As the electrons impact the sample, secondary electrons, backscattered electrons, and X-rays are emitted. When an electron impacts an atom from the sample, an electron within the atom is ejected. Because the impacting electron and ejected electrons have different momentums, a characteristic X-ray is also emitted in order to satisfy conservation of energy. To prevent a buildup of incident electrons on the sample, otherwise known as charging, the samples must be conductive, electrically grounded and kept in a high vacuum environment [51]. If a sample is nonconductive, it is often coated with a few nanometers of gold. The characteristic X-rays emitted by the SEM electron beam give way to energy dispersive x-ray spectroscopy (EDS), which is often used in tandem with SEM and can provide approximate compositional data about a sample. Because EDS is based on characteristic X-rays of elements, it can only provide elemental data and not chemical information [51]. The depth of analysis is typically 0.5-5 μm depending on the accelerating voltage of the beam [51]. The maximum penetration depth, $R_{K\text{-}O}$, can be calculated with the Kanaya-Okayama model given by Equation (2.2) [52]

$$R_{K-O} = \frac{27.6AE_0^{1.67}}{\rho Z^{0.89}} \tag{2.2}$$

where ρ is the target material density (g/cm^3), A is the target material atomic weight, Z is the target material atomic number and E_0 (keV) is the incident electron energy, which was held constant at 15 keV for the presented work. Prior to SEM and EDS, samples were hand polished down to 0.05 μm using a diamond suspension. This revealed the grains present on the surface and allowed the microstructures, which are determined by the phases, to be analyzed.

2.5.2 Indentation

Two types of indentation methods were used in the presented work - nanoindentation and Vickers indentation. Nanoindentation can measure mechanical properties such as wear, hardness and modulus at the nano-level. Because indents are on the size range of single microns in width, nanoindentation gives location-specific data that cannot be obtained with a larger tip such as Vickers. However, Vickers indentation can measure the hardness and fracture toughness at the micron-level and gives more representative data about how the material will behave at the macro-scale. This is especially important when considering the applications for a material. All samples were ground using SiC paper of 60, 80, 120, 600, and 800 grit sizes on an eight-inch grinding wheel spinning at 200 RPM. Each step was performed for approximately 10 minutes and an optical microscope was used to verify removal of deformation at each step. Polishing was then performed using 9 μm, 6 μm, 3 μm, 1 μm, 0.25 μm and 0.05 μm polycrystalline diamond media suspension on polishing cloth, each for approximately 30 minutes. Between each step of grinding and polishing the sample was cleaned using ultrasonication in de-ionized (DI) water to remove previous polishing media. After the final polishing step, ultrasonicating with a rotation of DI water, acetone and ethanol (each for 30 min) and a clean fluffed Q-tip was performed to remove any excess residue. A grid-like pattern was embedded across samples to ensure indentation was performed in various locations across the sample and prevent biases due to possible inhomogeneity. Scanning probe microscopy (SPM) imaging of each sample revealed an average roughness below 5

nm. Nanoindentation was performed on a Hysitron® TI Premier nanoindentation system with an anti-vibration table and enclosure as shown in Figure 2.4. The maximum load of the equipment is 10 mN with a resolution of 1 nN and a maximum displacement of 5 μm with a resolution of 0.04 nm. A Berkovich diamond probe (TI-0039 Berkovich, 142.3° total included angle, 100 nm tip radius) was used for all indentation tests. The hardness of samples was measured in order to investigate the relationship between processing method and material properties. To ensure accurate measurements, a tip area function calibration was performed on a standard sample of fused quartz with a known modulus and hardness value.

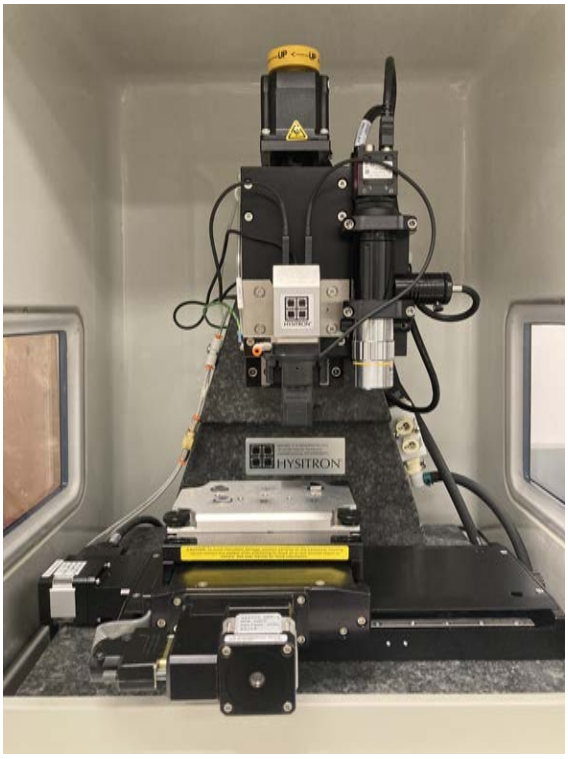

Figure 2.5: Hysitron® TI Premier nanoindentation system.

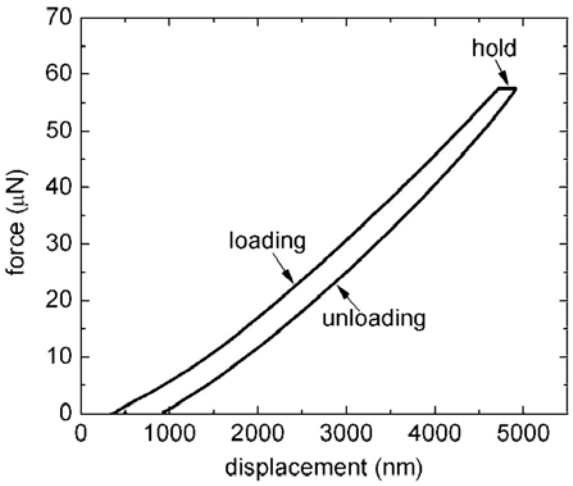

Figure 2.6: Force-displacement curve from a nanoindent showing the loading, hold at maximum force, and unloading segments [53].

All samples were indented with a 10-15-10 seconds load-hold-unload profile with a maximum force of 6 mN. During indentation, a force-displacement curve was generated, as exemplified in Figure 2.6. The hardness value was calculated with Equation (2.3) and is based on the maximum load, P_{max}, and the projected contact area, A [54]. To obtain statistically significant results, 10 sets each consisting of 9 indents were performed on each sample for a total of 90 nanoindents per sample.

$$H = \frac{P_{max}}{A} \tag{2.3}$$

Vickers indentation was performed on each sample under a 9.8 N load with a 15-10-15 second load-hold-unload increment. Indents were spaced five times the indent diameter from one another to comply with the ASTM standard of 2.5 times spacing that ensures neighboring indents do not affect one another due to any work hardening that may occur during indentation. 20 Vickers indents were performed on each sample.

The indentation size effect (ISE) is a well-established phenomenon that must be considered during, and especially when using two different methods of, indentation. This effect shows itself "as an increase in hardness with decreasing depth of penetration and becomes important at depths

of less than approximately 1 μm" [55]. The Nix & Gao model is the most widely used model that explains this effect [55]. This model assumes that there are dislocations statistically stored throughout a material in addition to dislocations that are necessary near the indentation region in order to accommodate the displacement of material [55]. In general and at the specified depth of around 1 μm, the deeper that an indentation penetrates into a sample, the more dislocations it will interact with and the hardness will decrease. Therefore, it is expected that the nanoindentations that displace into the material on the order of a few hundred nanometers will have a higher hardness than the Vickers indents.

2.5.3 FEM of Tensile Mechanical Behavior

Tensile testing was simulated on the Ti64 to address future work that predicts the mechanical properties of the sintered recycled chips. A wide variety of information can be obtained from tensile testing that tells how a material will behave under stress. These include elastic modulus, yield strength, ultimate tensile strength, and fracture toughness. During tensile testing, the two squared ends of the dogbone (Figure 2.7) are clamped into the grips of the tensile testing apparatus. An extensometer is placed onto the gauge to measure the amount of strain. The grips of the tensile tester extend uniaxially away from one another, stretching the dogbone specimen out along the direction of the gauge. The applied force and strain are measured and a stress-strain curve is generated based on Equations (2.4) and (2.5). Based on the cross-sectional area of the gauge, A_c, and the force, F, the engineering stress, σ_e, is calculated with Equation (2.4). The engineering strain, ε_e, is calculated using the initial gauge length, l_0, and the instantaneous gauge length, l, as in Equation (2.5).

$$\sigma_e = F/A_c \tag{2.4}$$

$$\epsilon_e = l/l_0 \tag{2.5}$$

In order to better predict a material's tensile behavior independently of dogbone dimensions, finite element modeling (FEM) was used to simulate the tensile testing of Ti64. A dogbone specimen similar to what is produced was created for the model. To simulate a structural defect, a small pore was created along the gauge length as indicated by the arrow in Figure 2.7.

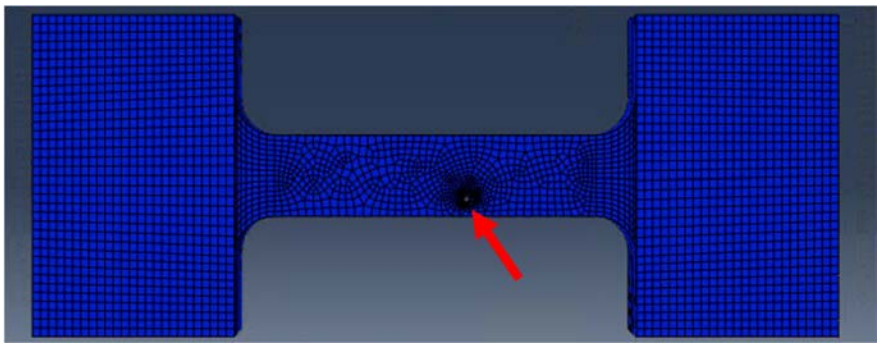

Figure 2.7: Dogbone specimen used in FEM model. Red arrow points to a small pore-like defect.

Table 2.3 provides a summary of the parameters used to simulate the tensile test. The part was assumed to be a homogeneous solid. Figure 2.7 shows the meshed dogbone specimen before starting the model. One end of the dogbone was fixed in position while the other end was set to displace uniaxially towards a reference point. The elastic deformation data and relevant material properties such as Young's modulus, Poisson ratio and mass density were input from database values [56]. Plastic deformation data was obtained from published Ti64 tensile test results [57] using a strain rate of 4.68×10^{-5} s^{-1}. Values for stress and strain in the plastic region were extrapolated from an experimental stress strain curve by [57] at strain increments of 0.01, from yield to fracture. The fracture energy per unit area was calculated by dividing the area under the necking region of the experimental stress-strain curve by the size of each element in the gauge.

Table 2.3: Input variables and parameters used to simulate tensile testing with FEM.

Parameter	Value
Young's Modulus	113.8 GPa [56]
Poisson ratio	0.3
Mass density	4430 kg/m^3 [56]
Strain rate	4.68×10^{-5} s^{-1} [57]
Strain at fracture	0.15 [57]
Fracture energy	2140 N/m [57]

2.6 Analysis of Energy Consumption

One of the goals of the presented work is to evaluate the environmental impact of the recycling methods used. Green engineering encompasses an entire product's life cycle, from the production of virgin materials and manufacturing of materials to usable parts, to the end of its life. The presented work focuses on eliminating the extraction of virgin materials by recycling materials at the end of their life. In order to make sure the presented method is more environmentally-friendly, certain metrics must be measured throughout the process. The energy consumption of ball milling is monitored by a power meter plugged directly into the same outlet as the ball mill. SPS energy consumption is tracked by the continuously measured current and voltage during sintering. Instantaneous power output is calculated by the measured voltage multiplied by the measured current. The total power is the sum of these products, which is then integrated over the total sintering time to obtain energy consumed. Specific energy consumption (SEC) is the total energy divided by the mass of the sample. The majority of the chemical waste was also monitored by measuring the use of acetone in cleaning the Ti64 chips and amounts of both stearic acid and toluene needed for ball milling.

Chapter 3

Spark Plasma Sintering of Stainless Steel Machining Swarf With and Without Addition of Powder

Previous research showed that stainless steel 304L machining swarf could be recycled and converted to powder by ball milling, with characteristics that are useful as feedstock in additive manufacturing (AM), specifically laser directed energy deposition [36]. Compared to producing virgin gas atomized powder as the feedstock for AM, this method of converting recycled chips to powder was more cost-effective and environmentally friendly because of reduction in material waste and energy consumption. However, the process window of ball milling was relatively narrow to achieve the desired powder morphology and size in AM. Specifically, two-stage ball milling with a total milling time of 60 hours was required to achieve a near spherical powder with a particle size range of 38–150 μm. In addition, a phase transition from austenite to martensite occurred in the ball milled powder due to severe plastic deformation. To increase the flexibility of recycling and reusing the machining swarf, SPS was explored to consolidate machining swarf directly without the step of ball milling. The hardness of the bulk samples made from the swarf was evaluated in comparison to industry standards to verify the feasibility of using swarf as feedstock in SPS. To overcome the challenge of packing machining swarf due to their irregular shape and large size, which leads to limited chip-to-chip surface contact area, gas atomized (GA) powder was added to the swarf as a sintering aid. The microstructure of the samples made from the mixture of powder and swarf was compared to the counterparts consisting of 100% swarf. Therefore, this chapter provides the findings of using SPS to recycle stainless steel chips with and without the addition of gas atomized powder.

3.1 Phase Constitution and Microstructure

Figure 3.1 shows the overview of representative samples made from 100% machining chips and a blend of 50 wt% chips plus 50 wt% GA powder, respectively, via SPS using identical processing parameters. These two types of samples are referred to as SS-100 and SS-50, respectively, hereafter, where the first S stands for stainless steel, the second S stands for swarf, and the number means the weight percent of the swarf in the feedstock.

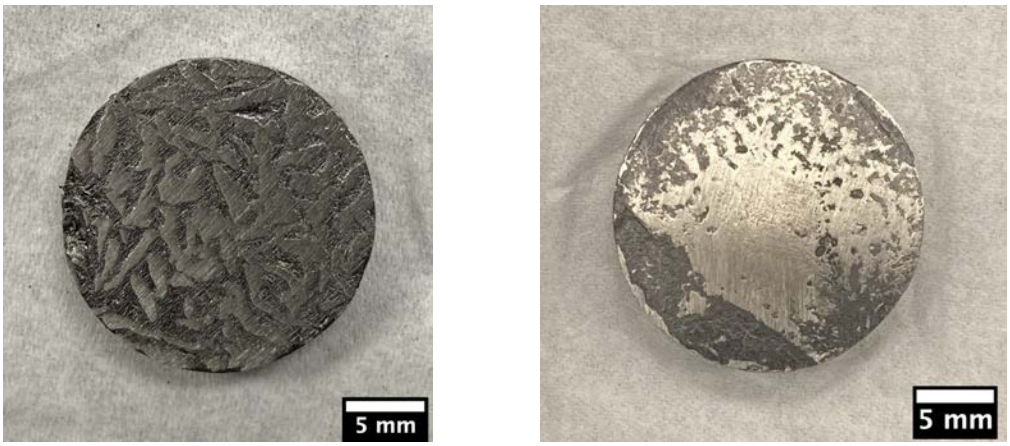

(a) **(b)**

Figure 3.1: Images of sintered samples made from (a) 100% nibbled chips (SS-100), and (b) 50 wt% nibbled chips and 50 wt% GA powder (SS-50).

3.1.1 Phase Constitution

To start with, the phase constitution of the gas atomized powder, nibbled chips, and SPS'ed samples (SS-100 and SS-50) were analyzed, as shown by the XRD patterns in Figure 3.2. As expected, the GA powder exhibited the austenite phase, while the nibbled chips exhibited primarily the austenite phase with the presence of a small amount of martensite phase. The martensitic formation resulted from the repeated plastic deformation during nibbling, causing a diffusionless phase transformation by straining the face-centered cubic austenitic lattice to a body-centered tetragonal lattice. This phase transition in stainless steels has been well established in the literature [13, 14, 58]. In addition, peak shifting and broadening was observed for the austenite and

martensite phases in the nibbled chips, which resulted from the cold working that occurred during machining. The repeated impacts and plastic deformation caused a residual stress and strain in the chips, leading to the slight peak shifting in XRD patterns.

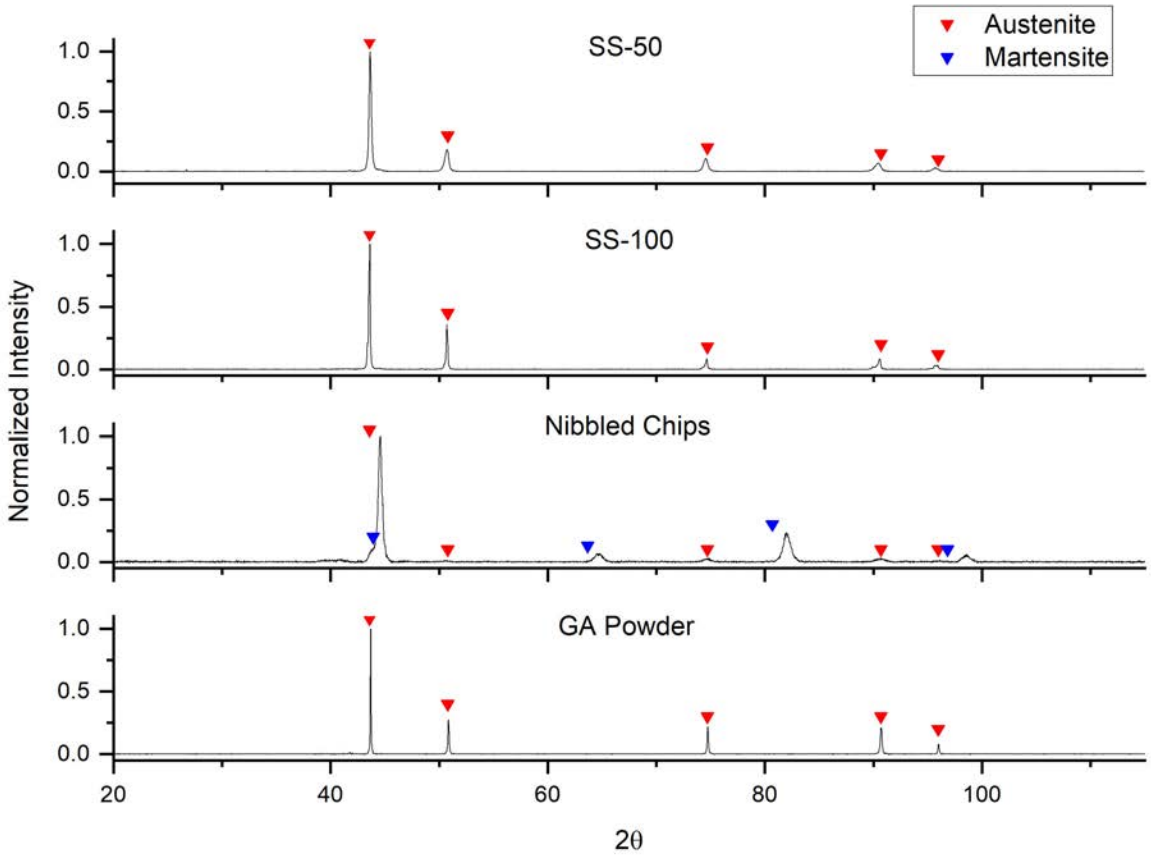

Figure 3.2: XRD patterns of (from bottom to top) the gas atomized (GA) powder, nibbled chips, SS-100 and SS-50.

After SPS, both SS-100 and SS-50 only exhibited the austenite phase. The thermal exposure during SPS led to the recovery of the lattice strains accumulated from the nibbling process, and subsequently, the martensite phase transited back to the equilibrium phase - austenite, according to the Fe-C phase diagram. Compared to the GA powder, peak broadening was also observed in the SPS'ed bulk samples, which indicated that the SPS'ed samples had a finer grain size.

3.1.2 Pore Structure

The density of SS-100 was 7.19 g/cm^3 (90% relative density) based on Archimedes' method. The microstructure of SS-100 contained several irregularly shaped pores with a size of a few hundred microns, as shown in the overview of the microstructure in Figure 3.3a. Those relatively large pores were formed due to local poor packing of the chips due to their irregular surface shape (shown in Figure 2.2 in Chapter 2). Micropores, with a length of $\sim$ 10 μm, were also observed at chip-chip boundaries. Those micropores were attributed to lack of surface diffusion due to the smaller chip-chip contact surface area than that of powders for the same volume.

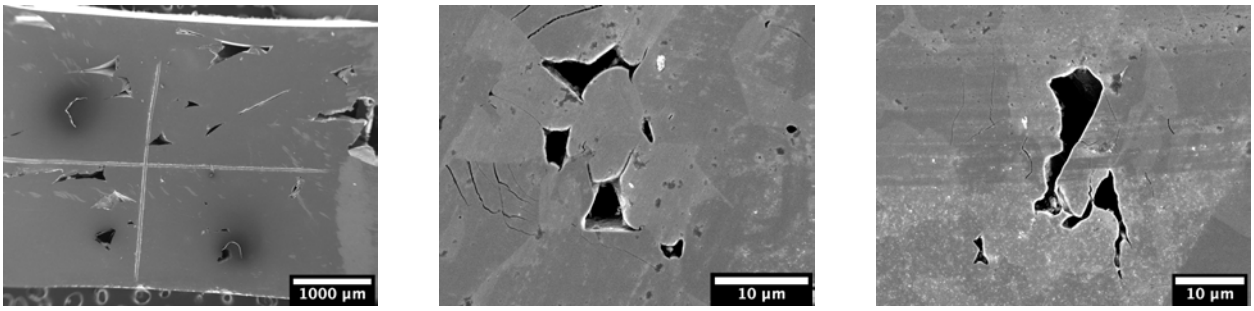

(a) **(b)** **(c)**

Figure 3.3: SEM images of the pores in SS-100. (a) overview, (b) and (c) representative micron-sized pores at chip-chip boundaries. Note: the two large scratches in (a) were intentional for marking locations along the sample.

The density of SS-50 was 7.06 g/cm^3 (88% relative density) based on Archimedes' method. The pore structure of SS-50 is displayed in Figure 3.4. Comparing Figure 3.3a and Figure 3.4a, SS-50 did not contain the large pores (a few hundred microns) as observed in SS-100. However, the smaller pores ($\sim$ 10μm) in SS-50 were more frequently dispersed throughout the sample than those exhibited in SS-100. Despite that solid-state sintering was achieved between chips and powder, the regions consisting of the chips are easily distinguishable from the regions consisting of powder particles in the sintered sample. The micropores were predominantly present in the regions consisting of the gas atomized powder particles (Figure 3.4b), while some were also observed between individual chips (Figure 3.4c).

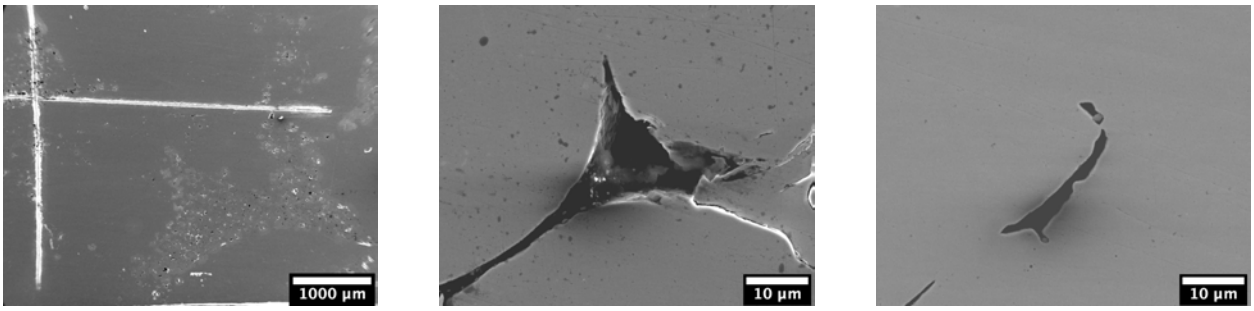

(a) **(b)** **(c)**

Figure 3.4: SEM images of the pores in SS-50. (a) overview, (b) and (c) representative micron-sized pores at particle boundaries. Note: the two large scratches in (a) were intentional for marking locations along the sample.

The elimination of sub-millimeter pores in SS-50 suggested that the addition of the gas atomized powder significantly improved the packing efficiency and effectively acted as a sintering aid to fill in the cavities among chips. Increasing the applied pressure or temperature during sintering would enhance the mass diffusion and therefore facilitate further closure of pores. However, unless the temperature exceeds the melting point, the pore closure will reach a limit and no more perceivable change will occur even with increased temperature or pressure because of an equilibrium concentration of vacancies, which increases with temperature, will be reached [59].

3.1.3 Grain Structure

Figure 3.5 displays the microstructure of a relatively pore-free region in SS-100. The majority of the grains throughout SS-100 were equiaxed in shape (Figure 3.5a). The average grain size was 51.36 ± 24.92 µm. Figure 3.5b shows a representative EDS result of a line scan across two neighboring equiaxed grains. The slight fluctuations in the intensities of different elements were due to background noise. Despite the contrast difference among individual grains shown in the SEM due to different grain orientations, the equiaxed grains are indistinguishable in chemical compositions. A distinct region (highlighted by the red dash lines in Figure 3.5a) exhibited dark-gray particles rather than clear equiaxed grains. EDS results (Figure 3.5c) confirmed that these

dark-grey particles are rich in Cr and C, while the light-grey region surrounding these dark particles exhibited almost the same composition with the equiaxed grain regions.

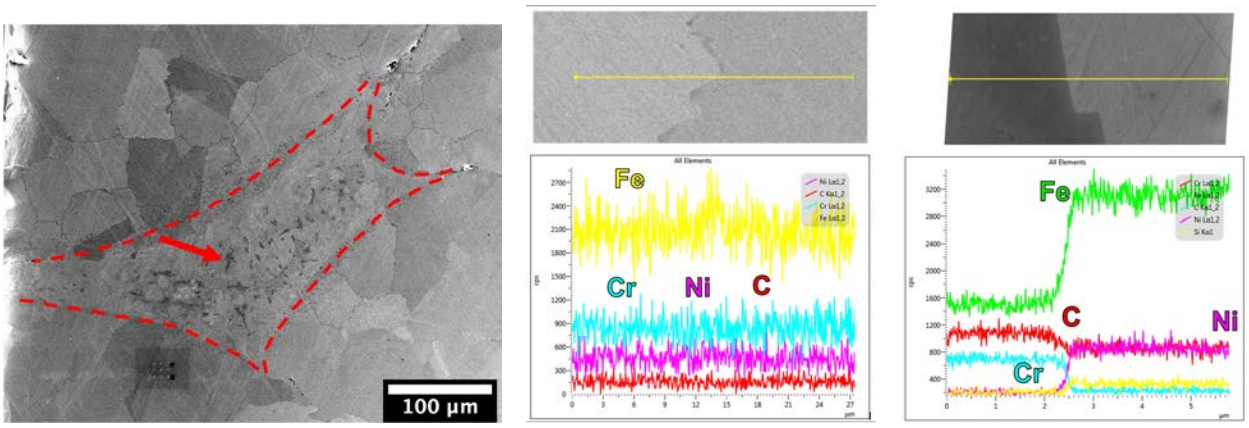

(a) **(b)** **(c)**

Figure 3.5: (a) SEM image the microstructural differences between the two types of regions on the SS-100sample, indicated with red dashed line, (b) EDS line scan result across two neighboring austenitic grains, and (c) EDS line scan result across a chromium carbide indicated in (a).

Segregation of chromium and carbon to grain boundaries to form chromium carbide precipitates, known as sensitization, occurs when a stainless steel is held at a temperature of 425-815°C, making it susceptible to intergranular corrosion. In 304L austenitic steel, the solubility limit of carbon in the FCC iron lattice is exceeded. As the temperature was increased during sintering, carbon tended to diffuse to the disordered, high-energy areas such as surfaces and grain boundaries. Chromium has a high affinity for carbon, and hence, it is drawn from the lattice towards the carbon-rich grain boundaries, forming chromium carbides (commonly $Cr_{23}C_6$) [60, 61]. Since chromium is the primary element in stainless steels that prevents corrosion, local chromium-depleted zones that are immediately adjacent to the carbides become more susceptible to stress corrosion cracking [62, 63]. Many austenitic stainless steels are susceptible to sensitization above 450°C, particularly along grain boundaries where there is more diffusion [63]. In SS-100, this was observed along grain boundaries and chip-chip surfaces.

The microstructure of sample SS-50 is characterized by three different types of regions, as schematically shown in Figure 3.6a. A representative SEM image of Region 1 - chip bulk (green box in Figure 3.6a) is shown in Figure 3.6b. Region 2 (blue box in Figure 3.6a) is shown in Figure 3.6c where a single chip's surface intersects with a pocket of powder particles. The circular outlines of individual powder particles, as well as grain boundaries within powder particles, can be distinguished here by the precipitation of chromium carbides. The average grain size in this Region 2 was 23.87 μm, with half of the measured grains ranged from 13.72 μm to 29.10 μm, smaller than the grains SS-100 sample. Figure 3.6d shows the microstructure of Region 3, referred to as pockets of gas atomized powder that were positioned between chips, as shown by the red box in Figure 3.6a. The GA powder region was not fully densified, although necks had formed between powder particles.

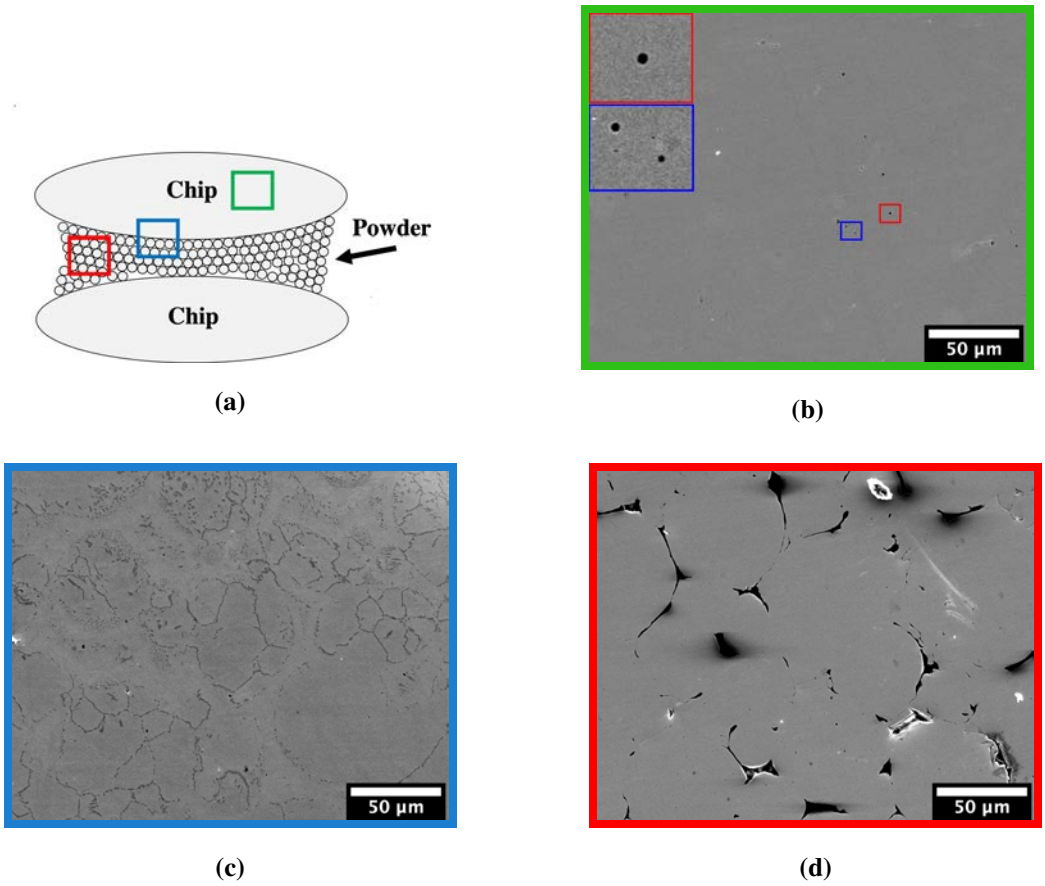

Figure 3.6: (a) Representative diagram showing the three different types of regions on the SS-50 sample and SEM images showing regions of (b) chip bulk (Region 1), (c) the interface between chips and pockets of GA powder (Region 2), and (d) pockets of GA powder (Region 3).

The chip bulk region (Figure 3.6b) exhibited microstructural features of ultrafine (diameter of $\sim$1 µm) black spherical particles, which were also observed in the cross-sectional microstructure of the SS-100 sample, but with a non-spherical shape. SEM images of SS-100 and the corresponding EDS results demonstrated that these ultrafine dark irregular particles were mostly present near chip-chip interfaces, leading to a distinguishable border around the chromium-carbide rich regions as seen in Figure 3.5a. In contrast, the black features were present in the interior of individual chips, with a more spherical shape and a lower number density, in the SS-50 sample. They were not observed in the GA powder pockets region. Based on the charging effect (brightening) on the edges, some of these black inclusions were identified as pores, as shown in Figure 3.7.

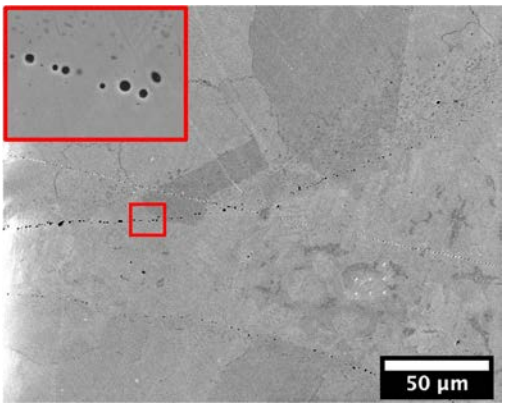

Figure 3.7: Inclusions bordering the chromium carbide-rich regions observed on the 100% chips sample. EDS map results shown in Figure 3.8.

The EDS mapping data shown in Figures 3.8 and 3.9 also showed that the black inclusions were primarily composed of silicon, manganese and oxygen. The higher counts in silicon, manganese, and oxygen in EDS can be explained by the higher driving force of diffusion near pores due to the free surface area of the pores. Segregation of these three elements is also relatively common in stainless steels [64, 65]. Increased amounts of oxygen are found on surfaces of stainless steels and, according to the Ellingham diagram shown in Figure 3.10, manganese and silicon both have an increased affinity to oxygen compared to the other alloying elements. This high affinity combined with the high driving force of diffusion towards the pore results in high levels of silicon, oxygen and manganese, as detected by EDS.

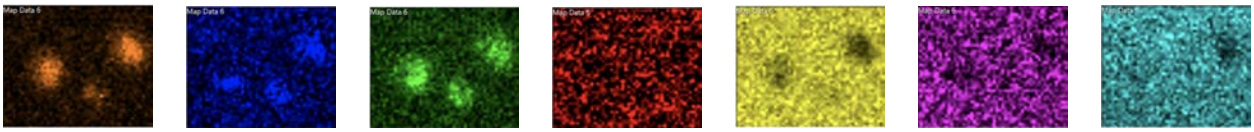

(a) Si **(b)** Mn **(c)** O **(d)** C **(e)** Fe **(f)** Ni **(g)** Cr

Figure 3.8: EDS map results from SS-100 of (a) Si, (b) Mn, (c) O, (d) C, (e) Fe, (f) Ni, and (g) Cr. Results clearly indicate an increase in silicon, manganese and oxygen at the black circular regions with a corresponding decrease in iron, carbon, nickel and chromium.

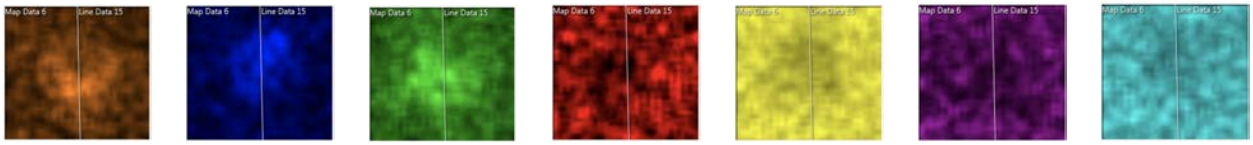

(a) Si **(b)** Mn **(c)** O **(d)** C **(e)** Fe **(f)** Ni **(g)** Cr

Figure 3.9: EDS map results from SS-50 of (a) Si, (b) Mn, (c) O, (d) C, (e) Fe, (f) Ni, and (g) Cr. Results clearly indicate an increase in silicon, manganese and oxygen at the black circular regions with a corresponding decrease in iron, carbon, nickel and chromium. Line across all scans is from the line scan taken in Figure 3.11b.

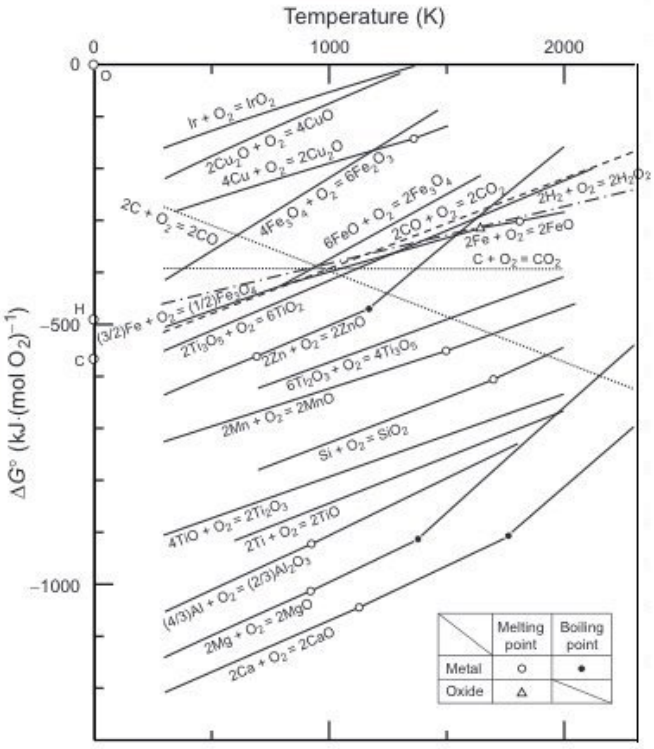

Figure 3.10: Ellingham diagram for some oxides. [66]

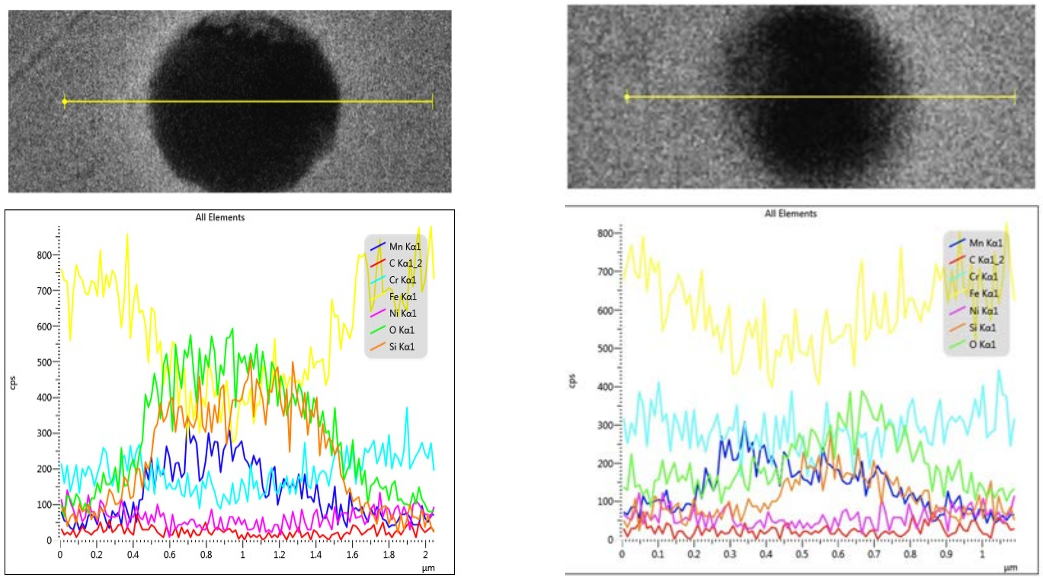

(a) **(b)**

Figure 3.11: EDS line scan results over dark circular inclusions on (a) SS-100 and (b) SS-50.

An alternative interpretation of the black inclusions, particularly those that did not exhibit the charging effect, would be precipitation of silicon and/or manganese oxides, which is a well-known phenomenon that occurs in austenitic steels. Saeidi et al. found that after laser melting 316L, there were circular nano-inclusions rich in Si, O and Cr [64] while Upadhyay et al. found similar inclusions rich in Si, Mn and O [67]. The nano-inclusions reported in those two studies closely resembled the ultrafine black inclusions observed in the present work. It was speculated that any oxygen take-up occurred during the laser melting because of a low amount of oxygen present within the chamber, which is similar to the vacuum environment during sintering. In addition, Laleh et al. reported similar oxide inclusions were rich in both Mn and Si when studying the localized corrosion rates of 316L samples produced by selective laser melting [65]. Similar to silicon and chromium, manganese also has a high oxygen affinity which explains its presence in the EDS results of the 304L samples in the current study [68]. The shapes of the EDS line scans shown in Figure 3.11 are consistent with the trend of line scans across precipitates taken by Upadhyay et al., Preston and Ma, Saeidi et al., and Khalaj et al. [64, 67, 69, 70]. Each line scan across an inclusion in both the presented and cited works has a high amount of curvature

as the scan moves into the inclusion, with the deepest part being near the middle. This indicates that the inclusions are nearly spherical, which is kinetically favorable for precipitates. Assuming the interface between the inclusion and the iron matrix is incoherent, the Gibbs free energy is proportional to the square of the volumetric strain associated with the incoherent interface. When the inclusions are spherical, the volumetric strain is minimized, leading to decreased energy [71]. The composition of 304L implies that there would be more manganese oxides than silicon oxides. However, the energy of formation must also be considered. Ellingham diagrams indicate that, regardless of temperature, manganese oxides have a higher free energy of formation than silicon oxides. Therefore, it is reasonable to presume that there are more silicon oxide precipitates in the samples than manganese oxide precipitates. A detailed analysis on the chemical compositions of individual oxides would need to be performed if quantitative effects of those oxides on the mechanical properties were to be sought, which is beyond the scope of the present work.

3.2 Mechanical Property - Hardness

Vickers indentation and nanoindentation methods were used to measure the hardness of the sintered samples at two different length scales. The results are summarized in Table 3.1, where the typical unit for Vickers indentation (HV) has been converted to GPa for a straightforward comparison to the nanoindentation results. Representative SEM images of Vickers indents and an array of nanoindents on the cross section of SS-100 are shown in Figure 3.12. The Vickers indent in Figure 3.12a and the two indents (1 and 2) in the top row of the array in Figure 3.12c are on the carbide-rich regions. The force-displacement curves corresponding to the array of the nanoindents in Figure 3.12c are provided in Figure 3.12d, where the red and blue curves are for Nanoindent 1 and 2, respectively.

Table 3.1: Average Vickers and nanoindentation hardness values from both 304L samples.

SS-100	**Vickers (HV)**	**Vickers (GPa)**	**Nanoindentation (GPa)**
Carbide region	879.34 ± 93.44	8.62 ± 0.92	6.69 ± 1.78
Non-carbide region	309.1 ± 52.0	3.03 ± 0.51	2.81 ± 0.40
SS-50	**Vickers (HV)**	**Vickers (GPa)**	**Nanoindentation (GPa)**
GA powder	79.59 ± 7.73	0.78 ± 0.08	3.69 ± 0.44
Chip bulk	179.59 ± 25.48	1.76 ± 0.25	4.54 ± 0.33
Chip-powder interface	262.25 ± 14.60	2.57 ± 0.14	4.65 ± 0.57

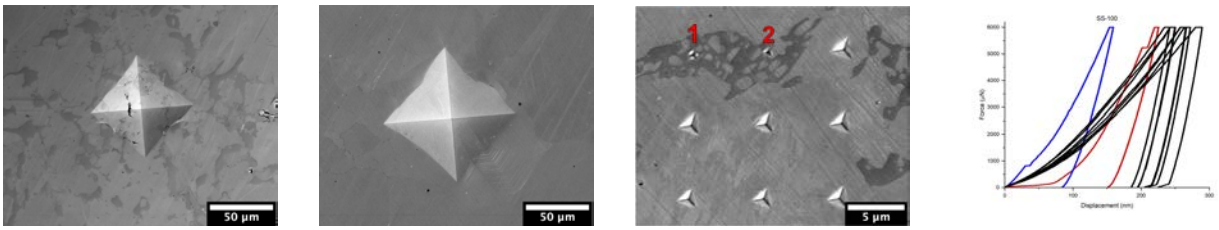

(a) **(b)** **(c)** **(d)**

Figure 3.12: Representative SEM images of (a) Vickers indent on a carbide-rich region, (b) Vickers indent on non-carbide region, (c) nanoindentation array, and (d) force-displacement curves corresponding to the nanoindentation array in (c). Red and blue curves correspond to nanoindents 1 and 2, respectively.

The average Vickers hardness of cast 304L is reported as 1.6 GPa [72] while the nanoindentation hardness are 2.93-3.94 GPa [73]. The present work showed that the hardness increased significantly with increasing chromium and carbon content compared to the non-carbide regions. The nanoindentation hardness values had a much wider range, 3.94-12.04 GPa for the carbide-rich regions and 2.01-5.27 GPa for the non-carbide regions, respectively, than the Vickers hardness, which ranged from 6.79-10.43 GPa for the carbide-rich regions and 2.24-3.92 GPa for non-carbide

regions, respectively. The greater variations in the nanoindentation hardness were attributed to the size (both deformation area and depth) of the indents. The plastic deformation depth of a nanoindent on SS-100 was approximately 300 nm and the length of the indent was $\sim$ 1 μm. Compared to a Vickers indent, which is typically a few microns in depth and approximately 100 μm in length, the nanoindentation hardness is more sensitive to the variation in microstructural features, such as thickness of precipitates and local compositional change.

The Vickers hardness values of SS-50 also varied widely depending on the location of the indents. In contrast, the variation in the average hardness values for the three regions obtained from nanoindentation were relatively small, with the Region 2 (chip-powder interface) exhibiting the highest hardness in SS-50. Representative SEM images of the Vickers indents in the three different regions and arrays of nanoindents are provided in Figure 3.13.

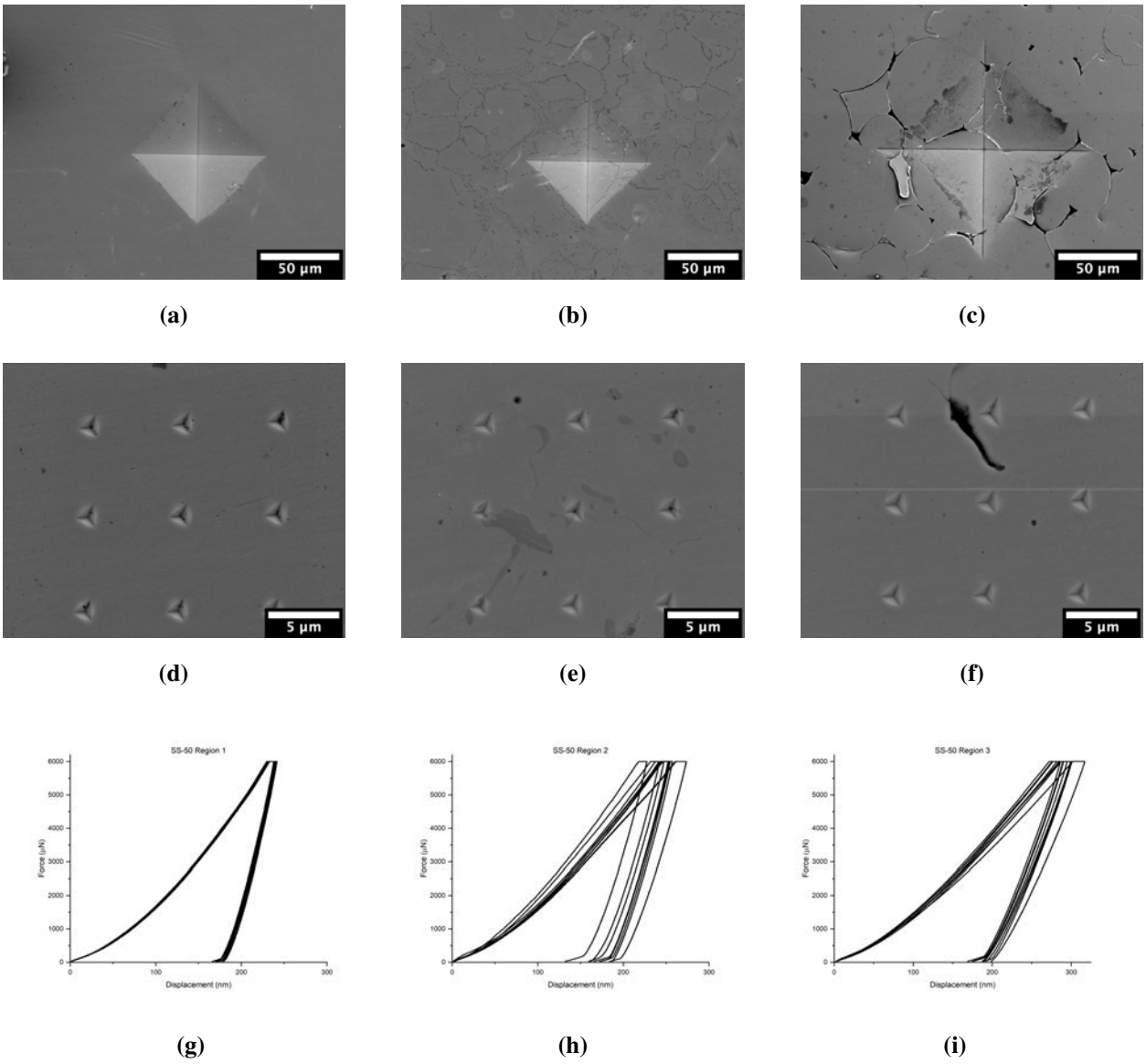

Figure 3.13: Representative SEM images of Vickers indents on (a) chip bulk, (b) chip-powder interface, (c) GA powder regions, respresentative SEM images of nanoindentation arrays on (d) chip bulk, (e) chip-powder interface, (f) GA powder regions with corresponding force-displacement curves in (g), (h), and (i), respectively on SS-50. Note the dark substance over the indent in (c) is surface-level contamination from a chemical on the Vickers indentation tip.

In general, the nanoindentation hardness values are higher than the Vickers hardness values which is explained by the indentation size effect described in Chapter 2. The chip bulk region and chip-powder interfaces exhibited higher hardness values than what was reported for cast 304L in the literature because of the presence of chromium carbide precipitates (Figure 3.6c) and potential

work hardening that the chips underwent during nibbling. The powder pocket regions in SS-50 had the lowest hardness, regardless of whether they were measured by Vickers indentation or nanoindentation. In addition, the non-carbide regions in SS-100 showed a higher Vickers hardness than the powder pocket regions in SS-50. This was because the powder pocket regions were not fully densified. Despite the fact that the grain size in the powders was smaller than the chip bulk area, the large amount of pores at the powder particle-particle boundaries decreased the hardness. Vickers indents are approximately 100 μm in length, covering larger areas that contain pores. The nanoindents are on the length scale of single microns, which gave a much lower chance to include pores in the subsurface. Moreover, the 9.8 N load from the Vickers indentation is also much higher than that from the nanoindentation, which reached a peak force of only 6 mN. Therefore, a larger volume of material was involved in the plastic deformation in the Vickers indentation, and it is more likely that pores, carbides or other inclusion are included in a Vickers indent area.

3.3 Environmental Assessment - Energy Consumption

Equations (3.1) and (3.2) can be used to calculate the theoretical energy required to heat (Q_1) and melt (Q_2) 1 metric ton (1000 kg) of 304L steel from room temperature. For 304L, the specific heat capacity, c_p, is 500 J/(kgC) [56], the latent heat of fusion, L_f, is 261 kJ/kg [74], and melting temperature is 1400°C [74]. The total theoretical energy to heat and melt 304L is therefore 948.5 kJ/kg, or 0.263 kWh/kg. Solid state sintering is often performed at temperatures below the melting point ($0.6T_m$), decreasing the amount of energy required to densify the steel based on theoretical calculations. However, reported SEC values for various manufacturing methods demonstrate that the amount of required energy consumption is highly dependent on the processing method.

$$Q_1 = mc_p\Delta T \tag{3.1}$$

$$Q_2 = mL_f \tag{3.2}$$

For example, induction furnaces are one of the most common methods used to melt materials, particularly for recycling. A number of variables can reduce the energy efficiency including from transmission systems, furnace radiation, and induction coils [75]. An induction furnace from the Coimbatore Foundry Cluster [75] that melts iron has a reported efficiency from 65% to 75%. Reported SEC values for melting and casting steel range from 4.72 kWh/kg [76] to 6 kWh/kg [77], where over half the energy cost is from melting [76]. After casting, the materials must undergo extensive machining to obtain a usable product. Additive manufacturing (AM) is a hot research field in recent decades because of its capability of near net shaping in one step, which reduces the multiple machining steps, also called subtractive manufacturing, to achieve complex 3D geometries. The feedstock material required for AM is usually produced via atomization, with an associated SEC of 1.94 kWh/kg for stainless steels [43]. Liu et al. reported the SEC to operate different AM machines. For example, the operation of an electron beam melting (EBM) machine consumes 22.2-166.7 kWh/kg and a direct energy deposition (DED) machine consumes 278-2,222 kWh/kg, where the energy consumption is highly dependent on the material feed rates [44]. It is important to note that those cited studies and the present work did not take into account any other resources required such as the constant stream of gas or water for atomization, inert gas for additive manufacturing or any coolant water used in machining.

During SPS, the time, voltage, and current were recorded continuously. The total energy consumption was estimated by integrating the power (voltage multiplied by current) over time, then divided by the sample mass to obtain the specific energy consumption (SEC). Plots of the power consumption are shown in Figure 3.14. The estimated SEC for SPS of SS-100 and SPS of SS-50 was 63.01 kWh/kg and 74.86 kWh/kg, respectively, with the mass of each sample being 20 g. It is necessary to note that the energy consumption of SPS does not linearly scale up with the mass of the samples that are sintered. For example, to SPS 100 g of 304L stainless steel using the same processing conditions with those used for SS-100 and SS-50, the SEC would range from 12.6 kWh/kg to 14.97 kWh/kg. In practice, the SEC for SPS would be much lower than what is reported on the laboratory scale because the occupancy of the furnace would be higher to maximize efficiency.

This demonstrates that not only is there an immediate energy savings compared to methods such as AM, but also a significant time savings since the SPS process occurs in a matter of minutes rather than hours. Recent research also proved the feasibility of making near net shape components via SPS [78]. In addition, providing more space for feedstock material by optimizing the graphite tooling, specifically the die, would also increase the efficiency of SPS.

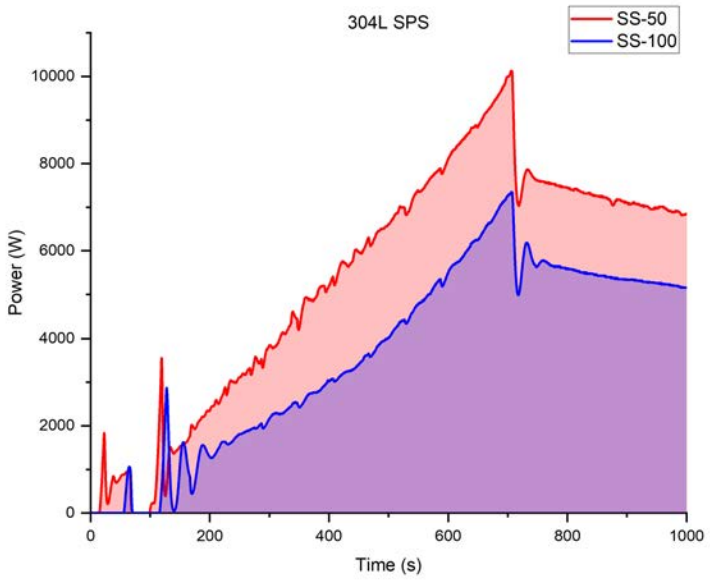

Figure 3.14: The graphs of power consumption versus time during SPS for SS-100 (blue) and SS-50 (red) samples.

The energy consumption to produce relevant tooling was not included in the present work, as other powder sintering techniques, such as hot press and hot isostatic pressing, use similar graphite tooling as SPS. The tooling sets are typically reused over several processing cycles, similarly to the molds required for casting. Therefore, the energy consumption associated with the tooling is assumed to be comparable among the aforementioned processing routes.

3.4 Summary

Stainless steel swarf collected from the nibbling process was successfully densified to bulk samples via SPS, which represents a more sustainable route to directly recycling metal machining swarf. It is proved that the swarf can be directly used as feedstock for SPS, without the need of ball milling to convert the machining chips to powder first. Despite the challenges resulting from the irregular surfaces of the swarf and the relatively large particle size, the samples made from SPS of 304L stainless steel swarf exhibited higher hardness than the cast counterparts. The higher hardness was attributed to the formation of chromium carbides, as well as the presence of ultrafine Si- and/or Mn- rich oxides. Pores remain a primary concern in the sintered bulk materials, which can be addressed via optimization of the SPS processing parameters, such as increasing applied pressure. Alternatively, gas atomized powder can be added to the swarf to improve the packing efficiency of the feedstock in the die, which subsequently facilitates an improvement in densification. However, the energy consumption associated with producing the powders needs to be considered for the strategy of adding powder as sintering aids. In comparison to traditional recycling methods, like purification and melting of the swarf (cast) to form ingots, the SPS approach not only gives rise to parts with higher hardness but also reduces the energy consumption and processing time. Moreover, the SEC of SPS is significantly lower than that of DED AM.

Chapter 4

Recycling of Ti-6Al-4V Machining Swarf

In addition to stainless steels, Ti-6Al-4V alloy, referred to as Ti64 hereafter, was of particular interest for energy-efficient recycling because of its high demand in industry and high production cost. The excellent strength to weight ratio of Ti alloys makes it attractive for structural applications, but the production of Ti alloys, particularly Ti64, is expensive, requiring multiple purification steps that result in high resource consumption. To reduce the cost and environmental impact, an alternative recycling method should be established to maximize efficiency. Based on literature review and the findings from the recycling of stainless steels via SPS in the present research, this chapter provides the results and discussion of SPS of recycled Ti64 machining swarf, including two different recycling methods and their viability - one involving SPS of swarf and the second involving conversion of chips to powders via ball milling before sintering.

4.1 Spark Plasma Sintering of Chips

The as-received (AR) Ti64 chips contained some amount of long and curly/tangled chips, as shown in Figure 2.3, which led to difficult packing. To improve the packing of the chips for sintering, it is necessary to reduce the size and curvature of the AR chips, which can be done by a short time of ball milling or grinding using a mortar and pestle set. Therefore, the AR chips were milled for 15 minutes in a planetary ball mill using stainless steel media before sintering. It is important to note that the Ti64 feedstock for SPS remained in the form of chips despite the 15 minute ball milling. The chips after ball milling were packed into a 20 mm diameter punch by a cold press at room temperature, and then consolidated into bulk samples via SPS, using a heating rate of 100 °C/min to a peak temperature of either 950°C or 1250°C, and a 5-minute holding time at the peak temperatures. A uniaxial force was applied and held constantly at 5 kN (15.91 MPa for a 20 mm diameter disk sample). Table 4.1 summarizes the sample identifications along with relevant distinctions in the processing procedure. Figure 4.1 shows the overview of representative

samples made from 100% Ti64 machining chips via SPS using peak temperatures of 950°C and 1250°C. These two samples are referred to as Ti64-950 and Ti64-1250, respectively, hereafter, where the Ti64 refers to the material of the sample and the number indicates the peak temperature reached during SPS.

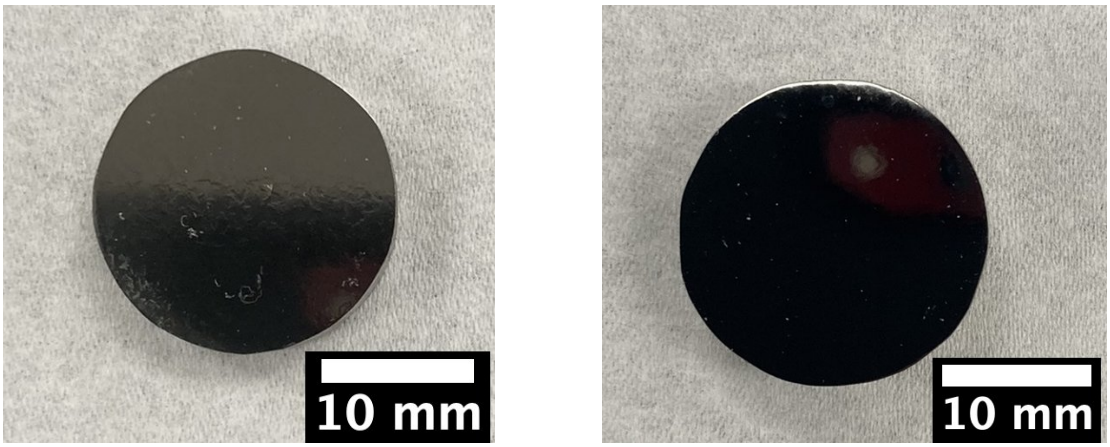

(a) **(b)**

Figure 4.1: Images of bulk samples made from Ti64 swarf via SPS at (a) 950°C, and (b) 1250°C.

Table 4.1: Sintered Ti64 sample IDs with relevant distinctions in processing. The peak temperature describes the maximum temperature reached during SPS that was subsequently held for 5 minutes.

Sample ID	Milling Media	Milling Time	Heating Rate	Peak Temperature (°C)
Ti64-950	stainless steel	15 minutes	100°C/min	950
Ti64-1250	stainless steel	15 minutes	100°C/min	1250

4.1.1 Phase Constitution

Figure 4.2 provides the XRD patterns of the AR Ti64 chips, the ball milled chips, and the sintered bulk samples. In all four patterns, the predominant phase is the HCP α-phase, with the presence of a minimal amount of the BCC β-phase. The patterns for the AR and ball milled chips

showed peak broadening and shifting, which resulted from the cold working that occurred during machining and milling. The plastic deformation resulted in a residual lattice strain that gives rise to peak shifting. Peak shifting was more severe in the ball milled chips compared to the AR chips. After SPS, both peak broadening and shifting were decreased. The thermal exposure during SPS, particularly for Ti64-1250, resulted in recovery of residual lattice strains and a limited amount of grain growth. In addition, the increased intensity in the β peak near 40° in the pattern for Ti64-1250 suggested that Ti64-1250 contained a higher amount of β phase than Ti64-950. This is expected as Ti64-1250 was sintered at a temperature higher than the β-transus temperature (990°C [31]).

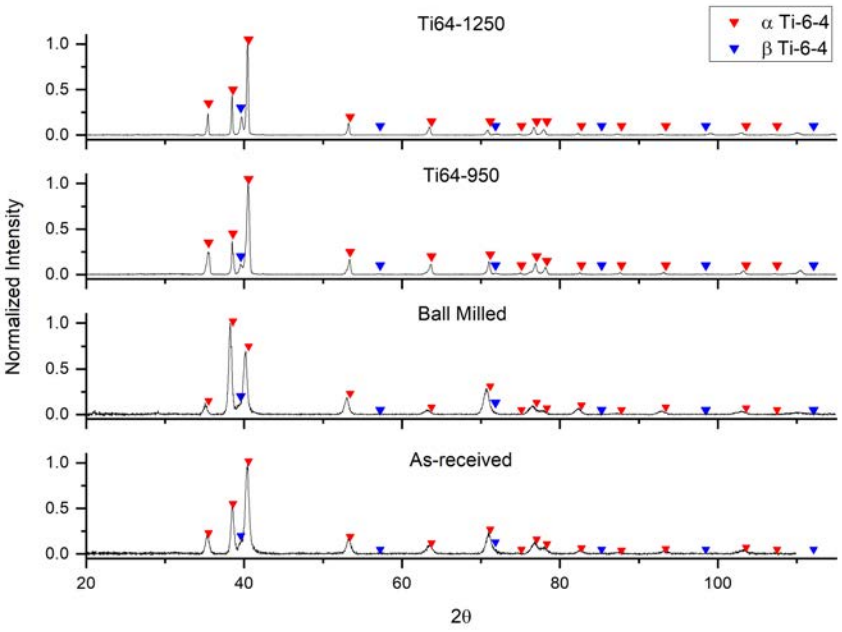

Figure 4.2: XRD patterns of, from the bottom upwards, the AR Ti64 chips, chips that were ball milled for 15-min. with stainless steel media, bulk samples sintered at 950C, and 1250 C.

In a pure Ti system, the α-Ti that is stable at room temperature undergoes a phase transformation to β-Ti around 882°C [79]. However, because the β transus temperature is strongly dependent on both substitutional and interstitial elements [80], the addition of aluminum and vanadium stabilizes the α and β phases, respectively. In the case of Ti64, the β-transus temperature is between 975-995°C [80].

4.1.2 Density

The densities of the sintered Ti64 bulk samples are provided in Table 4.2. Overall speaking, the porosity in the SPS'ed Ti64 samples was lower than that in the SPS'ed 304L samples. Representative SEM images showing pores in Ti64-950 and Ti64-1250 are shown in Figure 4.3 where Ti64-950 had several larger pores as shown in Figure 4.3a along with many smaller ($\sim$10 μm) pores like those in Ti64-1250 shown in Figure 4.3b. The Ti64 chips generally had a flatter, plate-like morphology whereas the nibbled 304L chips were thicker and larger (Figures 2.3 and 2.2). The thinness of the Ti64 swarf relative to the thick 304L stainless steel chips from nibbling, and the ductility of Ti64 allowed plastic deformation to occur more easily, therefore allowing for better packing during cold pressing. Table 4.2 also shows that an increase of 300°C in sintering temperatures led a slight increase in relative density. These measurements only provided the overall relative densities. The presence and distribution of pores were further characterized by SEM.

Table 4.2: Densities of samples sintered from Ti64 swarf. Percentages are the relative density compared to full density.

Sample ID	Geometric Density (g/cm^3)	Archimedes Density (g/cm^3)
Ti64-950	4.32 (97.59%)	4.21 (95.09%)
Ti64-1250	4.36 (98.51%)	4.34 (97.89%)

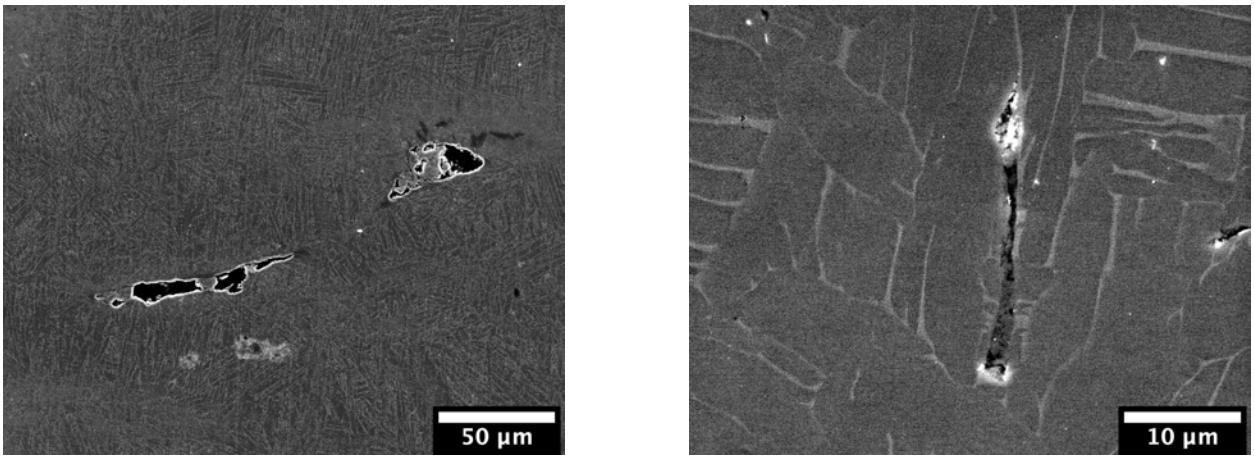

(a) **(b)**

Figure 4.3: SEM images showing representative pores observed in (a) Ti64-950 and (b) Ti64-1250 samples.

4.1.3 Grain Structure

Figures 4.4a and 4.4b show that the Ti64-950 and Ti64-1250 samples exhibit the typical α-β lamellar microstructure that is commonly reported for Ti64. Individual grains are distinguished by the dark α phase surrounded by the lighter β phase. The lighter regions are rich in vanadium, the β-phase stabilizer, while the darker regions are rich in aluminum, the α-phase stabilizer. The elemental distribution in the regions with different contrasts (dark grey vs. light grey) was verified via EDS (Figure 4.5). Colonies are also distinguishable by continuous α grains that surround a number of shorter grains as outlined by the red dashed line in Figure 4.4b. The colonies are generally shaped similarly to the equiaxed grains of the primary α phase and are explained by the growth of the β phase within primary α grains as the sintering temperature reached and exceeded the β-transus temperature.

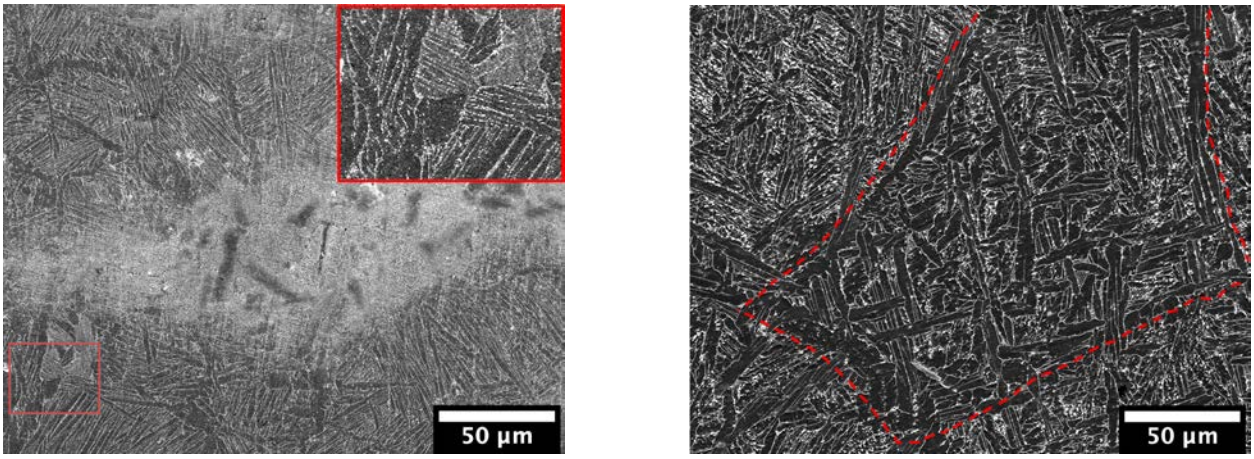

(a) **(b)**

Figure 4.4: SEM images showing microstructure of (a) Ti64-950 and (b) Ti64-1250 samples.

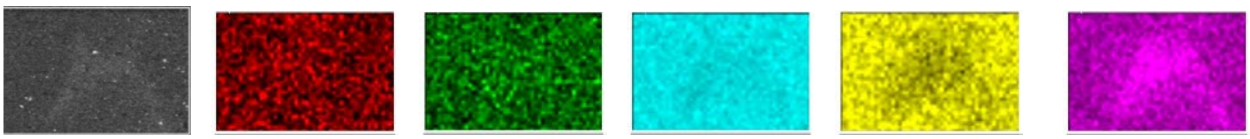

(a) SEM **(b)** C **(c)** O **(d)** Ti **(e)** Al **(f)** V

Figure 4.5: EDS map results showing increased vanadium (f) in lighter-contrasted areas surrounding darker α grains.

Figure 4.6 shows histograms of grain and colony sizes from each sample. The results are summarized in Table 4.3. The α grain size in Ti64-950 is similar to that observed in the AR chips shown in Figure 2.4, but smaller than the α grain size in the Ti64-1250 sample. It is not surprising to observe the trend that the grain size and the colony size increased with increasing sintering temperature.

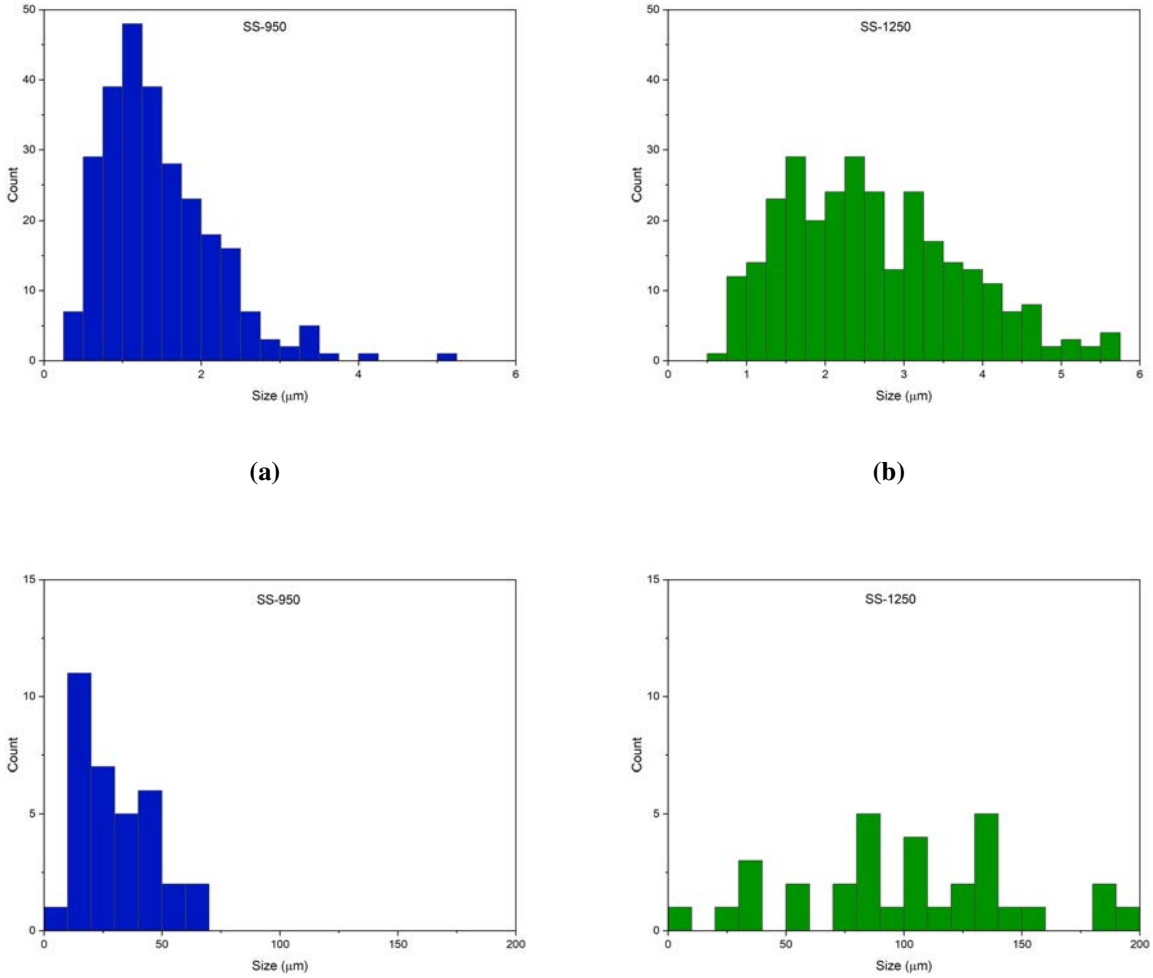

Figure 4.6: Histograms of α grain widths for (a) Ti64-950 and (b) Ti64-1250, and colony sizes for (c) Ti64-950 and (d) Ti64-1250.

Table 4.3: Average colony size, α grain size, and interlamellar spacing with standard deviations.

Sample ID	Colony Size (μm)	α Grain Size (μm)	Interlamellar spacing (μm)
Ti64-950	30.37 ± 15.14	1.39 ± 0.66	1.46 ± 0.71
Ti64-1250	104.37 ± 50.86	2.70 ± 1.32	3.99 ± 2.85

At higher temperatures, grain boundaries migrate to reduce the total number of grains, leading to an increased grain diameter, *d*. The average rate of grain boundary migration, $\bar{v}$, depends on the mobility, *M*, and diameter of the grain according to Equation (4.1)

$$\bar{v} \propto M\frac{2\gamma}{d} \tag{4.1}$$

where γ is the free energy associated with the boundary [71]. The grain boundary mobility is given by Equation (4.2)

$$M \propto \frac{1}{T}exp(\frac{-\Delta H^a}{RT}) \tag{4.2}$$

where ΔH^a is the atomic-level enthalpy [71]. It is clear because that the grain boundary mobility increases exponentially with temperature, grain growth is highly temperature-dependent as observed in the sintered samples.

Figure 4.4a shows a region that does not have the same fine, lamellar microstructure as its surroundings and is distinguished by being lighter in contrast. This type of region was observed throughout both Ti64-950 and Ti64-1250 and correlates with aluminum-depleted zones as shown by the EDS map results in Figures 4.7 and 4.8.

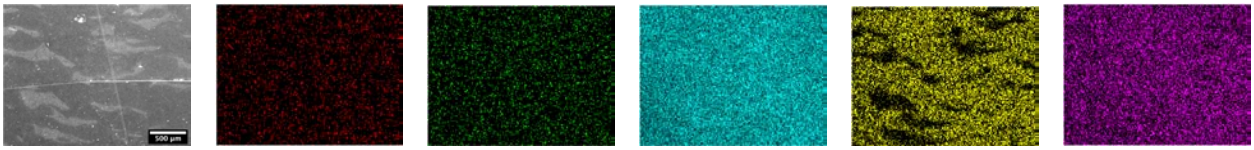

(a) SEM **(b)** C **(c)** O **(d)** Ti **(e)** Al **(f)** V

Figure 4.7: EDS results with (a) SEM image, (b) C, (c) O, (d) Ti, (e) Al, and (f) V elemental maps from a cross-section of Ti64-950. The two scratches in (a) are intentional to mark locations along the sample.

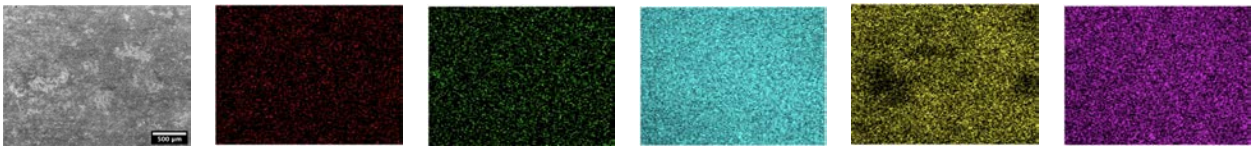

(a) SEM **(b)** C **(c)** O **(d)** Ti **(e)** Al **(f)** V

Figure 4.8: EDS results with (a) SEM image, (b) C, (c) O, (d) Ti, (e) Al, and (f) V elemental maps from a cross-section of Ti64-1250.

On the Ti64-1250 sample, the edges that define the aluminum-depleted regions are much less defined compared to those on the Ti64-950 sample which can be explained by the different diffusivities of aluminum and oxygen at the different sintering temperatures. Time-independent diffusivity, D, generally takes on the Arrhenius form given by Equation (4.3),

$$D = D_0 exp(-Q/RT) \tag{4.3}$$

where Q is the activation energy and R is the gas constant [24]. Multi-state diffusion and kinetic Monte-Carlo methods predicted the diffusion coefficient, D_0, of oxygen in α-Ti to be 2.036×10^{-6} m^2/s and the activation energy to be 183.612 kJ/mol [81]. As the temperature increases from 950°C to 1250°C, the interstitial diffusivity, D, of oxygen in α-Ti was measured to increase from from 3.67×10^{-14} m^2/s to 3.07×10^{-10} m^2/s [81]. The diffusivity of aluminum in α-Ti was also measured to increase from 1.07×10^{-13} m^2/s at 950°C to 1.28×10^{-12} m^2/s at 1250°C [82]. It is hypothesized that the aluminum-depleted regions align with the innermost "core" part of the individual chips. The Ellingham diagram in Figure 3.10 [66] shows that the affinity of oxygen to aluminum to form Al_2O_3 (alumina) is much higher than that of oxygen to titanium in order to form titania. In standard Ti64, there is a limited amount of oxygen present on the surface in the form of titania - whether it be rutile, brookite or anatase. Titania is initially formed on surfaces instead of alumina because of the higher atomic ratio of titanium to aluminum in Ti64. The movement of more oxygen atoms into the bulk of titanium is impinged by this surface oxide layer, giving titanium its corrosion resistance. During sintering, the mobility of the oxygen and aluminum atoms increased. At 950°C,

aluminum has a higher diffusivity than oxygen as previously described. Hence, the atoms present within the bulk of the chips diffuse towards the oxygen-rich surfaces. Consequently, the center of the chips became aluminum depleted, which then results in a kind of sensitization similar to the discussion on the carbon and chromium segregation in the 304L as discussed in Chapter 3. At 1250°C, the diffusivity of oxygen is increased to be higher than that of aluminum [81, 82] and the oxygen is able to diffuse inwards. This results in a less severe depletion of aluminum from the bulk of the chips. The size of the aluminum-rich regions, which has a composition closely resembling Ti64, corresponds to approximately the same size of the Ti64 chips, further indicating that the spacing between aluminum-depleted zones corresponds to the center of chips. The aluminum-depleted regions are significant because they show an increased Vickers hardness compared to the surrounding Ti64 as discussed in the following section.

Figure 4.9 shows one of 3-4 regions observed only on Ti64-950 that were ∼200 µm in diameter and consisted of the primary α phase (Figure 4.9b). This phase was not observed on Ti64-1250.

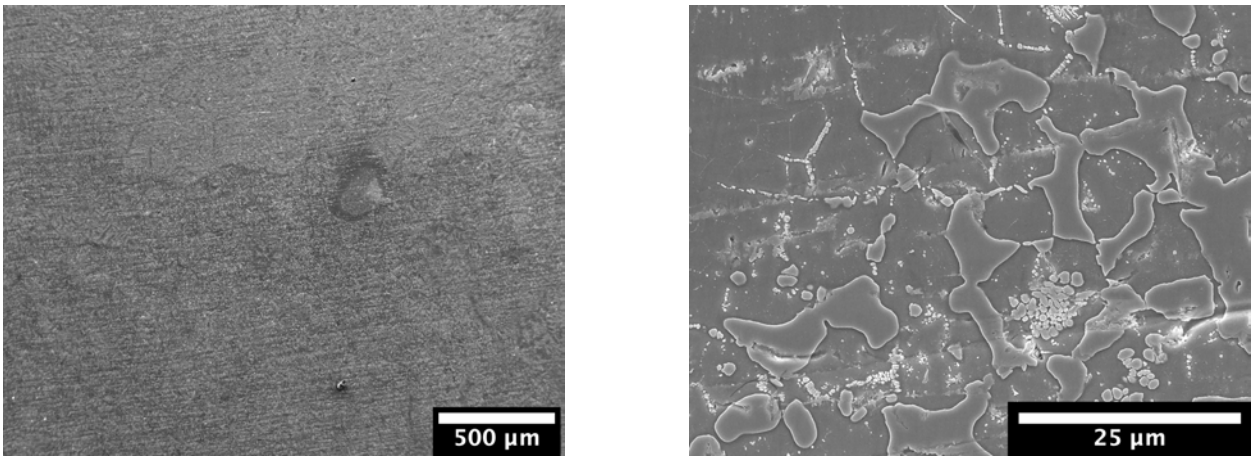

(a) **(b)**

Figure 4.9: (a) Overview and (b) magnified image of small region observed consisting of equiaxed grains on Ti64-950.

The α-phase regions in Figure 4.9 were only observed in the sample sintered below the Ti64 β-transus temperature, therefore they consist of the primary (or globular) α phase. The sample

sintered at 1250°C was expected to have fully transformed to the β phase prior to quenching, with nucleation of the α phase during the rapid cooling, which is observed with the basketweave microstructure in Figure 4.4. Since the sintering temperature for Ti64-950 was below the β transus point for Ti64, some nucleation of the α phase is expected.

4.1.4 Mechanical Property - Hardness

Nanoindentation and Vickers indentation was performed on the Ti64 samples. Figures 4.10a and 4.10d show representative SEM images of Vickers indents on Ti64-950 and Ti64-1250 samples, respectively, along with nanoindentation arrays shown in Figures 4.10b and 4.10e from Ti64-950 and Ti64-1250, respectively, with corresponding force-displacement curves in Figures 4.10c and 4.10f. Figures 4.10g, 4.10h and 4.10i show representative Vickers, nanoindent and force-displacement curves from the alumina-depleted regions on Ti64-950, respectively. The nanoindents boxed in Figures 4.10b and 4.10e are on pure α regions compared to those that are not boxed which that overlap α/β regions. The hardness results are summarized below in Table 4.4.

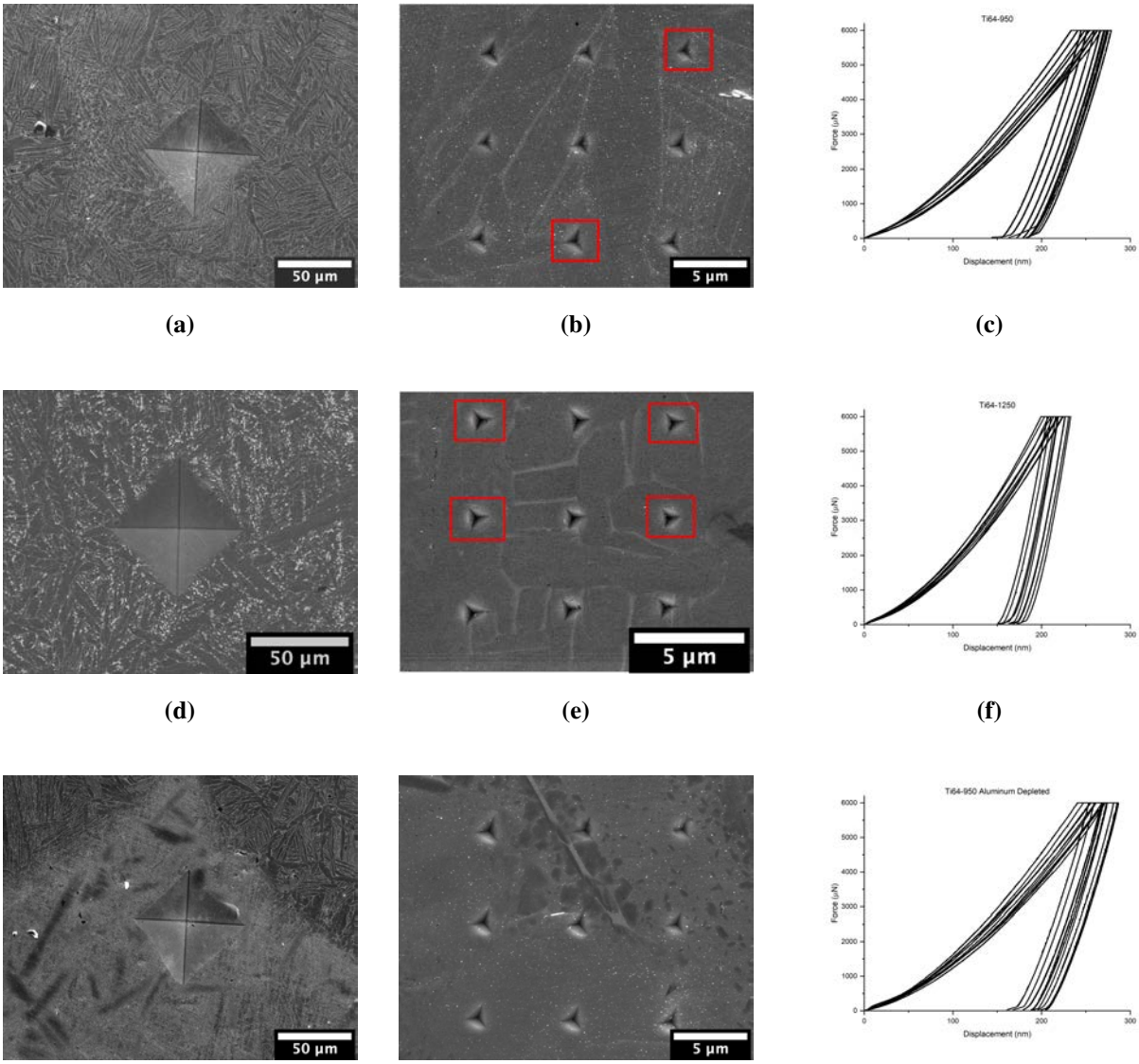

(a) **(b)** **(c)**

(d) **(e)** **(f)**

(g) **(h)** **(i)**

Figure 4.10: Representative SEM images of (a), (d), (g) Vickers indents on Ti64-950, Ti64-1250, and Al-depleted region on Ti64-950 respectively, (b), (e), (h) nanoindentation arrays on Ti64-950 and Ti64-1250, and Al-depleted region on Ti64-950 respectively, with respective force-displacement curves in (c), (f), and (i).

Table 4.4: Average Vickers and nanoindentation hardness values from Ti64-950, Ti64-1250 and aluminum-depleted regions with corresponding α grain sizes. Range of error is one standard deviation from the average.

Sample ID	Vickers (HV)	Vickers (GPa)	Nanoindentation (GPa)		α Grain Size (μm)
			α-region	α/β region	
Ti64-950	338.71 ± 19.67	3.32 ± 0.19	4.16 ± 0.66	4.62 ± 0.55	1.38 ± 0.66
Ti64-1250	408.85 ± 25.82	4.01 ± 0.25	5.29 ± 0.48	5.15 ± 0.46	2.70 ± 1.38
Al-depleted (Ti64-950)	365.32 ± 17.89	3.58 ± 0.17	4.00 ± 0.56		N/A

The increased hardness between nanoindentation and Vickers indentation can again be attributed to the size effect described in Chapter 2. A correlation was observed between the peak sintering temperature and hardness. Interestingly, the increased grain size of Ti64-1250 compared to that of Ti64-950 resulted in an increased Vickers hardness. According to the Hall-Petch relation given by Equation (1.1), an increase in grain size generally results in a decreased hardness. However, as the temperature is increased from 950°C to1250°C, the amount of the vanadium-rich β phase is increased. The hardness of the β phase is higher than that of the α phase, so increasing the amount of β-Ti by increasing the sintering temperature therefore also increases the hardness. The slightly increased relative density between Ti64-950 and Ti64-1250 also explains the increased hardness. Any residual porosity present from lack of surface diffusion between chips during sintering will decrease the hardness. Overall, there does not appear to be a difference in hardness values between pure α regions and α/β regions. Nanoindentation hardness for rolled Ti64 is reported at 4.1-5 GPa [83] and annealed Ti64 has a Vickers hardness of 349 HV (3.42 GPa) [56]. Compared to these values, the samples demonstrate a comparable hardness to rolled Ti64 and higher hardness than annealed Ti64. The chips were effectively cold-worked during machining and the short time used for SPS was not sufficient for annealing. Therefore, the hardness of the sintered samples is comparable to work-hardened Ti64 used in industry.

4.1.5 FEM Tensile Modeling

Finite element modeling (FEM) was used to predict the macroscopic behavior of spark plasma sintered swarf material under idealized conditions independent of sample dimension. The primary differences between commercially available Ti64 and recycled Ti64 that affect mechanical properties are compositional variation and presence of macro-scale defects like pores from chip serrations. To better understand the feasibility of using recycled materials, two tensile tests were modeled – one that represents an ideal, defect-free sample and the other with a pore (indicated by the arrow in Figure 4.12a). The results of the two tensile tests are shown in Figures 4.11 and 4.12, where Figure 4.11 shows the results of the ideal, defect-free specimen and Figure 4.12 shows that of a sample containing a pore-like defect. The colors indicate the amount of applied stress, with red being the highest near 109 MPa and blue being the lowest near 1.5 MPa.

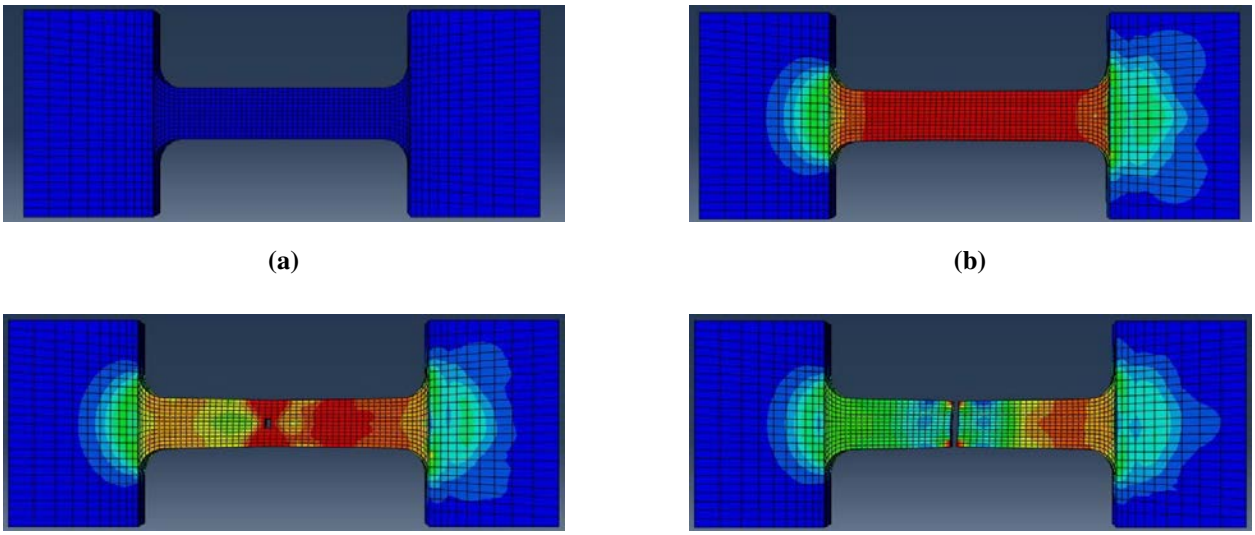

(a) **(b)**

(c) **(d)**

Figure 4.11: Results of simulated tensile testing with no pore (a) prior to testing, (b) prior to fracture, (c) initiation of fracture, and (d) complete fracture.

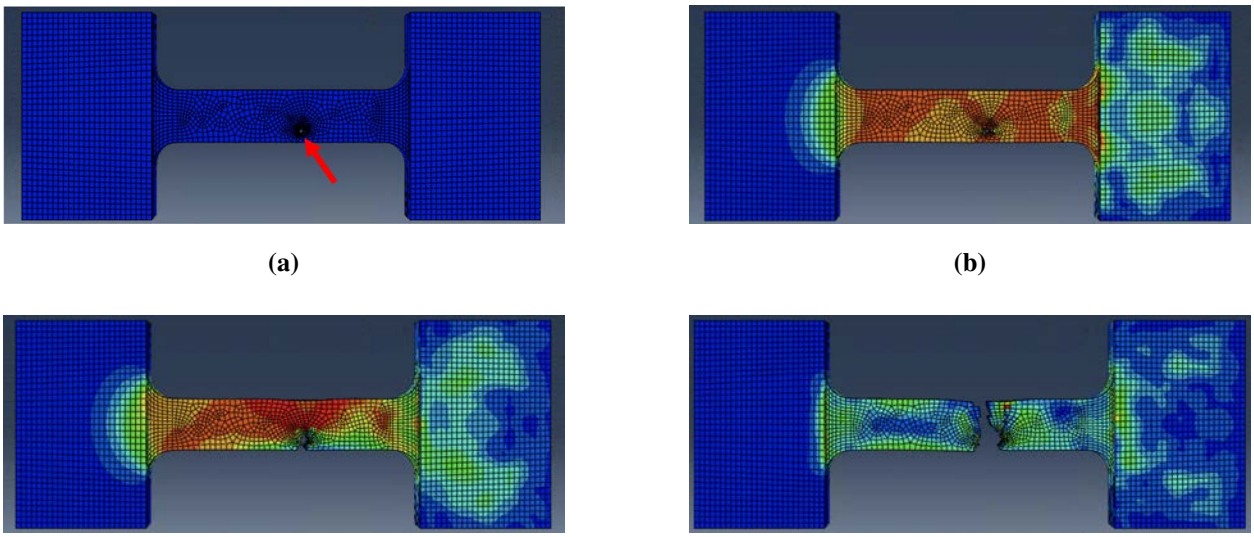

(a) **(b)**

(c) **(d)**

Figure 4.12: Results of simulated tensile testing with a pore (a) prior to testing, (b) prior to fracture, (c) initiation of fracture, and (d) complete fracture.

The resultant stress-strain curves are given in Figure 4.13 with relevant results summarized in Table 4.5. The reported literature values are experimental results from tensile testing on hot rolled and annealed Ti64 by Zhou et al. The model of the ideal, defect-free specimen demonstrated a higher ultimate tensile strength (UTS) and lower elongation than the literature-reported value. However, the annealed samples from cited literature are expected to have a slightly decreased strength and increased ductility. The yield strength, UTS and elongation in the sample modeled with a pore are all lower compared to those from the sample modeled with no defects and the literature. This is expected because a local stress concentration is generated at the pore (Figure 4.12c).

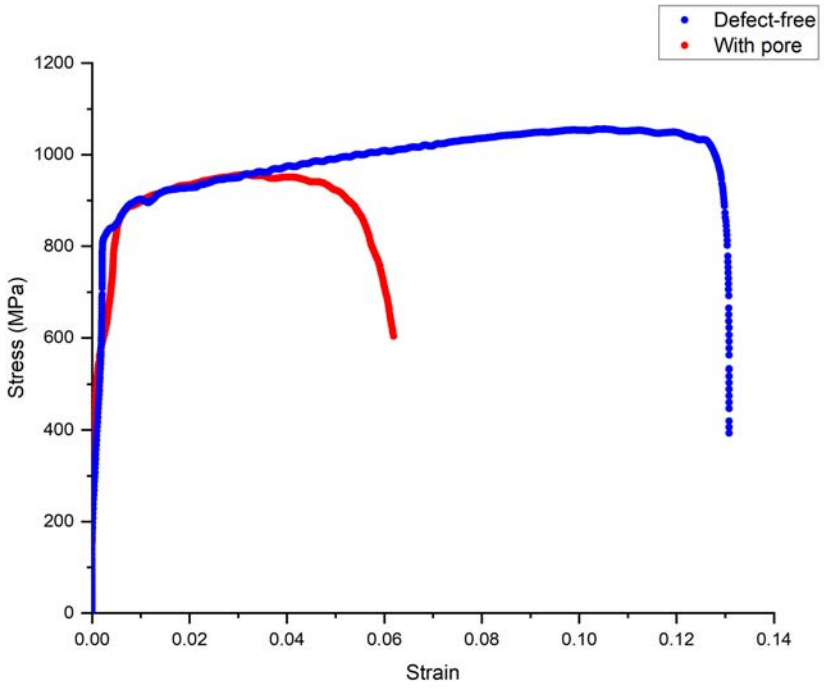

Figure 4.13: Stress-strain curves of modeled tensile tests on ideal sample (blue) and sample with a pore (red).

Table 4.5: Results from modeled FEM tests with and without a defect.

Property	No Defect	With Pore	Zhou et al. [57]
0.2% Yield Strength (MPa)	848	797	955
UTS (MPa)	1053	969	955
Elongation	0.13	0.06	0.15

It is demonstrated that the model is sufficient for comparison purposes before experimental verification. Further variations can be modeled based on the present work to compare and predict the mechanical behavior of recycled materials.

4.2 Conversion of Chips to Powder

Due to the high value of Ti64, it is important to have a variety of feedstock morphologies depending on the desired application of the material. For example, AM has strict requirements of spherical particles within a narrow size range such as 50-150 μm for laser-engineered net shaping (LENS) [84], a specific type of DED. A direct and more sustainable approach was taken to making powder feedstock suitable for a variety of purposes using recycled Ti64 scrap. Ti64 chips were cleaned with acetone then ball milled with either toluene or stearic acid as process control agents (PCAs). The vials with chips and stearic acid were backflowed with argon to prevent oxygen pickup during milling. Samples were taken from jars incrementally for analysis. The length of milling time, type of PCA and amount of PCA were explored.

Stearic acid and toluene were both separately used for this experiment. Stearic acid was added to the jars at 0, 0.5, 1, 2, 3, and 4% of the weight of the chips and the toluene was added to fill the jars to 50% of the jar height to maximize milling efficiency [85]. The milling conditions were the same as those used for feedstock of the sintered Ti64 samples: 10:1 BPR, 500 RPM and a 5 minutes on/5minutes off duty cycle as also used by Soufiani et al [86]. A summary of the extracted samples is given in Table 4.6. The samples that used stearic acid as a PCA are characterized by an experiment number that corresponds to the amount of stearic acid present in the jar, as well as a two digit number that tells the total time the sample had been milled for. For example, Expt3-20 corresponds to the sample obtained from Experiment 3 that used 1 wt-% stearic acid and was milled for 20 hours. For brevity, each sample ID is not listed in Table 4.6. The samples milled in toluene are identified first by the PCA and then a number corresponding to the amount of time that sample had been milled for.

Table 4.6: Sample summary for Ti64 samples extracted during ball milling in an effort to convert recycled chips to powder.

Sample ID	PCA	Amount of PCA	Time Milled (hr)
Expt1-40	Stearic acid	0 wt-%	40
Expt2-40	Stearic acid	0.5 wt-%	40
Expt3-40	Stearic acid	1 wt-%	40
Expt4-40	Stearic acid	2 wt-%	40
Expt5-50	Stearic acid	3 wt-%	40
Expt6-90	Stearic acid	4 wt-%	40
Toluene-20	Toluene	50 mL	20

4.2.1 Results of Ball Milling with Stearic Acid

Figure 4.14 shows SEM images that represent the morphology of ball milled particles with increased milling time and stearic acid, up to 4 wt-%. The box and whisker plots in Figure 4.15 show the particle size distributions for varying amounts of stearic acid up to 40 hours. The 0, 0.5 and 1 wt-% SA samples (Expt 1, 2, and 3, respectively) each had some cold welding observed after 10 hours of milling and the majority of the material had been cold welded at 20 hours, resulting in a rock-like morphology. Ball milling was continued up to 40 hours to observe if increased milling time would alleviate the cold welding. However, the amount of cold welding increased and resulted in a larger particle size and reduced amount of yield powder. Experiment 4 (2 wt-%) showed the largest change in particle morphology throughout the ball milling compared to Experiments 1-3 – the morphology started more flat and plate-like for the first 20 hours and became more rock-like at 30 hours with the onset of cold welding. The onset of cold welding in Experiment 4 can also be observed in Figure 4.15d where the average particle size is increased at 30 hours and the size distribution is more broad at 40 hours. Experiments 5 and 6 (3 and 4 wt-%, respectively) had the

least amount of cold welding compared to Experiments 1-4. However, the particle size reduction in Experiment 5 was less sufficient than prior experiments, particularly at 10 hours. Experiment 6 also showed less particle size reduction for the first 30 hours compared to prior experiments but no cold welding was observed throughout the entire 40 hours of milling. At 40 hours, the particles exhibited a notable decrease in size to an average of 26.47 ± 35.97 μm, from an average particle size of 576.47 ± 434.11 μm at 30 hours. The morphology of the particles in the first 30 hours of Experiment 6 were similar to the AR chips - long, thin and flat. At 40 hours, the smaller particles (<10 μm) were rock-like in morphology and the larger particles (>10 μm) were more flakey in morphology.

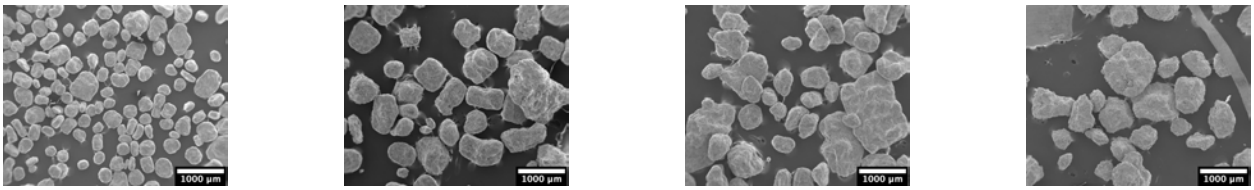

(a) Expt1-10 **(b)** Expt1-20 **(c)** Expt1-30 **(d)** Expt1-40

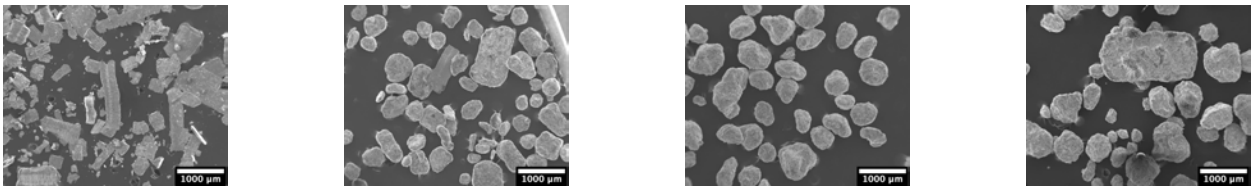

(e) Expt2-10 **(f)** Expt2-20 **(g)** Expt2-30 **(h)** Expt2-40

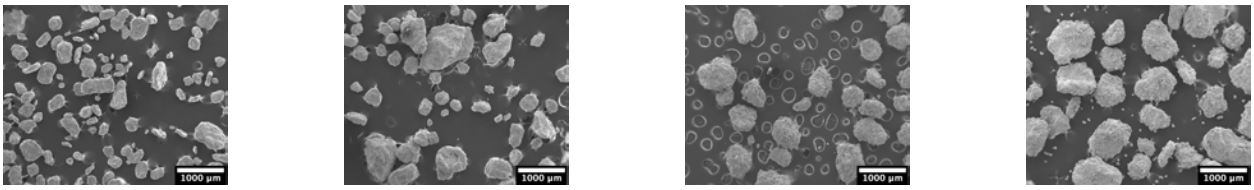

(i) Expt3-10 **(j)** Expt3-20 **(k)** Expt3-30 **(l)** Expt3-40

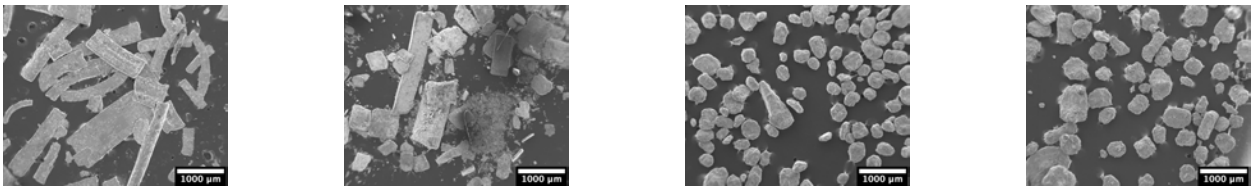

(m) Expt4-10 **(n)** Expt4-20 **(o)** Expt4-30 **(p)** Expt4-40

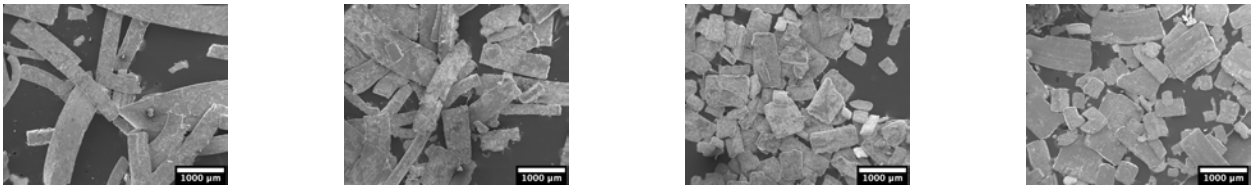

(q) Expt5-10 **(r)** Expt5-20 **(s)** Expt5-30 **(t)** Expt5-40

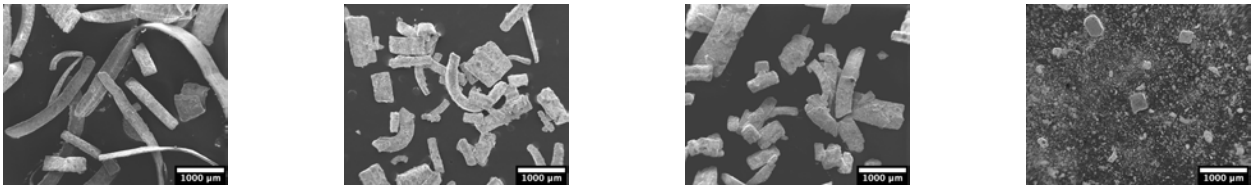

(u) Expt6-10 **(v)** Expt6-20 **(w)** Expt6-30 **(x)** Expt6-40

Figure 4.14: SEM images of ball milled Ti64 swarf with increasing milling time and amount of stearic acid.

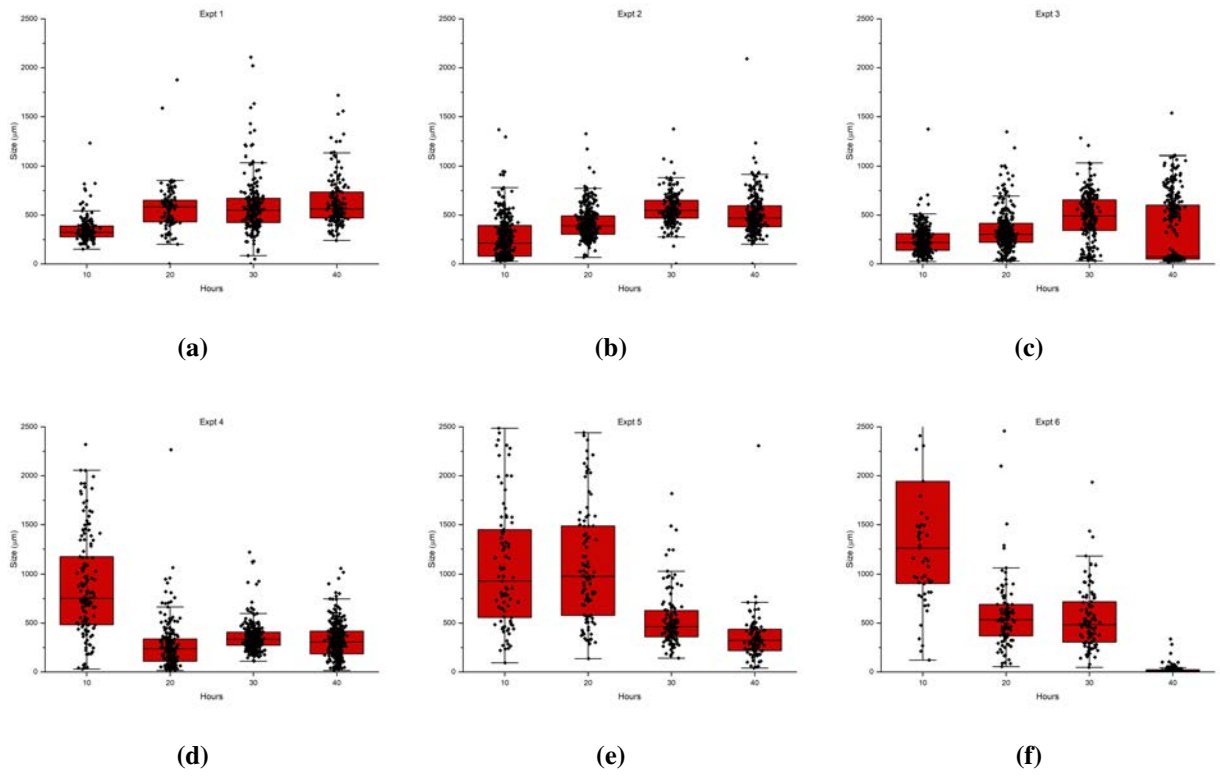

Figure 4.15: Box and whisker plots of measured particle sizes of ball milled Ti64 swarf using (a) 0 wt-%, (b) 0.5 wt-%, (c) 1 wt-%, (d) 2 wt-%, (e) 3 wt-%, and (f) 4 wt-% stearic acid. The bounds of the box give the upper and lower quartiles and the middle line shows the median value. Whiskers are drawn using a 1.5 IQR value. The upper bound of the whisker on E6-10 extends to 3252.18 µm.

4.2.2 Results of Ball Milling with Toluene

Compared to stearic acid, toluene proved to be a more effective PCA for reducing cold welding and particle size. Representative SEM images of Ti64 scrap milled for 0.5, 2, 10, and 20 hours are shown in Figure 4.16. The particle breakdown was more efficient than stearic acid, requiring only 20 hours to achieve the same particle size reduction as 40 hours when stearic acid was used. In addition, no cold welding was observed leading to a higher amount of yield material with less milling time. The particle breakdown was also more consistent than with stearic acid. While there were outliers of larger chips that did not break down, a more narrow size distribution was achieved compared to when stearic acid was used, particularly with the 10 and 20 hour samples.

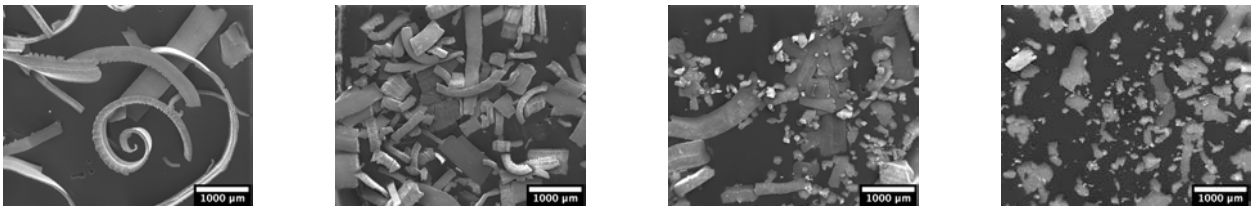

(a) **(b)** **(c)** **(d)**

Figure 4.16: SEM images of Ti64 swarf ball milled in toluene for (a) 0.5 hours, (b) 2 hours, (c) 10 hours, and (d) 20 hours.

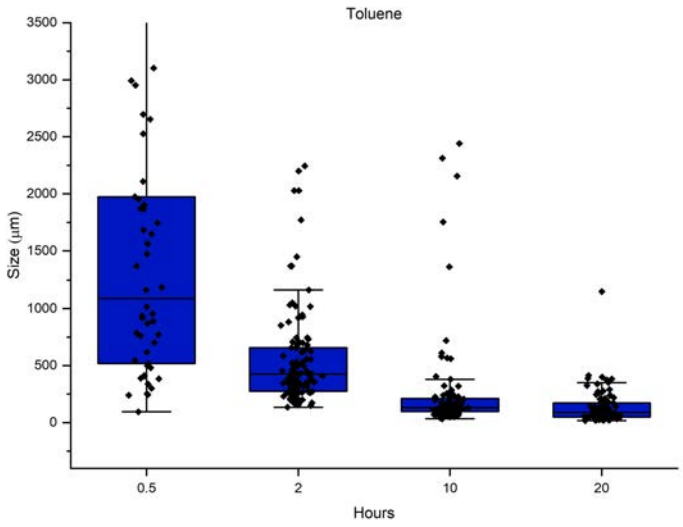

Figure 4.17: Box and whisker plot of measured particle sizes of ball milled Ti64 swarf using toluene as a PCA. The upper bound of the 0.5 hour whisker extends to 3561 µm.

Soufiani et al. ball milled Ti64 swarf with a similar morphology for a total of 50 hours using the same milling conditions as the presented work [86]. After only 10 hours of ball milling, the reported particles were already rock-like in morphology and the desired particle size range of 50 µm particles was achieved at 50 hours. The use of a PCA and presence of cold welding were not discussed. Machio et al. ball milled Ti-30Mg for up to 8 hours with a planetary ball mill comparing 0, 2, 4 and 6 wt-% stearic acid as a PCA [87]. It was found that the particle size decreased continuously with increasing amounts of stearic acid until 6 wt-%, where the particles

agglomerated and increased in size. The particle size distributions curves were also narrower compared to the reported work, and the average particle sizes was in the tens of microns [87]. It was reported that increasing the stearic acid also increased the yield powder [87]. Shial et al. and Alam et al. both ball milled Ti64 swarf in toluene [15]. After 0.5 hours of milling, the particle size was about 50 μm and decreased to around 20 μm after 2.5 hours of milling, with particles exhibiting a rock-like morphology.

4.2.3 Ball Milling Summary

The presented work did not achieve what these studies have reported, probably due to the different size and morphologies of the starting swarf. Nevertheless, effective particle breakdown was reached using a longer milling time than the cited works. The size of the particles obtained was either in the hundreds of microns range or tens of microns range and the particle morphologies were rock-like or flakey. This was dependent on the particle size, type of PCA and amount of PCA used. The chips milled with less stearic acid displayed a greater ability to break down compared to those milled with <3 wt-% stearic acid, and the morphology was rock-like. As the amount of stearic acid was increased to 3 and 4 wt-%, the particles became more flakey, especially larger particles, and the number of rock-like particle agglomerations was reduced. The particles milled in toluene showed a flat, flakey morphology regardless of the particle size.

4.3 Environmental Assessment - Energy Consumption

Using the same method as described in Chapter 3, the energy consumption to consolidate Ti64 swarf via SPS was calculated by integrating the power over the time. The plots for Ti64-950 and Ti64-1250 are shown in Figure 4.18. The larger fluctuations in the power curve of Ti64-950 during the heating process, compared to the steadier power output of Ti64-1250, was attributed to the different devices used to measure the temperature during SPS. For Ti64-950, a K-type thermocouple was used, which provided more frequent actual temperature feedback to compare with the programmed temperature, and thus led to more frequent adjustment (i.e., increase or decrease)

of the electrical current input. In contrast, the temperature was monitored by a pyrometer for the Ti64-1250 sample during SPS, which only led to small fluctuations in the difference between the measured temperature and programmed temperature. As a result, the electrical current was not significantly adjusted during the heating for Ti64-1250. The SEC to SPS the Ti64-950 and Ti64-1250 samples (6 g each) is 129.17 kWh/kg and 270.34 kWh/kg, respectively. At first glance, the two SEC values appear high. However, it is important to note that the relatively high SEC values for these two types of sample were due to the lab scale sampling, i.e., the input of the material was only $\sim$ 6 g. Further analysis provided in the next paragraph showed that the SEC of SPS was significantly reduced when the sample size was scaled up. In addition, the energy consumption of SPS does not increase linearly with increasing mass of samples.

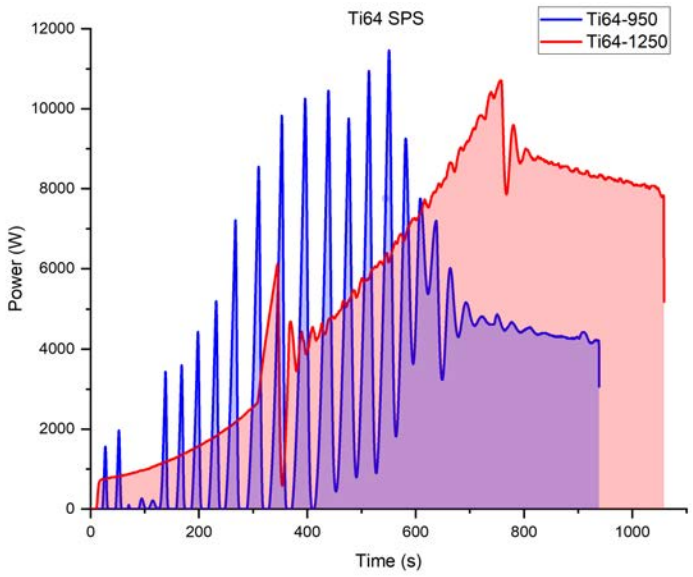

Figure 4.18: Power consumption for Ti64-950 (blue) and Ti64-1250 (red) SPS processes.

Similar to ball milling, using SPS at the laboratory scale is not energy efficient. Table 4.7 provides the energy consumption to SPS a 6 g, 10 g, 25 g and 452 g sample to 775°C.

Table 4.7: SEC for scaled-up SPS, up to 775°C.

Sample Mass (g)	Total Energy (kWh)	SEC (kWh/kg)
6	0.32	53.37
10	0.34	34.81
25	0.35	16.92
452	2.45	5.42

Comparing to industry methods such as melting and casting or HIP, which consume 6.52 kWh/kg [77] and 5.5-9.1 kWh/kg [88], respectively, the SEC to SPS smaller samples (<25 g) is high. However, the amount of mass being used for SPS affects the SEC considerably. Table 4.7 indicates that an increased total energy consumption is not linearly proportional to the increased mass, and that a drastic decrease in SEC is observed as mass increases, particularly with the 452 g sample. While Table 4.7 gives the energy consumption to SPS only to 775°C, it demonstrates that by scaling up the amount of material being sintered, the SEC is comparable to current industry methods and more energy efficient than additive manufacturing which can consume 22-2,222 kWh/kg [44].

In addition to measuring the total energy consumption to SPS bulk samples, relative density curves (Figure 4.19) were made to compare the energy consumed to consolidate swarf or GA powder to 95% relative density.

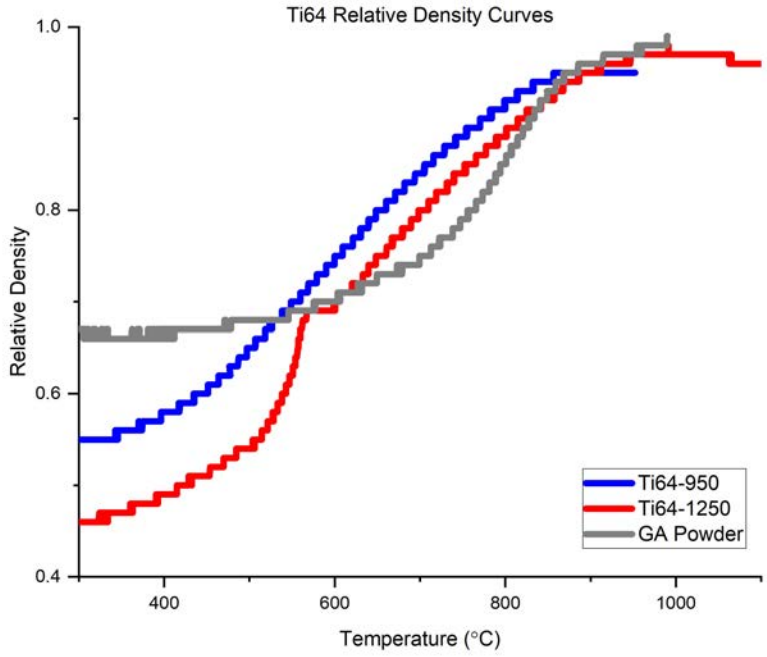

Figure 4.19: Relative density curves for Ti64-950 (blue), Ti64-1250 (red) and GA powder (grey).

A high green packing density was difficult to obtain given the spring-like behavior of the chips. Therefore, the initial density of Ti64-950 and Ti64-1250 are lower than that for the GA powder in Figure 4.19. A sudden increase in density for Ti64-1250 near 600°C was observed as a result of the decreased yield strength with increased temperature and the rearranging of chips. A notable decrease in yield strength of Ti64 at 600°C has also been reported by prior research [89]. The power consumption for samples to reach full density was determined based on the temperature and time that each sample reached 95% relative density. The results are tabulated in Table 4.8.

Table 4.8: Temperature, time and energy consumed to reach 95% relative density.

Sample ID	Temperature (°C)	Time (s)	Energy consumed (kWh)
GA powder	868.2	535.1	76.92
Ti64-950	856.4	585.1	61.43
Ti64-1250	885.7	547.4	71.36

The energy input required to reach full density by using SPS for Ti64 machining swarf is less than that of using GA powder, indicating that using swarf as an SPS feedstock decreases the energy consumption compared to using GA powder. In addition, the direct recycling of chips avoids the extraction and production processes of virgin titanium using the Kroll's process, which has been estimated to consume 71.61 kWh/kg [90] simply to produce the Ti sponge and 190.7 kWh/kg for the entire primary production process [9]. The primary benefit of using GA powder is the spherical morphology and higher purity. However, not all applications of Ti64 require the mechanical properties associated with virgin Ti64 (enhanced ductility, higher UTS). Therefore, direct recycling using SPS is a more energy-efficient method compared to virgin material production.

Ball milling 6 g of material at a time is not a time-effective solution for energy-efficient recycling of Ti64 in industry. Therefore, a scaled-up process with an energy evaluation must be considered. Table 4.9 outlines the data necessary to assess the SEC of a scaled-up recycling operation, assuming either the small (100 mL/jar capacity) or large (1000 mL/jar capacity) ball mills that are available in the laboratory are used with the same milling parameters as presented in this work. Filling the volume of the jars 50%, each of the four jars can accommodate a certain amount of Ti64 swarf. To process 1 kilogram of material, the mills must be run for multiple 15-minute operations depending on the jar capacity ("total operations for 1 kg"). The measured power draw on the small ball was approximately 50% of the maximum power requirement. Therefore, an overestimation of 80% of the maximum power draw was used for the large ball mill. Applying

this methodology, ball milling 1 kg for 40 hours to obtain a powder consumes 267 kWh/kg and 352 kWh/kg for the small and large ball mills, respectively. While these values are higher than the SEC to atomize Ti64 powder from virgin feedstock (7.02-31.7 MJ/kg (1.95-8.81 kWh/kg) [44]) the laboratory-sized ball mills will generally have a higher SEC because of the lower material capacity compared to industry-sized mills.

Table 4.9: Energy parameters to scale up ball milling operations.

Parameter	Small Ball Mill	Large Ball Mill
Number of jars	4	4
Capacity per jar (kg)	0.006	0.06
Total operations for 1 kg	42	5
Energy to mill for 1 hour (kWh)	0.159	1.76
SEC to mill 1 kg (kWh/kg)	6.68	8.8

Similar to SPS, the increased energy consumption is not linearly proportional to the increased mass. Therefore, it is predicted that further scale-up of ball milling operations will further reduce the SEC to be comparable to using GA.

4.4 Miscellaneous Work

AR Ti64 chips were also ball milled using alumina media to identify if alumina would be more efficient in particle reduction compared to stainless steel. In addition, it was reported that Al_2O_3 could be a reinforcement phase to make an Al_2O_3-Ti64 composite for improved mechanical properties [91]. Hence, if there is any contamination of the chips from the Al_2O_3 balls and jar, no detrimental effect would be expected. The samples milled with alumina media are referred to as Ti64-alumina-950 and Ti64-alumina-1250 following the same convention as the Ti64-950 and

Ti64-1250 samples, with the addition of specifying the alumina milling media. The XRD patterns of the AR chips, chips milled in alumina media and subsequently sintered are shown in Figure 4.20. The alumina balls used for milling are more brittle and fracture occurs more easily than the stainless steel, therefore it was expected that alumina show up on the XRD patterns. However, no significant alumina peaks are detected, indicating that there is not a significant amount of alumina present on the chips from ball milling. Additionally, no alumina peaks were observed in the sintered samples.

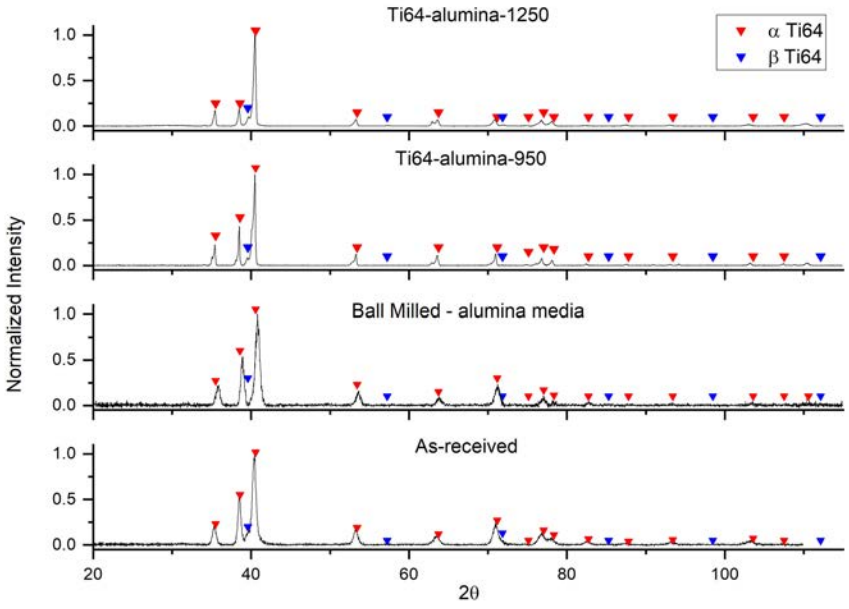

Figure 4.20: XRD plots, from the bottom upwards, of the AR Ti64 chips, chips milled with alumina media, chips SPS'ed to 950°C and chips SPS'ed to 1250°C.

The Archimedes densities achieved for the samples milled with alumina media and sintered to 950°C and 1250°C were 4.25 (95.84%) and 4.28 (96.61%) g/cm^3, respectively. The milling media is observed to have no effect on the density. Figure 4.21 shows the microstructure of Ti64-alumina-1250. The microstructure was also observed throughout the Ti64-alumina-950 sample. However, the lower sintering temperature with the alumina inclusions led to a high porosity in the Ti64-alumina-950 sample. Therefore, the processing parameters for this sample were excluded

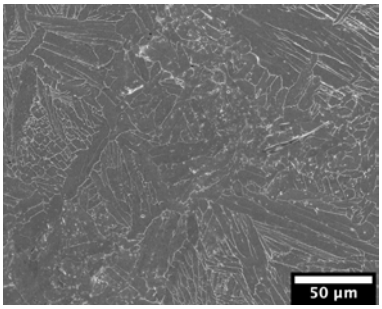

Figure 4.21: Microstructure of Ti64-alumina-1250 sample.

for further investigation. The grain and colony sizes were also found to be independent of milling media.

Figure 4.22 shows the EDS map results from a cross-section of the Ti64-alumina-1250 sample. The results are similar to the Ti64-1250 sample and it is determined that milling media again does not play a role in the compositional inhomogeneity that is observed.

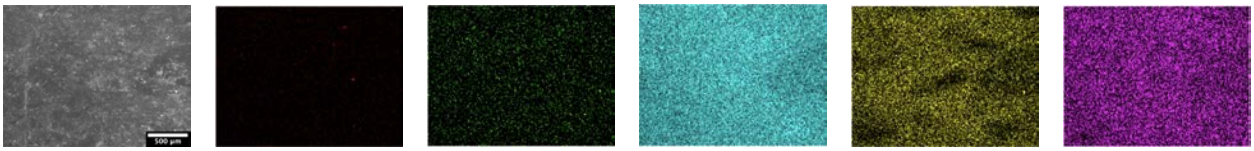

(a) SEM **(b)** C **(c)** O **(d)** Ti **(e)** Al **(f)** V

Figure 4.22: EDS results with (a) SEM image, (b) C, (c) O, (d) Ti, (e) Al, and (f) V elemental maps from a cross-section of Ti64-alumina-1250.

Similar to the Ti64-950 sample, the Ti64-alumina-950 sample showed a few small regions consisting of the globular α phase as shown in Figure 4.23.

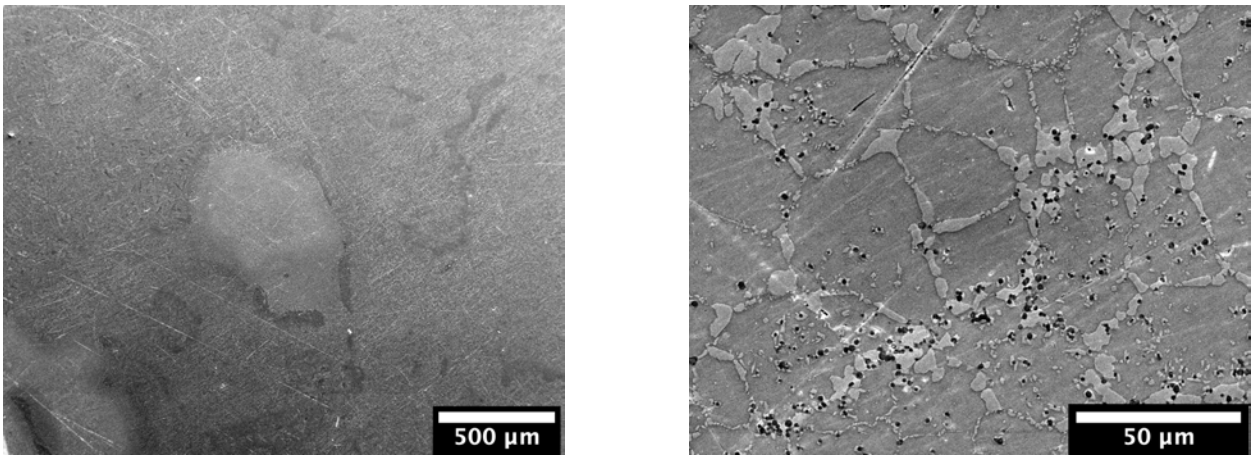

(a) **(b)**

Figure 4.23: (a) Overview and (b) magnified image showing region consisting of equiaxed grains observed on the Ti64-alumina-950 sample.

Ti64-alumina-950 requires a 9.2% higher power consumption compared to Ti64-950, but Ti64-alumina-1250 required only 6.67% more energy compared to the Ti64-1250 sample. This shows that the milling media makes a negligible difference in the amount of power consumed. In summary, the alumina milling media was not observed to make a difference in phase constitution, grain size or energy consumption.

4.5 Summary

Ti64 machining swarf was successfully densified to bulk samples via SPS and reduced to a powder feedstock via ball milling, providing two sustainable recycling routes. It is demonstrated that only minimal particle reduction of the swarf is required prior to SPS to achieve a high packing density, and near-full density is achieved from SPS without the use of a sintering aid such as GA power. The bulk samples made from SPS of machining swarf exhibited a higher hardness than annealed Ti64, and similar hardness to work-hardened Ti64. This was attributed to the work-hardening of the chips during machining operations and lack of grain growth in SPS. Lack of ductility remains a primary concern in the sintered bulk materials due to residual porosity, which

can be improved by optimizing the SPS parameters including increased pressure or temperature. It is shown that increasing sample size has a notable effect on decreasing the SEC for SPS and that the SEC to SPS swarf is comparable to that of GA powder.

Particle size reduction of Ti64 swarf was effective using both stearic acid and toluene, however toluene is demonstrated to be more efficient than stearic acid. Compared to production and atomization of virgin powder, ball milling is more energy-efficient and a variety of powder feedstock morphologies is obtained with different amounts of either stearic acid or toluene and milling time.

Chapter 5

Conclusions and Suggestions Future Work

In general, extracting virgin metals from natural resources exerts a significant environmental and economic impact on our earth and society. Production of virgin stainless steels and titanium (Ti) alloys have particularly caused concerns because of the high demands of these two classes of metals across many industries. Currently, less than one-third of steel scrap and one-fourth of Ti scrap are recirculated back into supply. In addition, the traditional recycling methods require multiple steps and significant energy consumption, especially for Ti and its alloys. To reduce the cost of materials and the environmental impact, the present work investigated the effectiveness of direct reuse of stainless steel swarf and Ti64 swarf as feedstock for spark plasma sintering (SPS) to make solid bulk samples. Mechanical properties, e.g., hardness, of the materials made from the swarf were comparable to, if not better than, their virgin counterparts. Ball milling was also used as an approach to obtain varying feedstocks.

5.1 SPS of Waste Chips

Overall, the direct reuse of swarf as feedstock for SPS is proved to be a successful method to recycle stainless steels and Ti alloys, with an SEC lower than conventional recycling methods (such as remelting and purification for casting), or producing virgin materials. Full density was achieved on all Ti64 samples and the 304L stainless steel samples reached near full density. The size and morphology of swarf chips play a crucial role in densification. The thicker 304L chips resulted in a lower density compared to the thinner Ti64 chips, which had a higher surface area to volume ratio, and a larger curvature. As a result, the green packing density of the 304L chips was lower than that of Ti64 swarf. The ductile nature of the Ti alloy also facilitated a better green body packing density than the 304L stainless steel when the chips were cold pressed. The addition of the gas atomized (GA) powder significantly reduced the size of pores compared to the counterpart where the feedstock was 100% swarf. However, pores were more frequently dispersed due to the

lack of full densification in the powder pocket regions surrounding the individual chip surfaces. Although the overall relative density and mechanical properties of the sintered bulk samples were not improved by adding GA powder, addition of GA powder improved the packing density of the green body. Increasing the sintering temperature or pressure can enhance densification and mitigate the porosity.

In both Ti64 and 304L stainless steel, elemental segregation and precipitation (carbides or oxides) were observed. The 304L samples exhibited chromium carbide precipitates, which is a common phenomenon in stainless steels that affects corrosion properties and local mechanical properties. Areas rich in chromium carbides resulted in higher hardness compared to the surrounding regions. The aluminum-depletion in Ti64, resulting from the diffusion of aluminum towards the surface oxide layers, can be controlled by raising the peak sintering temperature. EDS mapping results support that the depletion zones became more uniformly spread throughout the bulk with the increase in temperature from 950°C to 1250°C. The aluminum depleted zones resulted in higher hardness compared to the surrounding areas.

The energy consumption associated with the SPS of Ti64 swarf was less than that of producing virgin materials, if the processes are scaled up. In general, the energy consumption is proportional to the carbon footprint. Therefore, the carbon footprint of the present recycling method is also reduced by using SPS with swarf instead of virgin material. To reach full density, the 6 g samples consumed 76.97 kWh, 61.43 kWh, and 71.36 kWh for GA powder, Ti64-950 and Ti64-1250, respectively, demonstrating that the energy consumption to densify swarf is comparable to that to densify GA powder. However, in order to homogenize the microstructure and composition for more consistent mechanical properties of the bulk material, the full sintering process is required. To fully sinter the swarf via SPS, a 10 g and 6 g sample used 0.86 kWh (86.06 kWh/kg) and 0.78 kWh (129.17 kWh/kg), respectively, for Ti64-950 and 1.58 kWh (158.07 kWh/kg) and 1.62 kWh (270.34 kWh/kg) for Ti64-1250, respectively. This demonstrates that there is not a linear correlation between the amount of material to be sintered and the energy consumption. In other words, if a 100 g of Ti64 sample was sintered using swarf, the energy consumption of SPS would

not be ten times that used for a 10 g sample. Compared to current production of virgin material and AMb, the SPS is more energy efficient.

The biggest limiting factor in comparing the SEC of direct reuse/recycling of swarf via SPS to other conventional recycling methods is the ability of the SPS to be scaled up to accommodate larger quantities of material. By using scaled-up SPS machines that have a capacity more comparable to industry scale, the SEC is predicted to be lower than that of melting and remelting that is required for Ti and its alloys in conventional recycling routes. The swarf also does not need to be mixed with any amount of virgin material. Therefore, by scaling up the SPS and eliminating the need for virgin material, the present method of direct recycling via SPS is more energy efficient. In addition, with only 22% of Ti64 scrap in circulation and nearly 90% of the Ti64 used for industry components becoming scrap, the SPS offers a simpler and faster method for recycling.

5.2 Ball Milling of Waste Ti64 Chips

In addition, Ti64 swarf was successfully converted to powder by planetary ball milling in the present work. Both stearic acid and toluene proved to be useful PCAs, but toluene is more effective and efficient in consistently reducing particle size and preventing cold welding than stearic acid. It was determined that at least 4 wt-% stearic acid is necessary to have an effective particle size reduction within 40 hours of milling while also preventing cold welding. The chips milled in toluene for 20 hours achieved nearly the same particle size distribution as those milled in 4 wt-% stearic acid for 40 hours. The resultant powders in the present research have not achieved the spherical morphology desired for applications such as AM. However, the investigation into the PCA selection and ball milling time provides insights into how to convert Ti64 swarf to powders with different particle sizes and varied shapes for versatility. It is worth noting that SPS has the capability to accommodate various feedstock, in contrast to the specific requirements of powders in AM techniques. In addition, the energy required to sinter the non-spherical powders converted from swarf is lower than that of GA powder because of the flaky morphology of the ball milled powder.

5.3 Suggestions for Future Work

The present work provides a working foundation for two energy-efficient methods to recycle metal swarf. Improvements to these methods are suggested to obtain higher quality materials that can be used for industry applications. This section outlines proposals to refine each of the two recycling methods and potential applications of the ball milled feedstock.

5.3.1 Optimizing the SPS Process

Modifications to the SPS parameters are suggested to improve the densification of thicker chips like the nibbled 304L chips. To sustain the motivation of this work, the energy consumption needs to stay under consideration. Increasing the peak temperature or hold time during sintering was shown to result in a higher density and more homogeneous microstructure, but also increased the total energy consumption. However, pressure can also be used to facilitate mass diffusion. The Gibbs free energy is linearly proportional to pressure [71]. Therefore, increasing pressure leads to a higher driving force for diffusion, facilitating pore closure and compositional homogenization while not increasing the energy consumption. Complete closure of pores is not possible at elevated temperatures but reducing the pore size would aid in improved mechanical properties as demonstrated with the hardness testing results of 304L stainless steel.

It is recommended that the ratio of GA powder to swarf is studied more in-depth to assess the minimum amount of powder necessary to aid in achieving a full density when using thicker chips for SPS. Micro X-ray CT scanning is proposed to obtain a more accurate characterization of pore sizes and their distributions throughout the bulk of samples, which will subsequently help simulate and predict macroscopic mechanical behavior. However, the tradeoff between mechanical properties and environmental impact should remain under consideration and a minimal amount of virgin material used in order to minimize the embodied energy.

Macroscopic mechanical characterization methods like tensile testing are also recommended on both the 304L and Ti64 samples to better assess the impacts of adding GA powder or modifying the sintering parameters. The Vickers and nanoindentation data proved useful for observing local

mechanical properties, but they need to be analyzed at the macro-level to thoroughly assess the applicability of this recycling method for industry applications. Further work is also proposed to modify the Ti64 FEM tensile testing model to predict the material behavior of specimens that have additional defects, such as varying pore size, pore frequency and compositional inhomogeneity, prior to verifying the results experimentally.

5.3.2 Consolidation of Ball Milled Swarf

Sintering the flaky powder particles that were obtained from ball milling is recommended to analyze the effects of ball milling on densification, compositional variance, and mechanical properties. Sintering flaky powders is predicted to be more energy-efficient compared to a spherical or rock-like feedstock morphology based on the relative density curves shown in this work, and particles with a flaky morphology have been shown to achieve a higher densification and higher micro-hardness compared to feedstock with spherical or plate-like morphologies [92]. This indicates that the chips that were ball milled to powder in toluene, which achieved a flaky morphology, can be SPS'ed at a lower temperature than the GA powder to reach the same density, therefore consuming less energy. If ball milled powders are sintered with SPS, the hardness is expected to be improved compared to virgin materials due to the grain refinement.

The compositional variance in both 304L and Ti64 can be reduced by sintering the ball milled swarf. Reducing the particle size to the micron scale will result in smaller but more frequently dispersed aluminum depleted regions in the Ti64 and chromium-carbides in 304L. Therefore, further work is proposed to find the maximum particle size that best homogenizes the composition.

A procedure for evaluating the energy consumption of a scaled-up SPS process should be developed and standardized to have a more concrete assessment of the environmental impact SPS has compared to current industry methods. The present work demonstrated with Ti64 that there was not a linear correlation between energy consumption and the amount of material sintered. However, the relatively small capacity of the laboratory-scale SPS is not sufficient for industry use, even with modified tooling.

5.3.3 Additive Manufacturing

One of the many benefits of AM is that complex parts can be produced in a short time and with fewer machining steps compared to conventional methods. LENS uses a continuous deposition of either wire or powder feedstock material directly into a melt pool (Figure 5.1). Compared to other AM methods, DED offers a high degree of control in grain structure, high quality parts and has the least amount of waste feedstock material compared to other methods such as powder bed fusion [93].

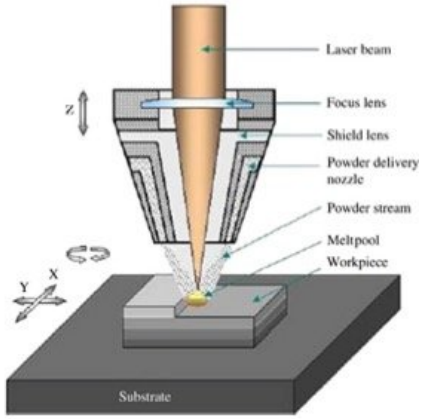

Figure 5.1: Diagram of LENS machine [94].

The powder feedstock for LENS must be spherical with a particle size of 50-150 µm in diameter [84]. The primary challenge with using titanium swarf for DED is obtaining the spherical shape. The ball milled Ti64 swarf did not achieve the morphology required for LENS, therefore further work is proposed to modify the ball milling parameters so that particles can be used for DED. Cryomilling may be a useful alternative milling method, as the cold environment prevents cold welding and facilitates particle fracture. However, titanium has a high affinity to nitrogen and if LN_2 is used as the milling environment, it is possible that titanium nitrides may form and embrittle the resultant feedstock. This may be beneficial to other mechanical properties such as hardness. Kundu et al. created a powder mixture consisting of Ti64 + TiN that was used for a type of powder bed fusion AM. They observed that increasing the amount of TiN increased the hardness

significantly compared to pure Ti64 [95]. Therefore, it is suggested that a metal-matrix composite powder can be formed by cryomilling the Ti64 swarf, subsequently improving the mechanical properties of parts created using AM methods and reducing the need for virgin materials.

5.4 Summary

In conclusion, my research proved that reuse of austenitic stainless steel chips and Ti64 alloy swarf as feedstock for SPS is an effective and energy efficient approach to recycle metal scraps, compared to production and use of virgin GA powders, or conventional metal recycling routes. The mechanical performance of the samples made from metal swarf outperformed the relevant industrial standard materials in terms of hardness while the ductility remains a concern due to the presence of pores. Therefore, future work is proposed to continue to address the challenges associated with mechanical performance, including but not limited to, tuning the SPS processing parameters, quantifying an appropriate amount of added powder as a sintering aid, and refining the morphology of the swarf by ball milling. It is critical for the health of our planet to always consider the tradeoff between energy consumption and materials performance.

References

[1] George Krauss. Steels: processing, structure, and performance. ASM International, Materials Park, Ohio, second edition edition, 2015. OCLC: ocn904652440.

[2] Krishnan K. Sankaran and Rajiv S. Mishra. Titanium Alloys. In Metallurgy and Design of Alloys with Hierarchical Microstructures, pages 177–288. Elsevier, 2017.

[3] R.S. Kaplan and H Ness. Recycling of metals. Conservation & Recycling, 10(1):1–13, 1987.

[4] S. Ramachandra Rao. Resource Recovery and Recycling from Metallurgical Wastes, volume 7 of Waste Management Series. Elsevier, 1st edition, 2006.

[5] Jeremiah Johnson, B.K. Reck, T. Wang, and T.E. Graedel. The energy benefit of stainless steel recycling. Energy Policy, 36(1):181–192, January 2008.

[6] Mohan Yellishetty, Gavin M. Mudd, P.G. Ranjith, and A. Tharumarajah. Environmental life-cycle comparisons of steel production and recycling: sustainability issues, problems and prospects. Environmental Science & Policy, 14(6):650–663, October 2011.

[7] Dimos Paraskevas, Kim Vanmeensel, Jef Vleugels, Wim Dewulf, and Joost R. Duflou. The Use of Spark Plasma Sintering to Fabricate a Two-phase Material from Blended Aluminium Alloy Scrap and Gas Atomized Powder. Procedia CIRP, 26:455–460, January 2015.

[8] Osamu Takeda and Toru H. Okabe. Chapter 16 - Recycling of Ti. In Zhigang Zak Fang, Francis H. Froes, and Ying Zhang, editors, Extractive Metallurgy of Titanium, pages 363–387. Elsevier, January 2020.

[9] Granta EduPack software, Granta Design Limited, 2019.

[10] C. Suryanarayana. Mechanical alloying and milling. Progress in Materials Science, 46(1):1–184, January 2001.

[11] Thomas H. Courtney. Mechanical behavior of materials. Waveland Press, Long Grove, Illinois, 2. ed edition, 2005.

[12] D.B. Witkin and E.J. Lavernia. Synthesis and mechanical behavior of nanostructured materials via cryomilling. Progress in Materials Science, 51(1):1–60, January 2006.

[13] Claudiney de Sales Pereira Mendonça, Vander Alkmin dos Santos Ribeiro, Mateus Morais Junqueira, Daniela Sachs, Leonardo Albergaria Oliveira, Mírian de Lourdes Noronha Motta Melo, and Gilbert Silva. Recycling Chips of Stainless Steel by High Energy Ball Milling. Materials Science Forum, 930:454–459, September 2018.

[14] M. H. Enayati, M. R. Bafandeh, and S. Nosohian. Ball milling of stainless steel scrap chips to produce nanocrystalline powder. Journal of Materials Science, 42(8):2844–2848, April 2007.

[15] S. R. Shial, M. Masanta, and D. Chaira. Recycling of waste Ti machining chips by planetary milling: Generation of Ti powder and development of in situ TiC reinforced Ti-TiC composite powder mixture. Powder Technology, 329:232–240, April 2018.

[16] J. Corrochano, M. Lieblich, and J. Ibáñez. The effect of ball milling on the microstructure of powder metallurgy aluminium matrix composites reinforced with MoSi2 intermetallic particles. Composites Part A: Applied Science and Manufacturing, 42(9):1093–1099, September 2011.

[17] P. Kulecki and E. Lichańska. The Effect of Powder Ball Milling on the Microstructure and Mechanical Properties of Sintered Fe-Cr-Mo-Mn-(Cu) Steel. Powder Metallurgy Progress, 17(2):82–92, December 2017.

[18] Yan Long, Weihua Zhang, Liang Peng, Haiyan Peng, Xiaozhen Li, and Xiaolong Huang. Mechanical Behaviors of Ultrafine-Grained Ti-6Al-4V Alloy During Compression at Various Strain Rates. Metallurgical and Materials Transactions A, July 2020.

[19] Pei Sun, Z. Zak Fang, Yang Xia, Ying Zhang, and Chengshang Zhou. A novel method for production of spherical Ti-6Al-4V powder for additive manufacturing. Powder Technology, 301:331–335, November 2016.

[20] Ricardo H. R. Castro and Klaus van Benthem, editors. Sintering: mechanisms of convention nanodensification and field assisted processes. Number v. 35 in Engineering materials. Springer, Berlin ; New York, 2013. OCLC: ocn826652603.

[21] John E. Blendell and Wolfgang Rheinheimer. Solid-State Sintering. In Encyclopedia of Materials: Technical Ceramics and Glasses, pages 249–257. Elsevier, 2021.

[22] Suk-Joong L. Kang. Sintering - Densification, Grain Growth, and Microstructure. Butterworth-Heinemann, 1st edition, February 2005.

[23] Chung Van Nguyen, Sree Koundinya Sistla, Stanley Van Kempen, Ngoc Anh Giang, Alexander Bezold, Christoph Broeckmann, and Friederike Lange. A comparative study of different sintering models for Al_2O_3. Journal of the Ceramic Society of Japan, 124(4):301–312, 2016.

[24] Paul G. Shewmon. Diffusion in solids. Minerals, Metals & Materials Society, Warrendale, Pa, 2.ed edition, 1989. OCLC: 21197119.

[25] C. Velmurugan, V. Senthilkumar, Krishanu Biswas, and Surekha Yadav. Densification and microstructural evolution of spark plasma sintered NiTi shape memory alloy. Advanced Powder Technology, 29(10):2456–2462, October 2018.

[26] Ziwei Xu, Chengchang Jia, Chunjiang Kuang, Ke Chu, and Xuanhui Qu. Spark plasma sintering of nitrogen-containing nickel-free stainless steel powders and effect of sintering temperature. Journal of Alloys and Compounds, 484(1):924–928, September 2009.

[27] Dimos Paraskevas, Kim Vanmeensel, Jef Vleugels, Wim Dewulf, Yelin Deng, and Joost R. Duflou. Spark Plasma Sintering As a Solid-State Recycling Technique: The Case of Aluminum Alloy Scrap Consolidation. Materials, 7(8):5664–5687, August 2014.

[28] Clemens Nikolaus Cislo, Bernhard Kronthaler, Bruno Buchmayr, and Christian Weiß. Solid State Recycling of Aluminum Alloy Chips via Pulsed Electric Current Sintering. Journal of Manufacturing and Materials Processing, 4(1):23, March 2020.

[29] E. W. Lui, S. Palanisamy, M. S. Dargusch, and K. Xia. Effects of chip conditions on the solid state recycling of Ti-6Al-4V machining chips. Journal of Materials Processing Technology, 238:297–304, December 2016.

[30] P. Luo, H. Xie, M. Paladugu, S. Palanisamy, M. S. Dargusch, and K. Xia. Recycling of titanium machining chips by severe plastic deformation consolidation. Journal of Materials Science, 45(17):4606–4612, September 2010.

[31] Nicholas S. Weston and Martin Jackson. FAST-forge of Titanium Alloy Swarf: A Solid-State Closed-Loop Recycling Approach for Aerospace Machining Waste. Metals, 10(2):296, February 2020. Number: 2 Publisher: Multidisciplinary Digital Publishing Institute.

[32] Vojtěch Kučera, Filip Průša, and Dalibor Vojtěch. Al-Fe Chips Processed by High-Energy Ball Milling and Spark Plasma Sintering. Solid State Phenomena, 270:197–204, November 2017.

[33] Tomila M. Vidyuk, Dina V. Dudina, Michail A. Korchagin, Alexander I. Gavrilov, Tatiana S. Skripkina, Arina V. Ukhina, Alexander G. Anisimov, and Boris B. Bokhonov. Melting at the inter-particle contacts during Spark Plasma Sintering: Direct microstructural evidence and relation to particle morphology. Vacuum, 181:109566, November 2020.

[34] Christophe Collard, Zofia Trzaska, Lise Durand, Jean-Marc Chaix, and Jean-Philippe Monchoux. Theoretical and experimental investigations of local overheating at particle contacts in spark plasma sintering. Powder Technology, 321:458–470, November 2017.

[35] Alan M. Russell and Kok Loong Lee. Structure-Property Relations in Nonferrous Metals. John Wiley & Sons, Inc., 1st edition, May 2005.

[36] Blake Patrick Fullenwider. From Recycled Machining Waste to Useful Powders: Sustainable Fabrication and Utilization of Feedstock Powder for Metal Additive Manufacturing. PhD thesis, Colorado State University, Fort Collins, CO, 2018.

[37] Sulaymon Eshkabilov, Ismat Ara, Igor Sevostianov, Fardad Azarmi, and Xiangping Tangpong. Mechanical and thermal properties of stainless steel parts, manufactured by various technologies, in relation to their microstructure. International Journal of Engineering Science, 159:103398, February 2021.

[38] Babatunde Abiodun Obadele, Ramokone Marcia Mafafo, Walter Roberto Tuckart, and Peter Apata Olubambi. Fabrication of AISI 304 Austenitic Stainless Steels with TiN Addition Using Spark Plasma Sintering Method. In S. Vijayan, Nachiappan Subramanian, and K. Sankaranarayanasamy, editors, Trends in Manufacturing and Engineering Management, Lecture Notes in Mechanical Engineering, pages 681–689, Singapore, 2021. Springer.

[39] Si Young Chang, Sung-Tag Oh, Myung-Jin Suk, and Chan Seok Hong. Spark Plasma Sintering of Stainless Steel Powders Fabricated by High Energy Ball Milling. Journal of Korean Powder Metallurgy Institute, 21(2):97–101, April 2014.

[40] M. Qian, G. B. Schaffer, and C. J. Bettles. 13 - Sintering of titanium and its alloys. In Zhigang Zak Fang, editor, Sintering of Advanced Materials, Woodhead Publishing Series in Metals and Surface Engineering, pages 324–355. Woodhead Publishing, January 2010.

[41] Youngmoo Kim, Eun-Pyo Kim, Young-Beom Song, Sung Ho Lee, and Young-Sam Kwon. Microstructure and mechanical properties of hot isostatically pressed Ti–6Al–4V alloy. Journal of Alloys and Compounds, 603:207–212, August 2014.

[42] Pei Sun, Zhigang Zak Fang, Ying Zhang, and Yang Xia. Review of the Methods for Production of Spherical Ti and Ti Alloy Powder. JOM, 69(10):1853–1860, October 2017.

[43] José M. C. Azevedo, André CabreraSerrenho, and Julian M. Allwood. Energy and material efficiency of steel powder metallurgy. Powder Technology, 328:329–336, April 2018.

[44] Z.Y. Liu, C. Li, X.Y. Fang, and Y.B. Guo. Energy Consumption in Additive Manufacturing of Metal Parts. Procedia Manufacturing, 26:834–845, 2018.

[45] M. Sherif El-Eskandarany. Controlling the powder milling process. In Mechanical Alloying, pages 48–83. Elsevier, 2015.

[46] B N Alam and D Chaira. Solid State Recycling of Waste Ti Chips: Effect of Wet and Dry Grinding on Synthesis of Ti-Tic Composite Powder during Planetary Milling. page 7.

[47] Methods for Assessing Surface Cleanliness. In Developments in Surface Contamination and Cleaning, Volume 12, pages 23–105. Elsevier, 2019.

[48] Scott A Speakman. Introduction to X-Ray Powder Diffraction Data Analysis. page 25.

[49] Introduction to Solid State Chemistry, Lecture Notes No. 5, X-rays and X-ray Diffraction, 2010.

[50] Diffrac.eva User Manual, 2011.

[51] Ernstsson Marie and Wärnheim Torbjörn. Surface Analytical Techniques Applied to Cleaning Processes. In Handbook for Cleaning/Decontamination of Surfaces, pages 747–789. Elsevier, 2007.

[52] F. A. Lukiyanov, E. I. Rau, and R. A. Sennov. Depth range of primary electrons, electron beam broadening, and spatial resolution in electron-beam studies. Bulletin of the Russian Academy of Sciences: Physics, 73(4):441–449, April 2009.

[53] Xinyu Liu, Roxanne Fernandes, Andrea Jurisicova, Robert F. Casper, and Yu Sun. In situ mechanical characterization of mouse oocytes using a cell holding device. Lab on a Chip, 10(16):2154, 2010.

[54] Hysitron. TI Premier User Manual, 2014.

[55] George M. Pharr, Erik G. Herbert, and Yanfei Gao. The Indentation Size Effect: A Critical Examination of Experimental Observations and Mechanistic Interpretations. Annual Review of Materials Research, 40(1):271–292, June 2010.

[56] R. Boyer, G. Welsch, and E.W. Collings. Materials Properties Handbook: Titanium Alloys. ASM International, Materials Park, OH, 1994.

[57] W Zhou and K G Chew. The rate dependent response of a titanium alloy subjected to quasi-static loading in ambient environment. page 7.

[58] Mendonça Claudiney, Oliveira Adhimar, Sachs Daniela, Capellato Patricia, Ribeiro Vander, Junqueira Mateus, Melo Mirian, and Silva Gilbert. A New Method to Recycle Stainless–Steel Duplex UNS S31803 Chips. Metals, 8(7):546, July 2018.

[59] Wei Cai and William D. Nix. Imperfections In Crystalline Solids. Cambridge University Press, Cambridge, UK, 2016.

[60] Satish Kolli, Vahid Javaheri, Thomas Ohligschläger, Jukka Kömi, and David Porter. The importance of steel chemistry and thermal history on the sensitization behavior in austenitic stainless steels: Experimental and modeling assessment. Materials Today Communications, 24:101088, September 2020.

[61] Abbas Bahrami and Peyman Taheri. A Study on the Failure of AISI 304 Stainless Steel Tubes in a Gas Heater Unit. Metals, 9(9):969, September 2019.

[62] A Pardo, M C Merino, M Carboneras, A E Coy, F Viejo, R Arrabal, and J A Muñoz. Influence of C, N and Ti concentration on the intergranular corrosion resistance of AISI 316 Ti stainless steel. page 8.

[63] Christoph Doerr, Jin-Yeon Kim, Preet Singh, James J. Wall, and Laurence J. Jacobs. Evaluation of sensitization in stainless steel 304 and 304L using nonlinear Rayleigh waves. NDT & E International, 88:17–23, June 2017.

[64] Kamran Saeidi, Lenka Kvetková, František Lofaj, and Zhijian Shen. Austenitic stainless steel strengthened by the in situ formation of oxide nanoinclusions. RSC Advances, 5(27):20747–20750, 2015.

[65] Majid Laleh, Anthony E. Hughes, Sam Yang, Jianli Li, Wei Xu, Ian Gibson, and Mike Y. Tan. Two and three-dimensional characterisation of localised corrosion affected by lack-of-fusion pores in 316L stainless steel produced by selective laser melting. Corrosion Science, 165:108394, April 2020.

[66] Masakatsu Hasegawa. Ellingham Diagram. In Treatise on Process Metallurgy, pages 507–516. Elsevier, 2014.

[67] Manas Vijay Upadhyay, Meriem Ben Haj Slama, Steve Gaudez, Nikhil Mohanan, Lluis Yedra, Simon Hallais, Eva Héripré, and Alexandre Tanguy. Non-oxide precipitates in additively manufactured austenitic stainless steel. Scientific Reports, 11(1):10393, December 2021.

[68] Vinícius Fernandes de Souza, Alef José Araújo, Josué Lucas do Nascimento Santos, Carlos Alberto Della Rovere, and Artur Mariano de Sousa Malafaia. Kinetics Oxidation and Characterization of Cyclically Oxidized Layers at High Temperatures for FeMnSiCrNiCe and FeSiCrNi Alloys. Materials Research, 20(suppl 2):365–373, September 2017.

[69] Alexander D. Preston and Kaka Ma. Insight into the effects of pore size and distribution on mechanical properties of austenite stainless steels. Journal of Materials Science, 56(30):17278–17295, October 2021.

[70] Omid Khalaj, Ehsan Saebnoori, Hana Jirková, Ondřej Chocholatý, Ludmila Kučerová, Jan Hajšman, and Jiří Svoboda. The Effect of Heat Treatment on the Tribological Properties and Room Temperature Corrosion Behavior of Fe–Cr–Al-Based OPH Alloy. Materials, 13(23):5465, November 2020.

[71] D. A. Porter and K. E. Easterling. Phase Transformations in Metals and Alloys. Springer US, Boston, MA, 1992.

[72] Phillip D. Harvey. Engineering Properties of Steels. American Society for Metals, Metals Park, OH, 1982.

[73] Keyou S. Mao, Cheng Sun, Yina Huang, Ching-Heng Shiau, Frank A. Garner, Paula D. Freyer, and Janelle P. Wharry. Grain orientation dependence of nanoindentation and deformation-induced martensitic phase transformation in neutron irradiated AISI 304L stainless steel. Materialia, 5:100208, March 2019.

[74] Lan Li, Cody Lough, Adriane Replogle, Doug Bristow, Robert Landers, and Edward Kinzel. THERMAL MODELING OF 304L STAINLESS STEEL SELECTIVE LASER MELTING. Solid Freeform Fabrication Symposium, page 14, 2017.

[75] Energy Efficiency Best Operating Practice Guide for Foundries, 2015.

[76] Hae-Sung Yoon, Jang-Yeob Lee, Hyung-Soo Kim, Min-Soo Kim, Eun-Seob Kim, Yong-Jun Shin, Won-Shik Chu, and Sung-Hoon Ahn. A comparison of energy consumption in bulk forming, subtractive, and additive processes: Review and case study. International Journal of Precision Engineering and Manufacturing-Green Technology, 1(3):261–279, July 2014.

[77] Vladislav Kruzhanov and Volker Arnhold. Energy consumption in powder metallurgical manufacturing. Powder Metallurgy, 55(1):14–21, February 2012.

[78] Charles Manière, Elisa Torresani, and Eugene Olevsky. Simultaneous Spark Plasma Sintering of Multiple Complex Shapes. Materials, 12(4):557, February 2019.

[79] Karabi Das, Pritha Choudhury, and Siddhartha Das. The Al-O-Ti (Aluminum-oxygen-titanium) system. 23(6):12, 2002.

[80] Magnus Neikter. Microstructure and texture of additive manufactured Ti-6Al-4V. PhD thesis, Luleå University of Technology, Luleå, 2017. ISBN: 9789175839868 OCLC: 1026817713.

[81] Lucia Scotti and Alessandro Mottura. Interstitial diffusion of O, N, and C in α -Ti from first-principles: Analytical model and kinetic Monte Carlo simulations. The Journal of Chemical Physics, 144(8):084701, February 2016.

[82] Sung-Yul Lee, Osamu Taguchi, and Yoshiaki Iijima. Diffusion of Aluminum in β-Titanium. MATERIALS TRANSACTIONS, 51(10):1809–1813, 2010.

[83] Rui Li, Laura Riester, Thomas R. Watkins, Peter J. Blau, and Albert J. Shih. Metallurgical analysis and nanoindentation characterization of Ti–6Al–4V workpiece and chips in high-throughput drilling. Materials Science and Engineering: A, 472(1-2):115–124, January 2008.

[84] Mojtaba Izadi, Aidin Farzaneh, Mazher Mohammed, Ian Gibson, and Bernard Rolfe. A review of laser engineered net shaping (LENS) build and process parameters of metallic parts. Rapid Prototyping Journal, 26(6):1059–1078, April 2020.

[85] M H Moys. A model of mill power as affected by mill speed, load volume, and liner design. Journal of The South African Institute of Mining and Metallurgy, 93(6):135–141, June 1993.

[86] A. Mahboubi Soufiani, M. H. Enayati, and F. Karimzadeh. Fabrication and characterization of nanostructured Ti6Al4V powder from machining scraps. Advanced Powder Technology, 21(3):336–340, May 2010.

[87] C Machio, H.K. Chikwanda, and S. Chikosha. Effect of process control agent (PCA) on the characteristics of mechanically alloyed Ti-Mg powders. Misty Hills, Muldersdrift, October 2010.

[88] Magnus Ahlfors, Johan Hjärne, James Shipley, and Quintus Technologies. Cost effective Hot Isostatic Pressing. A cost calculation study for AM parts. page 7, 2018.

[89] W.H. Lee, Y.J. Jo, Y.H. Kim, Y.H. Jo, J.G. Seong, C.J. Van Tyne, and S.Y. Chang. Self-Consolidation Mechanism Of Porous Ti-6Al-4V Implant Prototypes Produced By Electro-Discharge-Sintering Of Spherical Ti-6Al-4V Powders. Archives of Metallurgy and Materials, 60(2):1185–1189, June 2015.

[90] Yang Xia, Hyrum D. Lefler, Zhigang Zak Fang, Ying Zhang, and Pei Sun. Energy consumption of the Kroll and HAMR processes for titanium production. In Extractive Metallurgy of Titanium, pages 389–410. Elsevier, 2020.

[91] Hyo-haeng Cho, Sangyeob Lim, Hyung-Ha Jin, Junhyun Kwon, Soon-Jik Hong, and Chan-sun Shin. Microstructures and high-temperature tensile properties of mechanically alloyed and spark plasma-sintered 304SS-CNT composites. Journal of Composite Materials, 52(20):2755–2766, August 2018. Publisher: SAGE Publications Ltd STM.

[92] Alexander Preston. Effect of Powder Morphology on Spark Plasma Sintered Stainless Steel Parts, February 2020.

[93] Syed A.M. Tofail, Elias P. Koumoulos, Amit Bandyopadhyay, Susmita Bose, Lisa O'Donoghue, and Costas Charitidis. Additive manufacturing: scientific and technological challenges, market uptake and opportunities. Materials Today, 21(1):22–37, January 2018.

[94] Kuang-Hua Chang. Rapid Prototyping. In e-Design, pages 743–786. Elsevier, 2015.

[95] Sudip Kundu, Manowar Hussain, Vikas Kumar, Shakti Kumar, and Alok Kumar Das. Direct metal laser sintering of TiN reinforced Ti6Al4V alloy based metal matrix composite: Fabrication and characterization. The International Journal of Advanced Manufacturing Technology, 97(5-8):2635–2646, July 2018.